INTERROGATING TISSUE PERFUSION AND OXYGENATION USING DYNAMIC MAGNETIC RESONANCE IMAGING AND QUANTITATIVE SUSCEPTIBILITY MAPPING

A Dissertation

Presented to the Faculty of the Graduate School

of Cornell University

In Partial Fulfillment of the Requirements for the Degree of

Doctor of Philosophy

by

Bo Xu

January 2014

INTERROGATING TISSUE PERFUSION AND OXYGENATION USING DYNAMIC MAGNETIC RESONANCE IMAGING AND QUANTITATIVE SUSCEPTIBILITY MAPPING

Bo Xu, Ph. D.

Cornell University 2014

Magnetic resonance imaging (MRI) is a widely used non-invasive imaging technique, with rich contrast for interrogation of tissue physiology and pathology. MRI can be used to examine hemodynamic conditions like perfusion and oxygenation qualitatively and quantitatively. This dissertation reports new techniques that employ dynamic imaging and quantitative susceptibility mapping (QSM) to overcome technical challenges for improved MRI perfusion imaging and oxygenation quantification.

Perfusion imaging after gadolinium contrast agent administration is a common clinical practice, where dynamic MRI technique is used to track contrast bolus. It is desirable to have high temporal resolution to capture blood dynamics, as well as high spatial resolution to depict small lesions. Unfortunately, these requirements are limited by hardware and physiological conditions. In this dissertation, a dynamic MRI technique was realized, using fast spiral acquisition and a constrained image reconstruction algorithm, to achieve high temporal-spatial resolution for liver perfusion imaging.

Tissue susceptibility provides unique contrast in MRI. Recent development of QSM technique has been applied in various clinical applications. In this dissertation,

the dynamic imaging method was extended to multi-echo acquisition and combined with QSM to map gadolinium contrast agent concentration during the first passage for cerebral perfusion mapping.

Blood oxygenation is determined by the amount of deoxyhemoglobin in red blood cell. Magnetic susceptibility of deoxyhemoglobin is a source of MR contrast for imaging oxygenation. This dissertation reports correction schemes in both data acquisition and image reconstruction of QSM for improved blood oxygenation quantification.

BIOGRAPHICAL SKETCH

Bo Xu was born in Harbin, Heilongjiang, China in 1985. He received the Bachelor of Science degree in Electrical Engineering from Tsinghua University in 2008. In the same year, he joined the graduate program of Biomedical Engineering at Cornell University and received the Masters of Science degree in Biomedical Engineering in 2011.

Dedicated To My Parents

For Their Love And Encouragement

ACKNOWLEDGMENTS

I would like to thank my advisor, Yi Wang, for his vision in research direction, guidance on scientific thinking. He helped me to improve in all aspects, from conducting original research to forming efficient working habits, from presentation skills to professional attitude. He taught me to think rigorously and systematically, to accomplish things efficiently and fearlessly. His passion for constant improvement and higher achievements has greatly inspired me.

I am especially grateful for Pascal Spincemaille for his help and advice. I have been closely working with him since I started in the lab. I learned most of my pulse sequence programming and scientific writing skills from him. His problem solving skill and scientific reasoning greatly influenced me and inspired me to improve. His insights in MR physics and mathematics helped me to overcome obstacles. He is warm hearted and willing to help in every aspect of my research.

I would like to thank Dr. Martin Prince for his help in clinical aspects of my projects. His insights of diseases and their interpretation for imaging made me clear of what to do and what to explore. Our collaboration in liver projects encouraged me to translate my research to clinical scans. I am especially grateful for his help of contrast enhancement studies.

I owe my special thanks to Tian Liu for his help in all aspects of my research. I was always inspired through valuable discussions with him. He is a landmark in my lab that drives me to grow as a graduate student. I am grateful to Thanh Nguyen for his help in pulse sequence programming and MR physics. He was always patient and

nice to answer my questions in great details.

My gratitude goes to Drs Silvina Dutruel, Nanda Thimmappa, Mukta Agrawal and Bea Reig for their help of contrast agent administration in volunteer studies. They sacrificed their private time and were very supportive throughout the contrast scans, without which I could not have accomplished the perfusion projects.

I would to thank my colleagues Bryan Kressler, Noel Codella, Jing Liu, Gang Chen, Weiwei Chen, Keigo Kawaji, Shuai Wang, Fei Sun, Alexey Dimov, Mitch Cooper, Cynthia Wisnieff and Dong Zhou, who have provided valuable discussions and experimental help.

I am especially grateful to my parents and my wife for their constant support and encouragement through my graduate study. They made me stronger to overcome obstacles on my way ahead.

Finally I would like to acknowledge my Special Committee, Yi Wang, Peter Doerschuk and David Christini, who agreed as official examiners of this dissertation.

TABLE OF CONTENTS

LIST OF FIGURES

LIST OF TABLES

LIST OF ABBREVIATIONS

MRI	Magnetic Resonance Imaging
TR	Repetition Time
TE	Echo Time
SNR	Signal Noise Ratio
CNR	Contrast Noise Ratio
FOV	Field Of View
ROI	Region Of Interest
3D	Three-dimensional
4D	Four-dimensional
SENSE	SENSitivity Encoding
TRACER	Temporal Resolution Acceleration with Constrained Evolution Reconstruction
QSM	Quantitative Susceptibility Mapping
DCE	Dynamic Contrast Enhanced
LM	Levenberg Marquardt
IRGNM	Iteratively Regularized Gauss-Newton Method
DSC	Dynamic Susceptibility Contrast
AIF	Arterial Input Function
CBF	Cerebral Blood Flow
CBF	Cerebral Blood Volume
ASL	Arterial Spin Labeling
SvO_2	Venous Oxygen Saturation

CHAPTER 1

INTRODUCTION

MRI is a versatile imaging modality used in a wide range of clinical realms. Since its early invention, MRI has been used to imaging vessel physiology and blood flow. Perfusion MRI is a technique to investigate blood delivery to capillary beds in biological tissues. It involves three categories of imaging method: dynamic contrast enhanced (DCE) MRI, dynamic susceptibility contrast (DSC) MRI and arterial spin labeling (ASL). DCE-MRI and DSC-MRI use extraneous contrast agent and benefit from increased SNR from elevated blood contrast. In the first passage of contrast agent, vessels and tissues have a peak enhancement with the contrast arrival. This peak enhancement may vary across different tissues by its arrival time, amplitude, widths and shape. The enhancement pattern provides a qualitative and quantitative understanding of the tissue perfusion that can help diagnosis of diseases such as stroke and tumor.

The first passage of contrast agent only spans tens of second if not shorter. This short time window poses great challenges to capturing the enhancement dynamics accurately. Temporal resolution, spatial resolution and volume coverage bring conflicting scan requirements for dynamic MRI. In addition, hardware limits, physiological constraints, respiratory and cardiac motions pose difficulties for high spatial-temporal resolution imaging of contrast agent first passage. To overcome these difficulties, signal acquisition and image reconstruction innovations have been sought for to accelerate dynamic MRI. Techniques are developed to exploit the redundancy in

spatial and temporal information, among which, non-Cartesian sampling, parallel imaging, compressed sensing and constrained reconstruction are shown to be successful. Each acceleration scheme is tuned to fit certain applications and can be combined with other schemes to achieve further acceleration.

Blood oxygenation is an important physiological parameter. The susceptibility effect of deoxyhemoglobin in the blood can be used to quantify venous oxygenation. When a vessel is approximated as a long cylinder, the blood susceptibility is proportional to its induced phase shift, with knowledge of the angle between the vessel and magnetic field. This limits the available vessels for measurement and prevent from mapping global oxygenation. Mapping susceptibility without geometric constraints is desired. Recently developed quantitative susceptibility mapping serves to this need. QSM has been successful in static tissues but needs further investigation for mapping blood susceptibility. Flow induced extra phase needs to be considered in both acquisition and reconstruction for accurate blood susceptibility mapping.

1.1 Summary of Contributions

In this dissertation, three techniques for interrogating tissue perfusion and quantitating oxygenation are developed. First, a fast dynamic imaging framework is developed to allow high temporal frame rate dynamic contrast enhanced liver imaging. Second, this dynamic imaging technique is extended for multi-echo acquisition and combined with quantitative susceptibility mapping for contrast agent quantification in cerebral perfusion imaging. Thirdly, a correction scheme is developed to account for blood flow induced phase error in quantitative susceptibility mapping, permitting more

accurate venous oxygenation quantification.

1. *Dynamic Contrast Enhanced Liver Imaging*. Chapter 3 presents a fast dynamic imaging technique that achieves sub-second temporal frame rate for dynamic contrast enhanced liver imaging. Spiral trajectory with golden angle view order and fat suppression was designed for data acquisition. Temporal Resolution Acceleration with Constrained Evolution Reconstruction (TRACER) was developed for reconstruction. TRACER utilizes the prior information from previous frame and updates the dynamic change using information from single spiral sampling. Its temporal tracking ability is tested in phantom studies. The high temporal update gives exquisite depiction of vessel and tissue enhancement patterns, which allows confident qualitative assessment of liver perfusion.
2. *Dynamic Susceptibility Mapping.* Chapter 4 proposes a new technique to measure gadolinium contrast agent concentration for cerebral perfusion imaging. A multi-echo spiral readout sequence is developed. All-echo flow compensation gradients are designed. Time resolved phase data are reconstructed to compute dynamic susceptibility maps. Artery and tissue concentration time curves are obtained directly from the susceptibility maps. These time curves are used to generate cerebral blood flow and cerebral blood volume maps. Contrast concentration measurement from susceptibility avoids the assumption of linear relaxivity-concentration and requirement for tissue relaxivity in T2* based method. The measured cerebral blood flow matches that obtained from arterial spin labeling technique.
3. *Venous Oxygenation Quantification.* Chapter 5 reports an improved quantitative

susceptibility mapping technique to measure blood susceptibility for oxygenation quantification. The relationship between MR phase signal and echo time is modeled in the presence of flow. Gradient moment nulling was applied on each gradient axes for all echoes. An adaptive-quadratic fit that better models the blood voxel phase TE relationship was proposed. Phantom experiments demonstrate improved susceptibility mapping with adaptive-quadratic fit. In vivo studies show better visualization of the veins and improved oxygenation values.

CHAPTER 2

BACKGROUND

MRI stems from nuclear magnetic resonance (NMR). Interaction of nuclear spins with an external magnetic field results in spin precession about the field direction, which induces signals that could be detected for imaging. The dominant nucleus in MRI is hydrogen proton which accounts for two thirds of the body weight. By manipulating the magnetic field, detecting the bulk precession and reconstructing the signal, organs and tissues could be imaged. In this chapter, the MRI physics is briefly introduced, several image reconstruction methods are presented, and biological aspects related to this dissertation are discussed.

2.1 MRI Physics

2.1.1 Signal generation

When a proton spin is placed in an external magnetic field $\boldsymbol{B}_0$, its magnetic moment $\boldsymbol{\mu}$ rotates along the field direction. This spin precession phenomenon can be described by Eq [2.1].

$$\frac{d\boldsymbol{\mu}}{dt} = \gamma\boldsymbol{\mu} \times \boldsymbol{B}_0 \qquad [2.1]$$

The γ factor, called gyromagnetic ratio depends on the nucleus and $\gamma = 2.675 \times 10^8 \frac{rad}{s}/T$, or $\gamma = 42.58\text{MHz}/T$ for proton. To generate detectable MR signal, a radio-frequency (rf) field $\boldsymbol{B}_1$ is applied to tip the proton spin away from $\boldsymbol{B}_0$

direction. The frequency of $\boldsymbol{B}_1$ has to match the gyromagnetic frequency for effective polarization (on resonance). The $\boldsymbol{B}_1$ field is only applied for a finite time, tipping the spin away from B_0 direction for certain degree, called flip angle. This process is termed as "rf excitation". The rf pulses are usually designed to excite a certain slab of tissue and the detected signal is from this section of the imaging object.

The bulk magnetization $\boldsymbol{M}$ is used to describe an ensemble of spins. After rf excitation, spin isochromats try to align with the B_0 field due to the energy exchange of spins and their surroundings. The longitudinal magnetization $\boldsymbol{M}_z$ recovers to $\boldsymbol{M}_0$, which is called spins-lattice relaxation. The inverse of the rate of change, called spin-lattice relaxation time T_1, varies among different tissues. The spin-spin interaction causes decay of transverse magnetization $\boldsymbol{M}_{xy}$. The spin-spin relaxation time T_2 also varies in different tissues. Putting polarization and relaxation together, the bulk magnetization after rf excitation can be described using Bloch equation:

$$\frac{d\boldsymbol{M}}{dt} = \gamma \boldsymbol{M} \times \boldsymbol{B}_0 + \frac{1}{T_1}(\boldsymbol{M}_0 - \boldsymbol{M}_z) - \frac{1}{T_2}\boldsymbol{M}_{xy} \qquad [2.2]$$

The transverse magnetization $\boldsymbol{M}_{xy}$ has a frequency corresponding to the gyromagnetic ratio. This radio-frequency transverse magnetization generates signal to be detected in MRI.

2.1.2 Spatial encoding

A linear gradient field $\boldsymbol{G}(t)$ is used to encode spins at different positions. In each location, the spins see a local magnetic field that slightly deviates from B_0, thus having different precession rates. The tissue at a particular position is differentiated by

the frequency of the signal it generates. Three sets of coils are used to create $\boldsymbol{G}(t)$. The maximum gradient amplitude ant slew rates determines the scan time and are important factors to evaluate the scanner performance. With the help of spatial encoding, MR signal equation is formulated in Eq [2.3],

$$s(\boldsymbol{k}) = \int \rho(\boldsymbol{x}) e^{-i\gamma \boldsymbol{k}\boldsymbol{x}} d\rho \qquad [2.3]$$

Here ρ is proton density including the relaxation effect, $\boldsymbol{x}$ is spatial coordinates, $\boldsymbol{k}(t) = \gamma \int_0^t \boldsymbol{G}(\tau)\, d\tau$ is the so called k-space coordinates. Notice the acquired signal $s(\boldsymbol{k})$ is the spatial Fourier transform of the imaging object $\rho(\boldsymbol{x})$. The spatial frequency domain or k-space is traversed by adjusting gradient field $\boldsymbol{G}(t)$. Different sampling strategies to traverse the k-space can be designed by using different $\boldsymbol{G}(t)$.

2.1.3 Signal detection and acquisition

The transverse magnetization is detected using receiver rf coils. Time varying $\boldsymbol{M}_{xy}$ generates magnetic flux and current in receiver coils. The electric signal is amplified, digitized, demodulated and filtered. Usually an array of receiver coils is used to reach uniform coverage of the object. Each array element *m* has a distinct complex sensitivity c_m. The sensitivity is determined by the position and phase of the coil element. For a coil array with N_c elements, the signal equation for each coil is

$$s_m(\boldsymbol{k}) = \int \rho(\boldsymbol{x}) c_m(\boldsymbol{x}) e^{-i\gamma \boldsymbol{k}\boldsymbol{x}} d\rho \quad (m = 1 \sim N_c) \qquad [2.4]$$

The coil images $s_m(\boldsymbol{k})$ are combined to form the final image.

The transverse magnetization $\boldsymbol{M}_{xy}$ experiences T_2 decay effect during data acquisition. The imperfect magnetic field creates additional phase dispersion and decay. The combined decay rate is quantified as T_2^*. There are two types of signal acquisition method: spin echo and gradient echo. Spin echo acquisition employs two rf pulses: a π/2-pulse followed by a π-pulse. The π-pulse reversed any field inhomogeneity induced dephasing and forms T_2 decay signal envelop. Gradient echo acquisition only has an α-pulse and forms T_2^* decay signal envelop.

In gradient echo sequence, after each α-pulse, the longitudinal magnetization recovers to some degree before next pulse. After a few continuously applied rf pulse, the transverse magnetization reaches steady state:

$$m_{xy} = m_0 sin\alpha \frac{1 - e^{-TR/T1}}{1 - e^{-TR/T1} cos\alpha} \quad [2.5]$$

At the end of each rf pulse, if the transverse magnetization is completely dephased or spoiled by applying a big gradient, the sequence is called spoiled gradient echo (SPGR) sequence. In this dissertation, SPGR is the primary type of sequence to use.

To satisfy the Nyquist theorem, the k-space sampling interval has to be dense enough to completely recover the object. The minimal sampling interval Δk = 1/FOV, where FOV is the imaging field of view. Violation of the sampling theorem can result in aliasing artifact.

2.1.4 Sampling trajectory

By manipulating the gradient field, different sampling strategies can be achieved for k-space sampling. The most common way is Cartesian sampling, where the k-space is

sampled line by line. One k-space line is acquired before stepping the phase encoding gradient in the following TR. A typical pulse sequence and sampling trajectory for Cartesian sampling is shown in Figure 2.1.

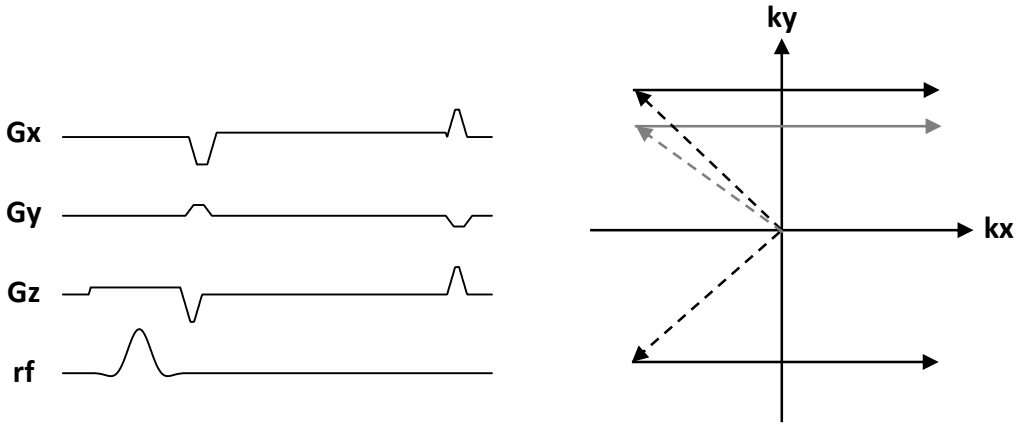

Figure 2.1 Cartesian Sampling
Pulse sequence diagram and k-space sampling scheme in Cartesian sampling.

Non-Cartesian trajectories like radial or spiral has higher k-space sampling efficiency. In radial sampling, the k-space is traversed by a set of radial spokes. Each spoke is a k-space line as in Cartesian sampling but they all cross the center of k-space so carrying the low frequency information. Figure 2.2 shows the pulse sequence diagram and k-space trajectory in radial sampling. In spiral sampling, each spiral leaf spreads from the k-space center and covers a big portion of the k-space. By adjusting the shape of the spiral, different density of k-space coverage could be achieved. Figure 2.3 shows the pulse sequence diagram and k-space trajectory of a spiral sampling. Both radial and spiral sampling are robust to motion and as they sample the center of k-space frequently. They also give flexibility for view ordering when used in dynamic imaging techniques.

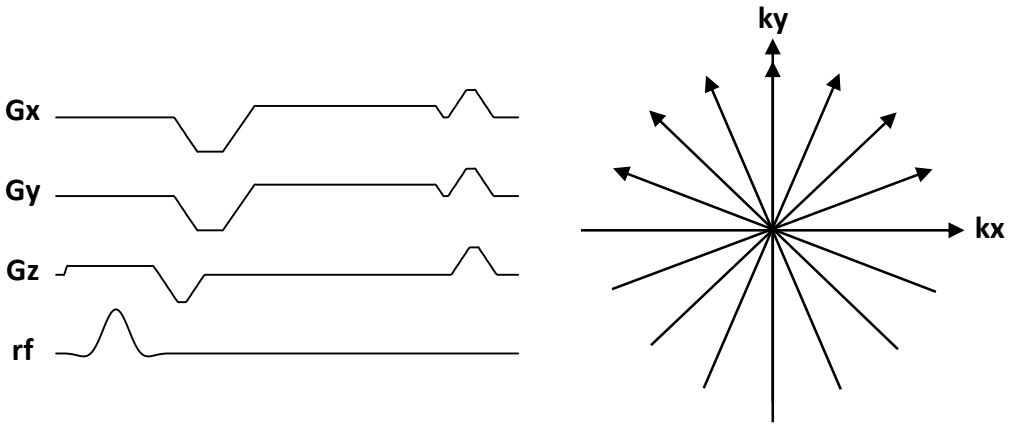

Figure 2.2 Radial Sampling
Pulse sequence diagram and k-space trajectory in radial sampling.

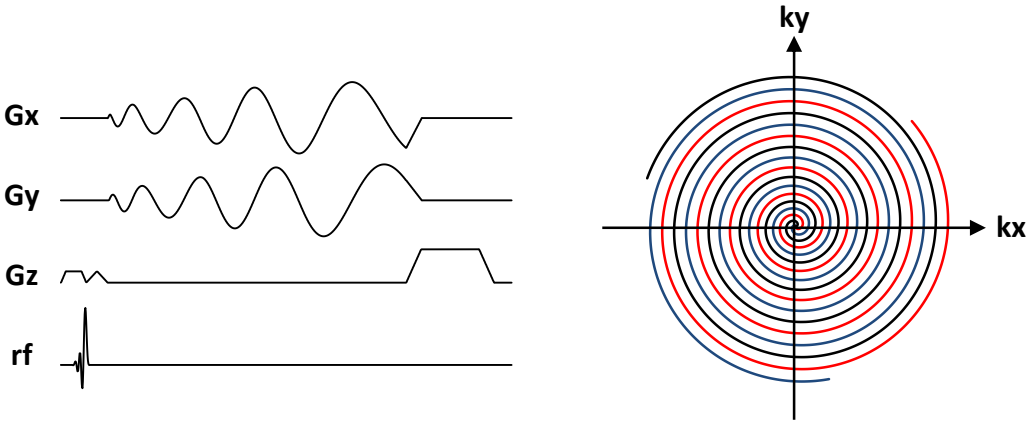

Figure 2.3 Spiral sampling
Pulse sequence diagram and k-space trajectory in spiral sampling.

Non-Cartesian sampling is sensitive to gradient imperfections and magnetic field inhomogeneity. Care must be taken when designing and implementing non-Cartesian pulse sequence. Post-processing correction maybe needed to obtain artifact free images.

2.2 Image Reconstruction

For Cartesian sampling that satisfies Nyquist theorem, image reconstruction could be as simple as a discrete Fourier transform. With more complicated acquisition strategies and parallel imaging, dedicated image reconstruction beyond simple Fourier transform is needed. This section gives an overview of non-Cartesian Fourier transform, parallel imaging and dipole inversion for susceptibility mapping. Lastly, iterative reconstruction is discussed.

2.2.1 Non-uniform Fourier transform

In non-Cartesian sampling, acquired k-space data is not uniformly distributed on rectangular grid. The data is gridded to rectangular points for Fourier transform. A flow chart of the gridding steps is shown in Figure 2.4.

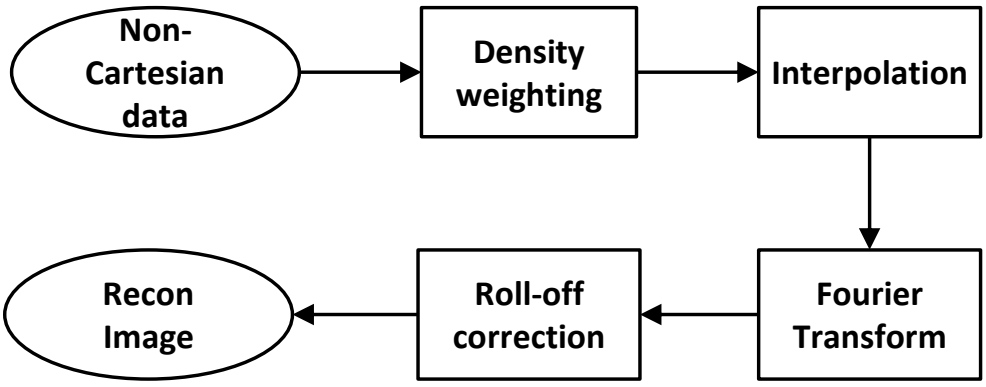

Figure 2.4 Gridding steps
The non-Cartesian data is first weighed by their density and then interpolated onto grids. The rectangular k-space data is Fourier transformed. Then roll-off correction is performed to get the final image.

Firstly, the non-Cartesian data is weighed by a density function. The density weighting is inverse correlated with the density of the sampled data. For example, in radial sampling, the density is proportional to the radius of the k-space sampled point.

In the next step, non-Cartesian points are interpolated onto rectangular grids by convolving with a Kaiser-Bessel kernel. An appropriate kernel size is chosen and usually the gridding size corresponds to two times the FOV. The Cartesian grid k-space data is Fourier transform to obtain an image. This image is cropped to the original size to get rid of residual artifacts outside the FOV. Finally a roll-off correction is applied, where the intermediate image is divided by Fourier transform of the convolving kernel to get the final reconstructed image.

2.2.2 Parallel imaging

As previously mentioned, most receiver coils are arrays of coil elements. Each element covers a distinct part of the body and exhibits its own coil sensitivity. Traditionally, all coil images are combined together to get the final image. Due to the need for fast imaging application, parallel imaging has been developed where the correlation among different coils are used to accelerate the data acquisition for fast imaging. There are two categories of parallel imaging technique: k-space based method and image space based method.

In k-space based method, coil sensitivities are not known but implicitly used as k-space convolution kernels. A typical method in this category is GeneRalized Autocalibrating Partially Parallel Acquisitions (GRAPPA). Multiplication of image and coil sensitivity is equivalent to convolution of their corresponding k-space representation. As the coil sensitivity is usually very smooth, its k-space representation, or k-space convolution kernel is narrow and focal. Each k-space point can be reformatted as a weighted average of its surrounding points and the points from other coils. The weightings could be calibrated from a fully sampled k-space region

and used to reconstruct k-space region that is not acquired.

In image space based method, known coil sensitivities are directly used to exploit data redundancy. A typical method in this category is SENSitivity Encoding (SENSE). Figure 2.5 shows the concept of SENSE in a two-coil example.

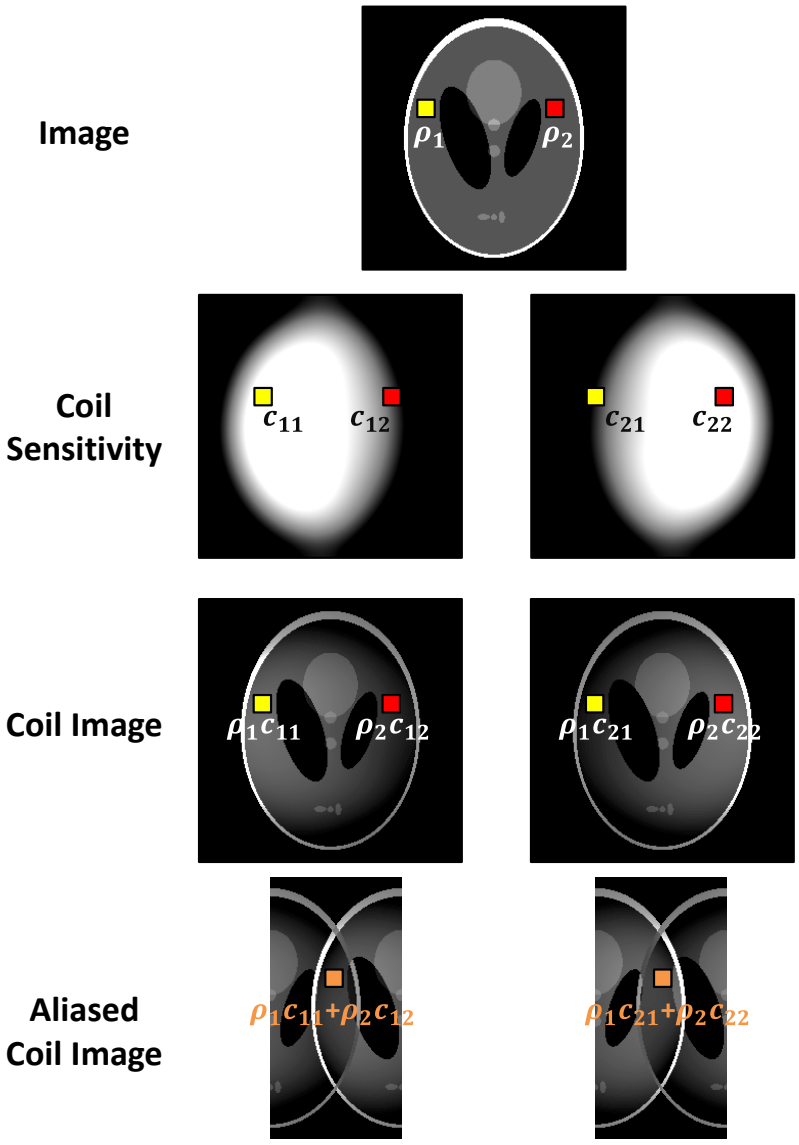

Figure 2.5 principle of sensitivity encoding
The aliased coil image is a weighed sum of voxels from the original image. The weighting is the coil sensitivity.

Two voxels marked by yellow and red have signal intensity of ρ_1 and ρ_2. The coil

sensitivity of the corresponding voxel in the two coils are c_{11}, c_{12} and c_{21}, c_{22} respectively. The fully sampled coil image is the original image weighted by the coil sensitivity. In accelerated imaging, only half of the k-space lines are acquired. The corresponding coil image is aliased. One voxel in this aliased image is the sum of two voxels in the "true" coil images. With known coil sensitivities, there are two unknowns ρ_1 and ρ_2 and two measurements y_1 and y_2. Solving a linear equation would recover ρ_1 and ρ_2.

$$\begin{cases} y_1 = c_{11}\,\rho_1 + c_{12}\,\rho_2 \\ y_2 = c_{21}\,\rho_1 + c_{22}\,\rho_2 \end{cases} \quad [2.6]$$

A more general form of this linear system is:

$$\begin{bmatrix} y_1 \\ \vdots \\ y_{N_c} \end{bmatrix} = \begin{bmatrix} c_{11} & \cdots & c_{1R} \\ \vdots & & \vdots \\ c_{N_c 1} & \cdots & c_{N_c R} \end{bmatrix} \begin{bmatrix} \rho_1 \\ \vdots \\ \rho_{N_c} \end{bmatrix} \quad [2.7]$$

When the system is over-determined ($N_c > R$), and the coils sensitivities are distinct (coil sensitivity matrix is well conditioned), an accurate estimation of the voxel image content could be obtained. In this dissertation, the proposed constrained reconstruction method is image based parallel imaging that rooted from SENSE.

2.2.3 Susceptibility mapping

Magnetic susceptibility indicates the degree of magnetization of a material in response to an applied magnetic field. Many biological relevant materials like iron, calcium and gadolinium have different susceptibility. It provides an addition contrast to T_1 and T_2. Quantifying susceptibility opens a new venue to investigate tissue physiology and

pathology.

The longitudinal magnetic field produced by a material with susceptibility χ can be determined by convolving the susceptibility distribution with the dipole response

$$\Delta B_z(\boldsymbol{r}) = \frac{1}{4\pi}\int \chi(\boldsymbol{r}')\frac{3cos^2\theta - 1}{|\boldsymbol{r}-\boldsymbol{r}'|^3}d^3\boldsymbol{r}' \quad [2.8]$$

where $\Delta B_z(\boldsymbol{r})$ is the field change, $\boldsymbol{r}$ is the spatial coordinate, θ is the angle between $\boldsymbol{r}-\boldsymbol{r}'$ and $\boldsymbol{B}_0$. By measuring $\Delta B_z(\boldsymbol{r})$, the susceptibility distribution χ can be computed by de-convolution of the dipole kernel. The $\Delta B_z(\boldsymbol{r})$ field generated from susceptibility source does not change with time. Considering this local field change, the MR signal equation becomes:

$$s(\boldsymbol{k}) = \int \rho(\boldsymbol{x})e^{-i\gamma\Delta B(\boldsymbol{r})TE}e^{-i\gamma\boldsymbol{k}\boldsymbol{x}}d\rho \quad [2.9]$$

The field change results in a phase shift in the image that is proportional to TE. By measuring the phase and performing a linear fit, $\Delta B(\boldsymbol{r})$ could be obtained.

The obtained $\Delta B(\boldsymbol{r})$ is the total field change that induced by tissue as well as air, bone and fat which has much higher susceptibility. These susceptibility sources create a big background magnetic field that needs to be removed to unveil the local field that produced by tissue of interest.

After the background removal step, a dipole de-convolution algorithm is applied to de-convolve χ from Eq [2.9]. The dipole kernel $\frac{3cos^2\theta-1}{|\boldsymbol{r}-\boldsymbol{r}'|^3}$ has a zero value cone surface which makes the de-convolution under-determined problem. Prior knowledge needs to be incorporated to perform this de-convolution. Robust, efficient and accurate

de-convolution algorithm is still a hot topic under research.

2.2.4 Iterative reconstruction

In accelerated MRI, non-Cartesian sampling and parallel imaging are often combined to achieve high acceleration factor. In 2.3.2, the reconstruction procedure of SENSE is introduced. In that example, the Cartesian under-sampling in k-space results in a nice aliasing pattern that could be used to form a linear system to reconstruct the original image. For non-Cartesian sampling, the aliasing in image space does not have an explicit representation from the image and coil sensitivities. Direct un-aliasing is not readily available.

Iterative reconstruction can be used in this scenario. The MR signal equation

$$s_m(\boldsymbol{k}) = \int \rho(\boldsymbol{x}) c_m(\boldsymbol{x}) e^{-i\gamma \boldsymbol{k}\boldsymbol{x}} d\rho \quad (m = 1 \sim N_c) \qquad [2.10]$$

can be reformulated in a linear system point. Let $\cdot$ denotes point-wise matrix multiplication, and $\mathcal{F}$ denotes Fourier transform operator, the signal equation becomes

$$s_m = \mathcal{F}(c_m \cdot \rho) \quad (m = 1 \sim N_c) \qquad [2.11]$$

or

$$\boldsymbol{s} = \mathcal{F}(\boldsymbol{c} \cdot \rho) \qquad [2.12]$$

where $\boldsymbol{s} = [s_1, \cdots, s_{N_c}]$, and $\boldsymbol{c} = [c_1, \cdots, c_{N_c}]$. The non-Cartesian sampling could also be treated as a linear operator *P*, which is a projection function in k-space. Then

the signal equation becomes:

$$\boldsymbol{s} = P\mathcal{F}(\boldsymbol{c} \cdot \rho) = E(\rho) \quad [2.13]$$

When P is equally spaced Cartesian projection, E could be directly inversed. When P is a non-Cartesian projection, multiply both side of the equation with E^H to make the system symmetric positive-definite.

$$\boldsymbol{c}^H \cdot \mathcal{F}^{-1} P^H \boldsymbol{s} = \boldsymbol{c}^H \cdot \mathcal{F}^{-1} P \mathcal{F}(\boldsymbol{c} \cdot \rho) \quad [2.14]$$

Image ρ could be solved iteratively using conjugate gradient algorithm.

In many MR reconstruction problems, the mathematic formulation is a linear or a nonlinear system based on the physical modeling of a forward problem. In the SENSE reconstruction, the forward problem is MR signal equation. In susceptibility mapping, the forward problem is convolution of dipole kernel with the susceptibility distribution. The commonality of these problems is the high dimension of unknowns and series of operations involved in the model. Iterative reconstruction is used in these situations. It is worth noting that the initial guess and the stopping criteria are important for iterative reconstruction. When the system is under-determined, regularization is needed.

2.3 Contrast Agent

Contrast agents are widely used in MRI to increase the SNR of blood and as a biomarker for quantitative evaluation of hemodynamics. For the past twenty years, gadolinium chelate contrast agent has been widely used in MR angiography, dynamic

contrast enhanced MRI and perfusion MRI. This section discusses about the physics property of gadolinium contrast agent and its usage in different imaging applications.

2.3.1 Contrast enhancement

Gadolinium (Gd) contrast agent is a Gd^{3+} compounds with seven unpaired electrons. The Gd^{3+} based molecules can bind free water and increase the effective relaxation rate of the surrounding water. Presence of contrast agent in the blood can greatly reduce both the longitudinal relaxation time T_1 and transverse relaxation time T_2 of blood. This effect is determined by the relaxivity r_1 and r_2 of the contrast agent. The relationship between relaxation time, relaxivity and contrast agent concentration is given by:

$$\frac{1}{T_1} = \frac{1}{T_{10}} + r_1 C \qquad [2.15]$$

$$\frac{1}{T_2} = \frac{1}{T_{20}} + r_2 C \qquad [2.16]$$

Here T_{10} and T_{20} are relaxation time without contrast agent and *C* is the contrast agent concentration. The T_1 shorting effect is usually applied in T_1 weighted contrast enhanced MRI where the blood signal will be boosted dramatically to give good contrast to noise (CNR) of the blood. The T_2 shorting effect is used in dynamic perfusion MRI for quantitative measurement of the contrast agent concentration.

Besides relaxation effect, gadolinium contrast agent has a high susceptibility. The susceptibility of gadolinium is proportional to its concentration. Quantifying the susceptibility can provide contrast agent bio-distribution, which is an important

indicator of tissue physiology and hemodynamics.

2.3.2 Timing and quantification

Contrast agent is usually intravenous injected into a vein. It is mixed with blood in the heart and pumped to arterial supplied tissue. The contrast arrival time, enhancement peak amplitude and duration depend on the local hemodynamic property. Thus the enhancement pattern carries important pathophysiological information.

The timing of contrast agent is crucial in applications where arterial and portal venous enhancement needs to be differentiated. In the first passage, there is a time window called arterial phase, when only the arteries are enhanced. A couple of seconds after arterial phase is the venous phase when veins get enhanced. In imaging of arterial malfunction, venous enhancement will overwhelm or cover the arteries and affect the diagnosis. Obtaining arterial phase is especially import in liver imaging. Liver has dual blood supply, the hepatic artery and portal vein. Normal liver parenchyma receives 75% blood supply from portal vein, while liver tumor receives most of its blood supply from hepatic artery. To obtain the arterial phase when only hepatic artery enhances is crucial in identification of liver tumors. Furthermore, different liver tumor has different enhancement patterns. Liver enhancement curves provide important information on categorizing different tumors.

Quantification of contrast agent is also essential for many applications including perfusion MRI. Quantitative or semi-quantitative quantification of contrast agent could be determined from the change of blood T_1 and T_2 values pre- and post- contrast administration. Quantification requires contrast agent time curves that acquired from either T_1 or T_2 weighed sequences. T_1 weighed dynamic contrast enhanced MRI is

used to investigate tumor activity. k^{trans}, the volume transfer coefficient between the blood pool and the extracellular extravascular space, is usually computed as an indication of tumor micro-vascular permeability. In cerebral perfusion imaging, the contrast agent time courses in the supplying artery and capillaries can be used to determine cerebral blood volume and cerebral blood flow when the blood brain barrier is intact.

Extracting quantitative time resolved information of contrast agent first pass has great clinical importance and drives the development of fast MRI technique described in this dissertation.

CHAPTER 3

DYNAMIC CONTRAST ENHANCED LIVER MRI

Time-resolved imaging is crucial for the accurate diagnosis of liver lesions. Current contrast enhanced liver MRI acquires a few phases in sequential breath-holds. The image quality is susceptible to bolus timing errors, which could result in missing the critical arterial phase. This impairs the detection of malignant tumors that are supplied primarily by the hepatic artery. Additionally, the temporal resolution may be too low to reliably separate the arterial phase from the portal venous phase. In this study, a method called Temporal Resolution Acceleration with Constrained Evolution Reconstruction (TRACER) was developed with 3D volume coverage and high temporal frame rate. Data is acquired using a stack of spirals sampling trajectory combined with a golden ratio view order using an 8-channel coil array. Temporal frames are reconstructed from vastly under-sampled data sets using a nonlinear inverse algorithm. Numerical and phantom experimental validation is presented. Preliminary in vivo results demonstrate high spatial resolution dynamic 3D images of the whole liver with high frame rates, from which numerous sub-arterial phases could be easily identified retrospectively.

3.1 Introduction

Multi-phase contrast enhanced magnetic resonance imaging is important for assessing liver function and characterizing liver lesions (1-7). The temporal pattern of enhancement may enable the specific characterization of lesions thereby avoiding

biopsy. It is necessary to distinguish the arterial supply from the portal venous supply to lesions and to visualize the perfusion and interstitial distribution of the gadolinium contrast agent in the liver parenchyma. In current liver MRI protocols, typically five phases are acquired: pre-contrast, arterial phase, portal venous phase and two delayed phases. High 3D spatial resolution is needed for the detection of smaller lesions, for which curative therapies can be most effective. Acquisition timing needed to capture the contrast bolus may be actuated using fluoroscopic triggering (8), using a delay derived from a prior test bolus or using a fixed timing delay. This introduces an operator dependence that makes it difficult to guarantee capturing the optimal arterial phase in every patient. An incorrect time delay between the injection and the start of imaging may lead to the loss of the arterial phase and may create a mixture of pre-contrast, arterial and/or portal venous phases. Since liver diseases can affect the vasculature heterogeneously, the optimal timing may also vary with patients and lesions. This indicates that dynamic 3D CE MRI exam should further resolve the arterial phase into multiple sub-phases for accurate diagnosis of liver lesions (9). Even with parallel imaging, a typical 3D acquisition with adequate spatial resolution is over 10 s, which is not adequate for resolving arterial sub-phases.

In this study, a method called Temporal Resolution Acceleration with Constrained Evolution Reconstruction (TRACER) is developed based on a real time 2D radial technique recently proposed by Uecker et al.(10). TRACER samples k-space with a 3D stack of variable density spirals to achieve a high temporal frame rate with whole volume coverage. We aim to validate the temporal tracking accuracy of TRACER and assess its advantages when applied to contrast enhanced liver MRI over the traditional

multi-phase imaging technique.

3.2 Algorithm

The concept of TRACER is to enforce image fidelity to the sampled data of the current time frame therefore minimizing temporal footprint, while maintaining image quality by imposing consistency with the previous image frame. Specifically, we illustrate here how TRACER reconstructs one temporal frame each time one spiral leaf is sampled across all slice encodes in stacked spiral 3D acquisition. Initially, a high quality base frame is formed from a fully sampled dataset, preferably using data without contrast enhancement, after which subsequent 3D volumes are reconstructed from highly under-sampled stack of spiral trajectories by limiting the amount of change that can occur in the images from one temporal frame to the next. Furthermore, the coil sensitivities are assumed to be changing during the scan and are thus considered as unknowns. This data reconstruction process is based on the nonlinear inverse algorithm proposed by Uecker et al. (11,12) where both image content and coil sensitivities can be jointly estimated. The 3D spoiled gradient echo signal equation is written as:

$$y_n = P_n \mathcal{F} P_{FOV}(\rho_n \cdot c_n) = E_n(x_n) \qquad [3.1]$$

where both the image ρ_n and the coil sensitivities c_n are unknown. All symbols are defined in Table 3.1.

A solution x_n at time frame n can be obtained iteratively. This involves linearizing the signal encoding function E_n around the current guess $x_{n,m}$:

$$dE_n/dx(x_{n,m})dx_{n,m} = y_n - E_n(x_{n,m}) \quad [3.2]$$

where $x_{n,m}$ is the solution of the $(m-1)^{th}$ iteration and $dx_{n,m}$ is the update calculated in the m^{th} iteration.

Table 3.1 Symbols used in TRACER

n	time index
m	current iteration number
y_n	k-space measurement at time n
ρ_n	unknown image content at time n
E_n	signal encoding function at time n, which maps the image ρ_n and the coil maps $c_{n,j}$ to the corresponding k-space y_n
N_c	number of coils
$c_{n,j}$	unknown coil sensitivity maps at time n, with $j = 0, ..., N_c - 1$
x_n	vector $(\rho_n, c_{n,0}, c_{n,1}, \ldots, c_{n,Nc-1})$
P_n	k-space projection onto the sampling trajectory corresponding to time frame n
F	Fourier transform operator
P_{FOV}	projection onto the field of view
$x_{n,m}$	estimated solution of x_n at the $(m-1)^{th}$ iteration
$dx_{n,m}$	solution update for x_n calculated in the m^{th} iteration

An updated solution $x_{n,m+1}$ is $x_{n,m} + dx_{n,m}$. Eq [3.2] can be solved using the following minimization:

$$min\left\| dE_n/dx(x_{n,m})dx_{n,m} - (y_n - E_n(x_{n,m}))\right\|^2 \quad [3.3]$$

By adding a limited regularization term to Eq [3.3], the solving process becomes the well-known Levenberg-Marquardt (LM) algorithm or Iteratively Regularized Gauss-Newton Method (IRGNM) (13-15). In the LM algorithm, a term $\mu_{n,m}\|dx_{n,m}\|^2$ is added to Eq [3.3]. This constrains the solution of the current iteration to be close to that of

the previous iteration. Then the problem becomes:

$$\min \quad \left\| dE_n/dx\left(x_{n,m}\right)dx_{n,m} - \left(y_n - E_n(x_{n,m})\right)\right\|^2 + \mu_{n,m}\left\|dx_{n,m}\right\|^2 \qquad [3.4]$$

In the IRGNM algorithm, a term $\mu_{n,m}||x_{n,m} + dx_{n,m} - x_{n,0}||^2$ is added to Eq [3.3]. This constrains the solution of the current iteration to be close to the initial guess $x_{n,0}$. Then the problem becomes:

$$\begin{aligned} \min \quad & \left\| dE_n/dx\left(x_{n,m}\right)dx_{n,m} - \left(y_n - E_n(x_{n,m})\right)\right\|^2 \\ & + \mu_{n,m}\left\|x_{n,m} + dx_{n,m} - x_{n,0}\right\|^2 \end{aligned} \qquad [3.5]$$

In both algorithms, $\mu_{n,m}$ is reduced by half in each iteration (13-15). In preliminary testing, these two algorithms were compared to select an appropriate solver for the remainder of the reconstructions.

The minimization in Eq [3.5] is a linear problem solved using a conjugate gradient solver. As coil sensitivities vary smoothly in space, the high spatial frequency components are constrained by adding a weighting matrix W to c_n (11). In this work, the iteration was stopped when $||dx_{n,k}|| > ||dx_{n,k-1}||$ and $x_{n,k-1}$ was taken to be the reconstructed image at time point n, ie, $x_n = x_{n,k-1}$. The final reconstructed image is $x_n = \rho_n \cdot \sqrt{(\sum c_{n,i}^2)}$ as in (11). In dynamic imaging, the initial guess $x_{n,0}$ is taken to be the reconstructed image x_{n-1} at time point $n - 1$. This algorithm is applied in situations where the difference between successive time points is sufficiently small such that the image update $dx_{n,m}$ can still be found despite the high under-sampling. In TRACER, we applied this algorithm to a 3D stack of spirals sampling method using golden ratio

updating. A single spiral leaf y_n (acquired for each slice encoding) is used to update a 3D volume x_n.

3.3 Data Acquisition

A 3D fast spoiled gradient echo stack of spirals sequence with partial Fourier slice encoding is used for data acquisition (16). A spectrally selective inversion pulse combined with a segmented view order is employed to provide fat suppression (3,16,17). For a fully sampled k_x-k_y plane using 48 spirals, this spiral trajectory has a variable density such that the k-space is oversampled two-fold in the center while under-sampled by a factor of 0.7 at the edge (18,19). Consecutive spiral leafs are rotated by the golden ratio angle of 220° (20,21) such that each new spiral leaf is sampling a substantially different part of k-space compared to the immediately preceding leaf. For each spiral leaf, a full set of slice encodings (partially encoded) is acquired.

3.4 Image Reconstruction

A fully sampled k-space, consisting of 48 leaves, can be acquired before the arrival of contrast agent and used to reconstruct a pre-contrast volume (x_0) which serves as the initial guess $x_{1,0}$ for the reconstruction of the first dynamic frame. For the reconstruction of x_0, the initial guess $x_{0,0}$ is taken to be a matrix of ones for ρ and a matrix of zeros for each c_j (10). A scaling factor λ is calculated such that $\|F^{-1}(\lambda y)\| \approx \|F^{-1}P_0F(I)\|$, where I is a vector containing an image for each coil that has all pixels set to one. This λ is used to rescale all raw data y in the remainder of the reconstruction,

which in preliminary testing was found to ensure good convergence. The parameter $\mu_{0,0}$ needed in the LM algorithm is estimated by requiring that $\|(dE/dx(x_{0,0}))^H\ dE/dx(x_{0,0})I\| \times 10 \approx \|\mu_{0,0}I\|$. For the under-sampled reconstructions of the successive time frames $n > 0$, the parameter $\mu_{n,0}$ is selected differently. First, $\mu_{1,0}$ is chosen to satisfy $\|(dE/dx(x_{1,0}))^H\ dE/dx(x_{1,0})\sigma\| \approx \|\mu_{1,0}I\|$ while $\mu_{n,0}$ is set equal to this $\mu_{1,0}$ for all other time frames $n > 1$. Again, this selection of the solver parameter was found to provide good convergence in preliminary testing. In the calculations, the damping factor decreases as follows: $\mu_{n,m} = \mu_{n,m-1}/2$. Reconstructed images are temporally filtered using a median filter (window size 5) to eliminate time dependent residual spiral artifacts. Solving Eq [3.4] using the conjugate gradient method requires gridding each coil image to a spiral k-space followed by gridding it back to image space. This process can be simplified by convolving the image with the point spread function of the sampling trajectory (22). Here a Kaiser-Bessel kernel width of 6 and oversampling factor of 3 were used. A smaller kernel width or oversampling factor was, in preliminary testing, found to result in appreciable accumulated error through the iterations due to errors in approximating the gridding-regridding operation with a convolution. The shape parameter of the Kaiser-Bessel kernel is computed according to Beatty et al. (23). All reconstruction parameters (the raw data scaling factor λ, and the solver parameter $\mu_{n,m}$) were determined from the acquired raw data in the same manner for all numerical, phantom and in vivo experiments. In some experiments with possible contrast enhancement in the fully sampled dataset (constructed from the first 48 spiral leaves), the dynamic reconstruction was started from the 48th spiral leaf, but run backwards in time to the 1st spiral leaf. This allowed obtaining the early

unenhanced frames, from which the reconstruction was then performed normally in the forward direction.

3.5 Temporal Footprint

3.5.1 Experiment design

The temporal footprint of a single image in dynamic imaging may be defined as the temporal interval from which raw data is used for the reconstruction of that image (24). As TRACER updates the current frame with the raw data from the corresponding spiral leaf and an initial guess equal to the previous time frame, each constructed frame depends on all previous frames. It is expected that when more and more raw data is used, frames that are farther apart in time will contribute less. In order to determine this dependence, the temporal footprint was defined using the response to a temporal impulse function. As the variable density spiral sampling covers the central region of k-space more often than the outer region, the temporal footprint is expected to vary with the k-space radius. A numerical dynamic phantom (Figure 3.1) with 60 frames was built. In the k_x-k_y plane, the phantom had only non-zero spatial frequency components inside a disk with radius r and an annulus with fixed width d but varying outer radius R. The k-space signal inside this annulus was constant and equal to one in all frames except for frame 13, in which it was set to two, representing an impulse input function in time.

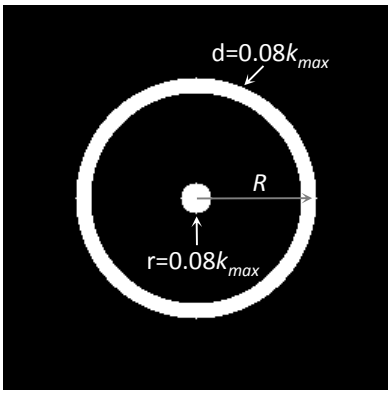

Figure 3.1 k-space numerical phantom
The central disk has a radius of $0.08k_{\max}$ and constant signal of 1 in all 60 frames. The outer annulus has a constant signal of 1 in all frames except for frame 13 where the signal is set to 2, representing an impulse input function. The outer radius R of the annulus varies from $0.08k_{\max}$ to $k_{\max}$.

The first frame was sampled along a fully sampled spiral trajectory (48 leaves) such that a high quality initial frame could be reconstructed. Each successive time frame was sampled using one spiral leaf with successive spiral leaves rotated using the golden ratio angle as before. The impulse response was calculated by Fourier transforming the reconstructed images and taking the average of the signal on the k-space annulus, excluding the central k-space disk. An exponential function was fit to the impulse response and the temporal footprint was calculated as four times the exponential decay time constant corresponding to a decrease in signal of over 98%. This temporal footprint analysis in k-space was complemented by a similar analysis in image space. A 60-frame dynamic phantom consisting of a single disc at the center of the image with diameter varied from 0.08 × FOV to FOV was built. A temporal impulse function similar to the one above was applied and an exponential function was fit to the impulse response to get the temporal footprint. All the temporal footprint results were expressed in frames assuming a temporal frame rate of 0.22 s

(corresponding to TR = 7 ms and 32 slice encodings, parameters close to those in a typical patient study).

3.5.2 Result

Figure 3.2a shows the impulse response when the outer radius of the k-space annulus is $0.08k_{max}$ (10 pixels for reconstructed matrix size 256 × 256). At frame 13, the impulse response reaches about 60% of the impulse input magnitude and decays quickly to base signal in about 5 frames (1.1 s). Signal drop occurred at frame numbers that were approximately equal to the frame number corresponding to the impulse (frame 13) plus a Fibonacci number. Figure 3.2b shows the temporal footprint of the k-space annulus as a function of its outer radius. The temporal footprint increases approximately linearly with the spatial frequency radius. When the radius reaches k_{max}, the temporal footprint is 12.7 frames (2.8 s). Figure 3.2c shows the temporal footprint of a disk in image space as a function of its diameter. The temporal footprint decreases as the diameter increases due to the decreased contribution of high frequency components. This agrees with results in Figure 3.2b.

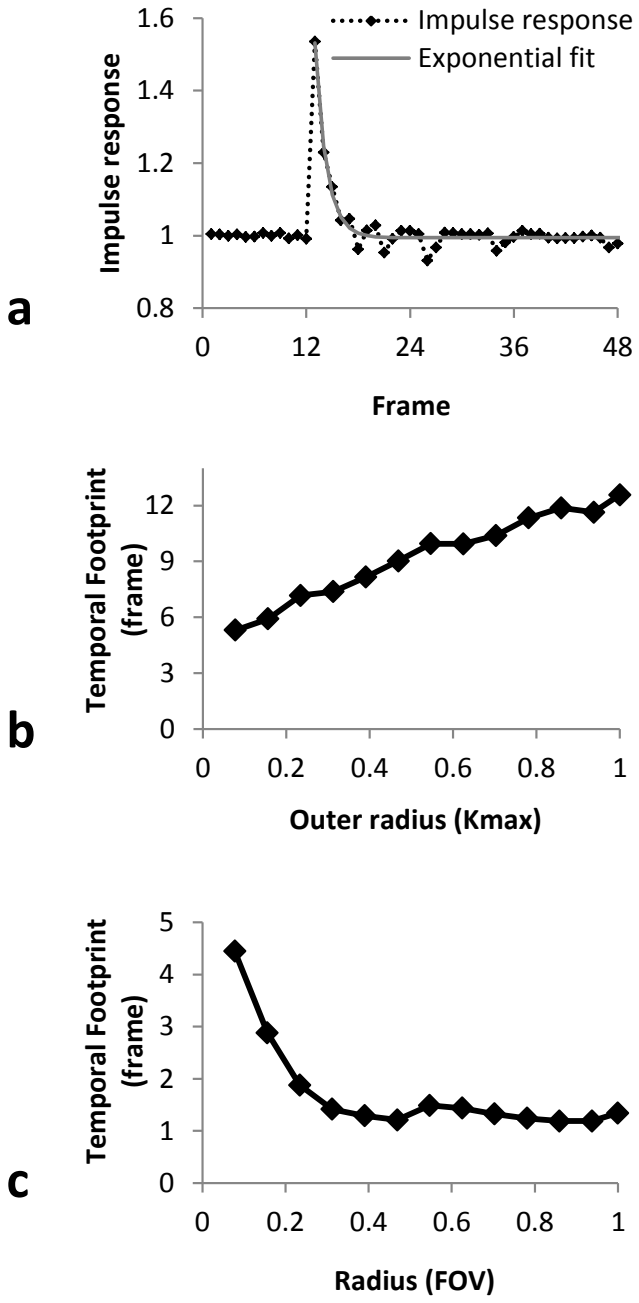

Figure 3.2 Temporal footprint analysis
(a) Impulse response when the outer radius of the k-space annulus is $0.08k_{max}$. The impulse response has an exponential decay with time constant of 1.23 frames corresponding to a temporal footprint of 5 frames (1.1 s). **(b)** Temporal footprint as a function of the outer radius of a k-space annulus with non-zero signal. The temporal footprint increases linearly with the spatial frequency up to 12.7 frames (2.7 s). **(c)** Temporal footprint as a function of the diameter of an image space disk. The temporal footprint decreases with the diameter.

3.6 Contrast Enhancement Simulation

3.6.1 Numerical liver phantom

A numerical dynamic phantom was constructed to simulate liver contrast enhancement (Figure 3.3). It contains liver, portal vein (PV), aorta, inferior vena cava (IVC) and pancreas with enhancement kinetics modeled from Bae et al. (25) according to a compartmental model of the cardiovascular system. A contrast injection rate of 2 ml/s and a cardiac output varying from 4 to 8 L/min were chosen for modeling. Based on in vivo scan parameters (reconstructed temporal resolution, tissue relaxation time and spiral sequence parameters as shown in Table 3.2), dynamic reference images were created after which noise was added.

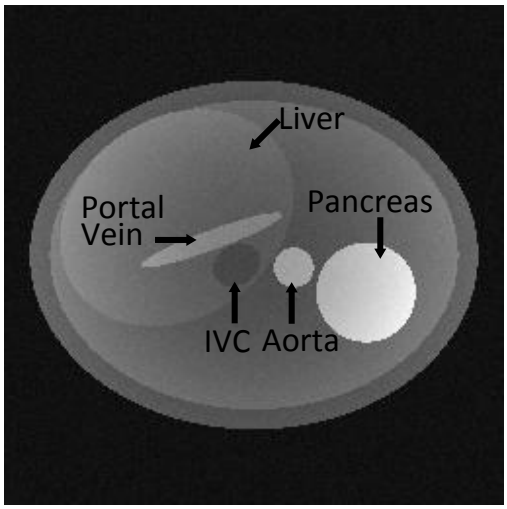

Figure 3.3 Numerical dynamic liver phantom
Labeld are liver, aorta, portal vein, inferior vena cava and pancreas, where contrast enhancment curves are measured.

3.6.2 Algorithm comparison

LM and IRGNM were compared in the numerical liver phantom for a reconstruction from a fully sampled set of spiral leaves. The logarithm of the residual (defined as $\|y -$

$E(x)||/||y||$) and the update dx through the first 10 iterations are shown in Figure 3.4.

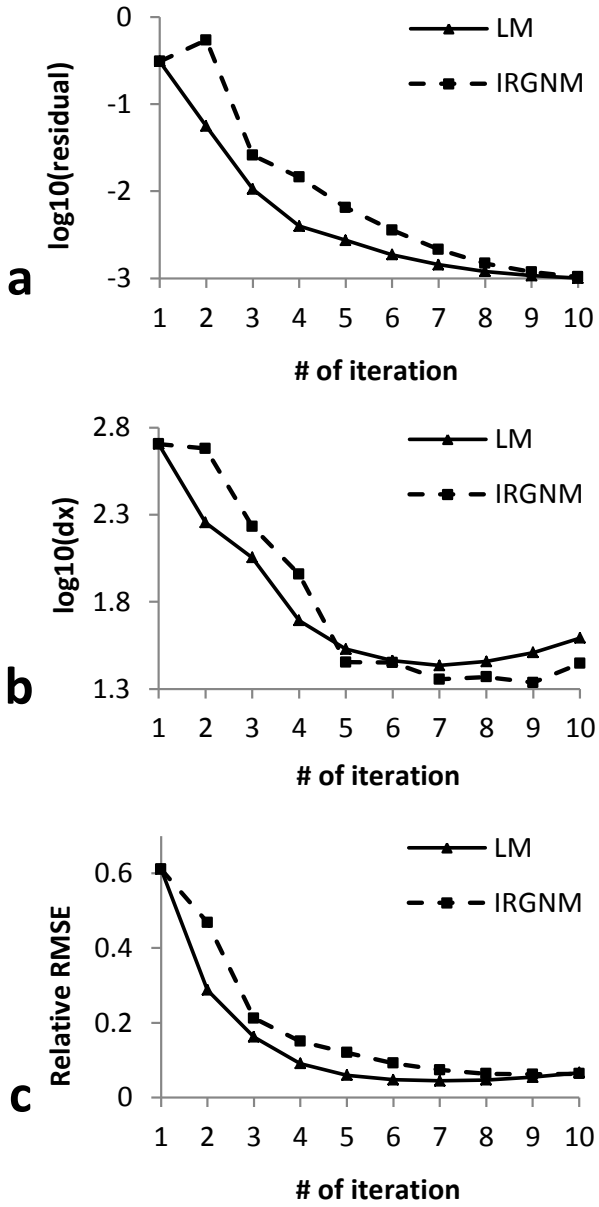

Figure 3.4 Comparison of the LM and IRGNM algorithms
(a) The logarithm of residual (defined as $||y - E(x)||/||y||$) for each iteration. (b) The logarithm of the solution update dx for each iteration. **(c)** The relative root mean square error (RMSE) of reconstructed image at each iteration compared with the reference image.

Figure 3.4a shows the LM algorithm has a faster convergence rate and lower residual

than IRGNM algorithm through the iterations. In Figure 3.4b, the *dx* decreases monotonically to its minimum for the LM algorithm and monotonically increases afterwards. This minimum corresponds to a reconstruction with the lowest relative root mean square error (RMSE) with respect to the reference image (Figure 3.4c). IRGNM shows a consistently higher relative RMSE in Figure 3.4c compared to LM. Therefore, in the remainder of the experiments, the LM algorithm was used combining with a stopping criterion that identifies the iteration with the smallest update *dx*.

3.6.3 Contrast enhancement

Tissue enhancement curves from the reference dynamic images and those from TRACER were compared using ROI analysis in the liver, aorta, portal vein and IVC. When modeling cardiac output of 7 L/min, 30 dynamic data sets were constructed, each with different noise having the same distribution, but otherwise identical. The TRACER method was performed on each of these data sets and pixel-by-pixel noise was calculated by taking the standard deviation of each pixel across these 30 experiments. Signal to noise ratio of the aorta (SNR_{aorta} = mean aorta signal/mean aorta noise) and portal vein (SNR_{PV} = mean portal vein signal/mean portal vein noise) was calculated.

Multi-phase sliding window (26) images were created using fully sampled (~11s) datasets with a 3s temporal update rate. A second sliding window reconstruction was performed in which a k-space mask was applied such that the effective FOV for each k-space region was equal to or smaller than the prescribed FOV. This effectively applied a temporal filter to the spiral data similar to that previously used in real-time

spiral imaging (19), and to the "tornado" filter (27) and KWIC method used in radial imaging (28). This filter limits the temporal window from which data (especially in the central k-space region) is used for reconstruction. Since a oversampling of two was used for the spiral trajectory near the center of k-space, this means that, for image reconstruction, the center of k-space was taken from a temporal window that is half as wide (~5s) compared to the edge of k-space (~11s). The SNR of these two sliding window reconstructions was calculated in the same manner as in TRACER. Aorta to portal vein contrast to noise ratio (CNR) was defined as $SNR_{aorta} - SNR_{PV}$ and compared between TRACER and multi-phase sliding window images.

Figure 3.5a shows the contrast enhancement curves derived from reference images and TRACER images in aorta, liver, portal vein and IVC in the numerical phantom. The reconstructed curves preserve the shape and trend of the signal and narrowly follow the reference curves. A delay was found in the fast changing part of the aorta and portal vein enhancement curves. In the liver, this delay is smaller due to its relatively slow signal change. This delay reaches the maximum where the signal change is highest and shrinks near peak enhancement. Since the steepness of the enhancement curves increases with increasing cardiac output, the delays of each tissue under different cardiac output conditions were calculated as well and shown in Figure 3.5b. Liver parenchyma has the smallest delay of about 0.1 s. Aorta, portal vein and IVC have delays around 1.5 s which do not vary much with cardiac output. Figure 3.5c shows the aorta to portal vein CNR of images reconstructed from TRACER and multi-phase sliding window images through time. The peak CNR from TRACER

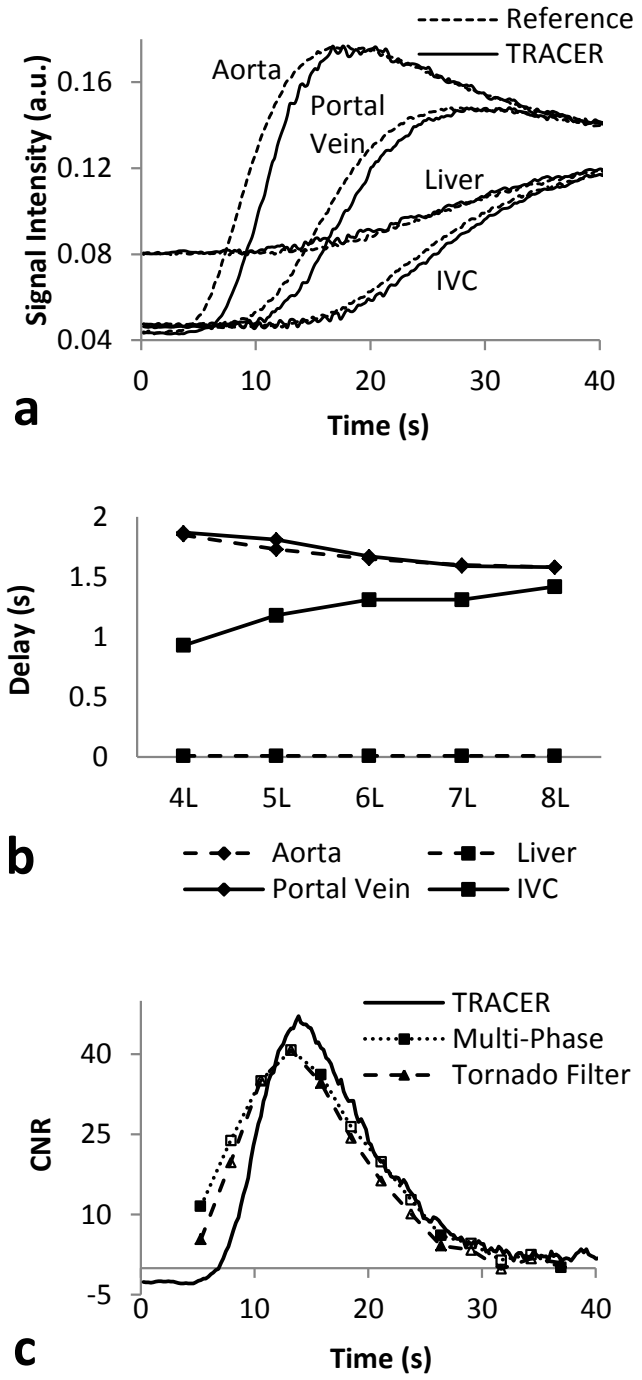

Figure 3.5 Contrast enhancement comparison
(a) Enhancement curves of aorta, portal vein, liver, IVC at 7 L/min cardiac output derived from TRACER images and reference images. **(b)** Delay of enhancement curves derived from TRACER compared with the reference under various simulated cardiac outputs. **(c)** Aorta to portal vein CNR of TRACER images and multi-phase sliding window images (with and without a tornado like filter).

method was 16% higher than that from multi-phase sliding window images and multi-phase sliding window images with a tornado filter at aorta peak enhancement which corresponds to the optimal arterial phase.

The tornado like filter in the sliding window reconstruction effectively reduced the view sharing effect, thus narrowing the CNR peak compared to the sliding window reconstruction. However, as less data was used for reconstruction, noise increases and the peak CNR remained similar to that of the unfiltered sliding window reconstruction. Therefore, in the remaining experiments, only the sliding window reconstruction was performed as a comparison.

3.6.4 Edge sharpness

To assess the edge sharpness during the dynamic reconstruction, the aorta diameter was measured for each time frame by taking the gradient of the reconstructed image, plotting the signal along a line across the aorta and measuring the distance between the two peaks representing the edges on either side of the aorta.

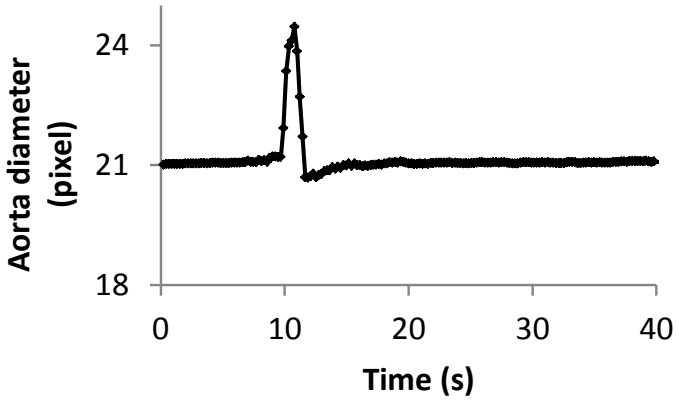

Figure 3.6 Aorta diameter

Figure 3.6 shows the aorta diameter as a function of time. When contrast arrived in

the aorta, the diameter had a maximal error of about 3 pixels within a period of about 10 frames (2.2 s), coinciding with the arrival of contrast in the aorta. In the rest of the frames, the aorta diameter remained unchanged.

To investigate the influence of the image quality of the initial image on the performance of the TRACER method, two additional TRACER reconstructions (each repeated 30 times as above) were performed. In these reconstructions, the standard deviation of the simulated noise for the initial image was increased by 50% and 100%, respectively, while the noise level of the remaining simulated spiral data was kept the same. Aorta to portal vein contrast to noise ratio was measured as above. The noise behavior of TRACER images with different levels of noise in the initial frame is shown in Figure 3.7a. With a 50% and 100% increase in noise for the initial frame, the noise decreased through the dynamic reconstruction in TRACER. It converged to the noise level of the reconstruction without the additional noise in the initial frame. The relative RMSE of the dynamic images showed a similar behavior (Figure 3.7b).

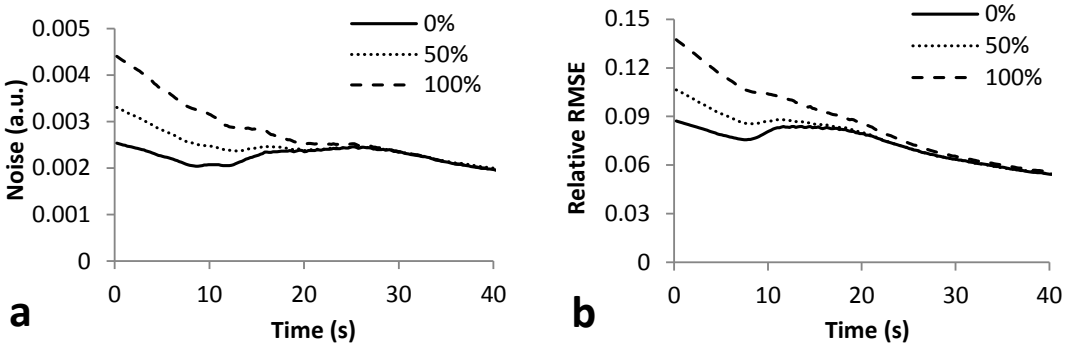

Figure 3.7 Noise behavior of TRACER images
(a) Noise behavior of TRACER images through time with different noise levels for the initial image : 0%, 50%, and 100% increase in noise standard deviation of the initial image compared to the rest of the simulated spiral data. Shown is the noise measured in the aorta. The initial higher noise level decreased with time and finally converged to that of the reconstruction using an initial image without the additional noise. **(b)** The

relative RMSE of reconstructed images in a) compared with the truth. The error also decreased as the dynamic reconstruction progresses.

3.7 Scan Parameters

Scan parameters for experiments performed in the following of this chapter is listed in Table 3.2.

Table 3.2 Scan parameters in flow phantom, moving phantom and in vivo scans

Parameter	Moving Phantom		Flow Phantom			In Vivo
	3D spiral	2D EPI	Phase contrast	3D spiral	2D EPI	3D spiral
TR/TE(ms)	6.2/0.6	6/1.5	8.6/4.2	7.2/0.6	4.2/1.2	7.2/0.6
Flip angle	15˚	15˚	25˚	15˚	20˚	15˚
Band Width (KHz)	±125	±62.5	±31.25	±125	±62.5	±125
Field of view (mm)	320	320	300	420	420	340
Slice Thickness (mm)	5	5	10	5	30	5
Matrix size	256 ×256 ×8,16,32	128 ×64	256 ×128	256 ×256 × 32	128 ×64	256 ×256 ×36-50
VENC			30cm/s			
Temporal frame rate (ms)	63, 104, 198	147		198	147	220

3.8 Moving Object Experiment

3.8.1 Experiment design

A set of moving phantom experiments were performed to examine the sensitivity of TRACER to various magnitudes of motion. In the experiments, a syringe filled with contrast agent was moving in and out of the field of view which contained a set of static phantoms. The motion of the syringe was driven by a programmable motor. The moving range was 38 mm at velocities of 2, 4, 6, 8, 10, 12, and 14 mm/s. The spiral

acquisition parameters are listed in Table 3.2. For each velocity, the acquisition was performed multiple times with different temporal frame rates, equal to 63 ms, 104 ms and 198 ms by changing the number of slice encodings. For each velocity, the phantom was additionally imaged using a multi-phase 2D EPI sequence (Table 3.2) to obtain a reference dynamic image set. For all experiments, an ROI around the syringe was selected and its frame-to-frame motion was computed using a cross-correlation registration algorithm (29). Displacement curves of the TRACER images, multi-phase sliding window images and 2D reference images were compared to investigate the reconstruction fidelity.

3.8.2 Results

TRACER images could faithfully record the motion of the moving phantom at various velocities. At the 198 ms reconstruction temporal frame rate, which is similar to the one obtained in the human study, the dynamic image set from low velocity experiments only show small spiral ringing artifacts as shown in Figure 3.8. The overall shape was well resolved. In contrast, the image from multi-phase sliding window imaging was temporal blurred and show substantial motion artifacts.

The position curve derived from the TRACER images narrowly follows the reference as shown in Figure 3.9. A constant time lag of about half second is seen between two curves, corresponding to a position lag of less than 3mm or 2 pixels. The curve from multi-phase sliding window images leads the reference curve and the peak position is smaller than that of the reference due to temporal blurring.

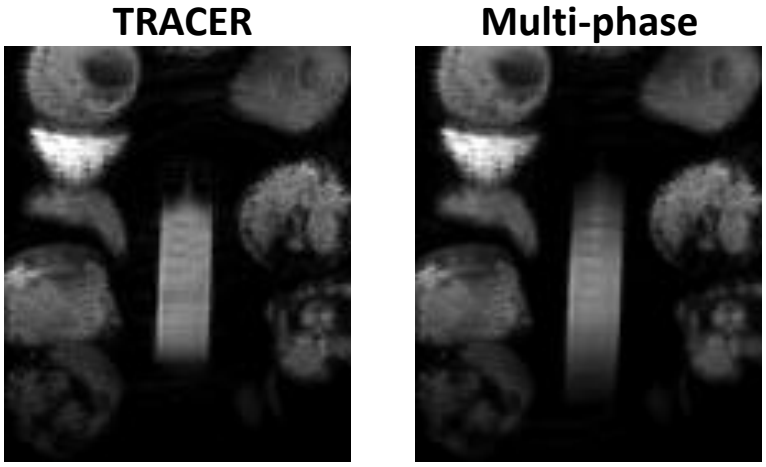

Figure 3.8 Comparison between TRACER and Multi-phase
One frame from dynamic image set reconstructed using TRACER at a temporal frame rate of 198 ms (velocity 4 mm/s) and corresponding frame from multi-phase imaging. At this velocity, the movement could be tracked with minor spiral ringing artifacts seen inside the syringe. The multi-phase image has severe motion artifact due to temporal blurring.

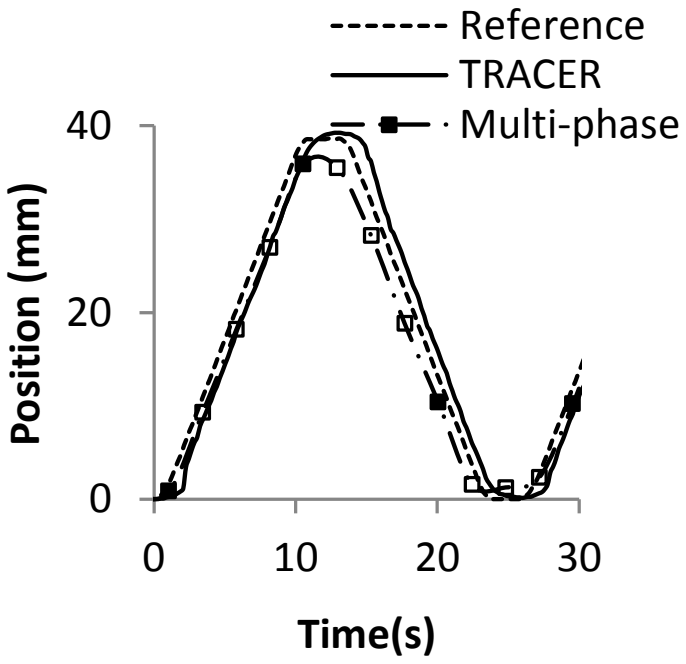

Figure 3.9 Moving phantom position-time curve
TRACER images can track the motion during the whole experiment with a constant lag during the movement stage. Multi-phase sliding window curve leads the reference and has a smaller maximum position compared with reference and TRACER.

For all TRACER experiments, position lag increases with moving velocity and reconstructed temporal frame rate as shown in Figure 3.10. This lag is less than 4mm for all image sets reconstructed at 63, 104 ms temporal frame rates. For the 198 ms temporal frame rate, a large position lag and severe artifacts were seen when velocity increased beyond 6 mm/s.

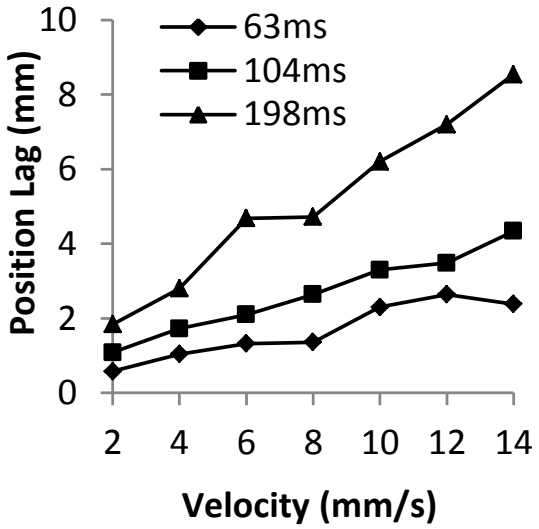

Figure 3.10 Reconstruction lag
Lag in position as a function of velocity and reconstructed temporal frame rate. The position lag increases with velocity and reconstructed temporal frame rate.

3.9 Flow Phantom Experiment

3.9.1 Experiment design

A flow phantom experiment was performed to mimic liver vascular enhancement. A long U shaped plastic tube, through which tap water was flowing, was fixed on a board on top of the scanner table. A power injector was used to inject contrast agent into the flowing water. According to (30), maximum blood flow velocity in portal vein is around 15 cm/s, to which the speed of the flowing water was set. This speed was

confirmed using a 2D phase contrast study (Table 3.2). Contrast flow was imaged using a multi-phase 2D EPI sequence as well as the 3D spiral sequence (Table 3.2). The 2D images were used to obtain a dynamic image set from which the reference intensity change due to contrast flow was derived.

3.9.2 Visual comparison

In Figure 3.11, by comparing TRACER and reference images at the same time after contrast injection, it can be observed that TRACER faithfully records the bolus at this thick slab coverage and high spatial resolution (32 slices, slice thickness 5 mm)

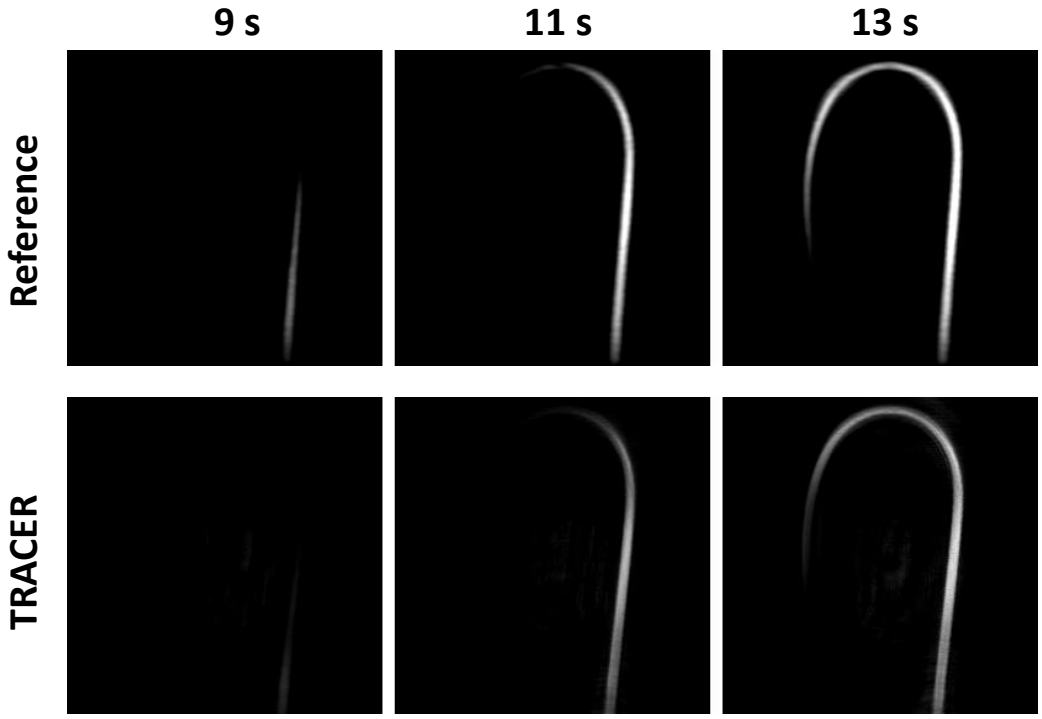

Figure 3.11 Reconstruction fidelity of TRACER
Contrast bolus at 9, 11 and 13 s after injection. TRACER images could faithfully represent the bolus position. TRACER images achieved similar temporal frame rate as the reference 2D images while maintaining higher spatial resolution, coverage and SNR.

3.9.3 Enhancement curve

TRACER and multi-phase sliding window images were reconstructed from the 3D dataset and the contrast flow enhancement curves were derived. These enhancement curves were derived from an ROI positioned inside the tube on both the 2D images and the 3D images at approximately the same location. For all reconstructions, the first (pre-contrast) frame was subtracted from all subsequent frames, allowing a clear visualization of the contrast bolus behavior. The result is shown in Figure 3.12.

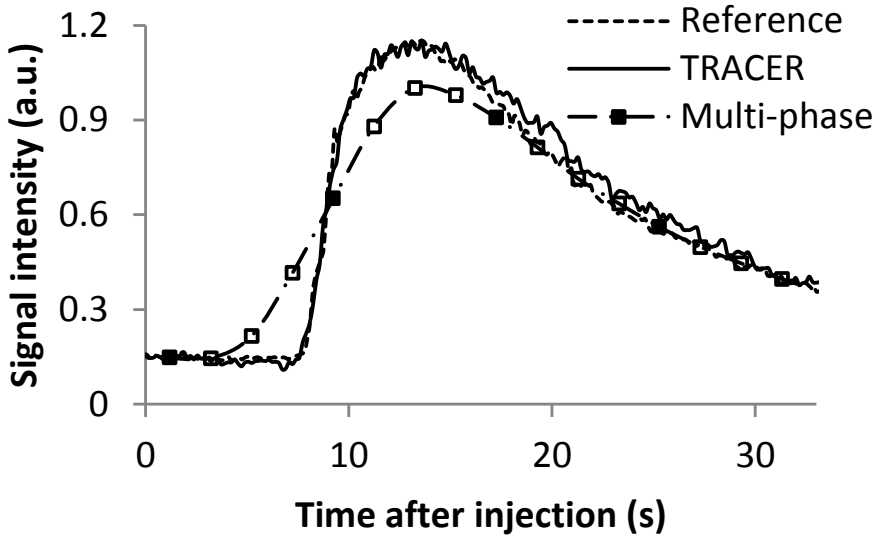

Figure 3.12 Contrast enhancement curve comparison
TRACER enhancement curve closely follows that derived from reference image set. Multi-phase sliding window images at the same cross section is temporal smoothened and blurred, resulting in a decreased peak signal.

The signal intensity over time at an ROI near the inlet of the tube narrowly follows the signal obtained in approximately the same ROI on the 2D dynamic images. Even in the fast signal rising region from 8 to 12 s, the signal curve difference is negligible. Some ringing artifacts due to highly under-sampled spirals were observed around the tube but do not affect the overall image quality. The temporal blurring effect is seen in

the multi-phase sliding window images. Contrast bolus enhancement curves are smoothed over time with reduced peak intensity.

3.10 In Vivo Study

3.10.1 Scan protocol

This study was institutional review board approved and HIPPA-compliant. Three healthy volunteers (all men, aged 23 years) were imaged after obtaining informed consent and anonymized. Raw Fourier image data was obtained from 18 consecutive patients undergoing abdominal MRI with indications related to liver pathology in our institute (from February 23rd, 2011 to March 22nd, 2011, 6 men aged 35-62 years, mean age 53 years and 12 women aged 42-82 years, mean age 56 years). For human scans, 20 ml of Gd-DTPA (volunteers) or 10 ml Gadoxetate (patients) was injected 8-10 s after scan initiation, which, in general, allowed for an acquisition of an initial data set before contrast arrival that was at most two-fold under-sampled (24 leaves) but was in most cases fully sampled (48 leaves). For healthy volunteers, the breath hold was as long as possible up to a total scan time of 80 s. For the patients, the scan time was 33 s. For all cases, a dynamic image data set was reconstructed using one single spiral leaf and the previous frame as the initial guess for the TRACER reconstruction, resulting in a temporal frame rate of approximately 220 ms. Multi-phase sliding window reconstructions with a 3 s temporal update rate were performed as well.

3.10.2 Dynamic liver images

One patient dataset was eliminated due to severe respiration motion induced artifact.

All other 4D datasets were successfully reconstructed. For the 33 s breath-hold studies, 144 frames were created which captured the arterial phase. For the volunteer study with longer breath hold, the portal venous phase appeared around 50 s after contrast injection. From the high temporal frame rate dynamic image sets, small respiratory motion and stomach peristalsis were observed without motion artifacts. Inspecting the same anatomical location at high temporal frame rate provided an uninterrupted view of all liver tissue dynamic changes (see Supplementary video). An optimal arterial phase with only the hepatic artery enhancing was reconstructed in all cases. Optimal arterial and portal venous phases were retrospectively selected by looking at all the temporal phases of a few slices that cover both the aorta and hepatic artery (Figure 3.13a).

Temporally distinct tissue enhancements were observed for the aorta, hepatic artery, kidney, spleen, portal vein, inferior vena cava, and liver parenchyma. In the spleen, the typical spatially varying enhancement pattern was well visualized. In a patient with hepatocellular carcinoma, gradual arterial enhancement of the tumor was observed (Figure 3.13b).The arterial enhancement of the tumor could be confidently identified with the high temporal resolution of TRACER and the consequent detailed depiction of the enhancement evolution. In one study, the patient failed to follow the breath-hold instruction during the scan and continued shallow free breathing. Despite ringing artifacts, TRACER was still able to produce diagnostic images (Figure 3.13c).

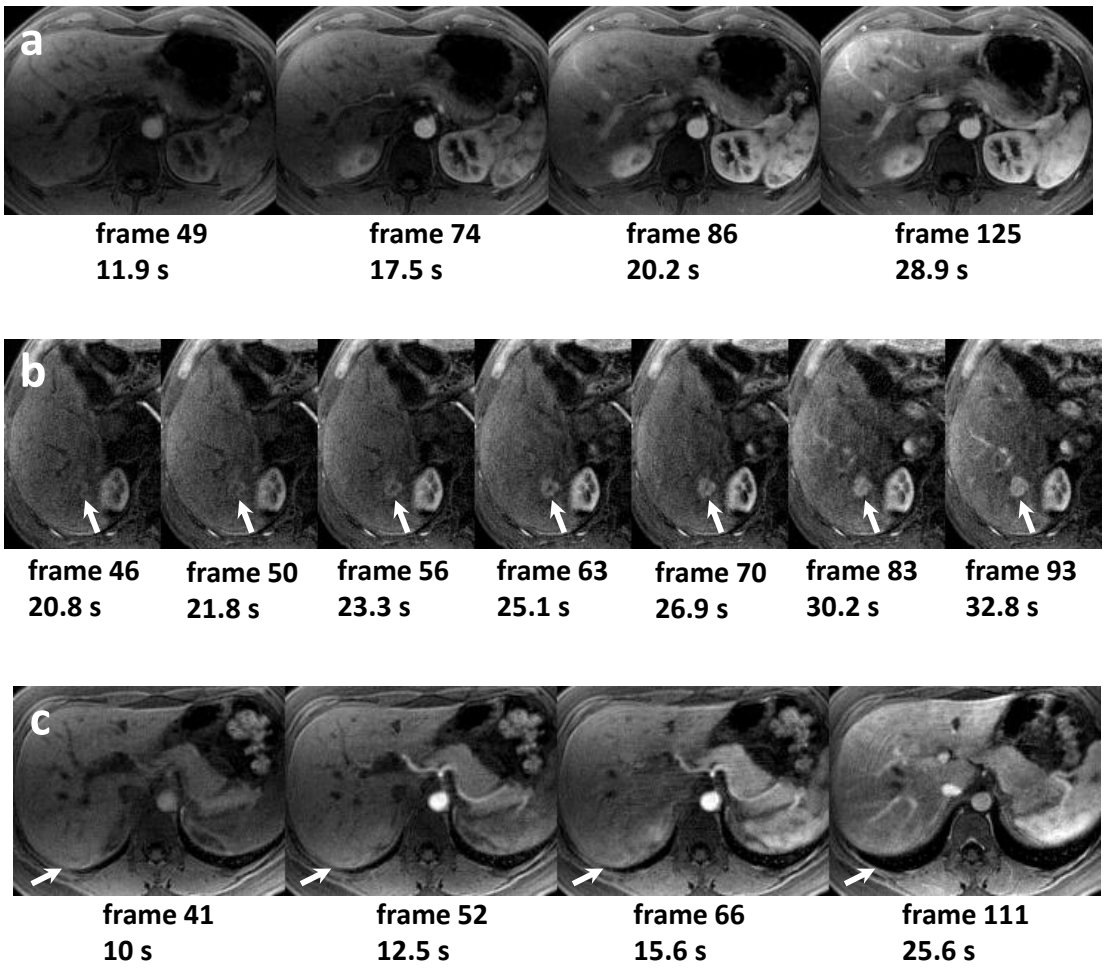

Figure 3.13 Retrospectively selected optimal arterial phases and sub-phases Each image is labeled with its frame number and acquisition time after scan initiation. **(a)** A healthy volunteer study showing start of arterial enhancement, optimal arterial phase, and two late sub-phases. **(b)** A hepatocellular carcinoma case showing the arterial enhancement of the tumor (arrows indicated). Retrospectively selected sub arterial phases depicted the gradual tumor enhancement evolution. **(c)** A liver donor patient who failed to follow instructions and performed shallow breathing instead. Four phases from an early arterial phase to early portal venous phase are shown to illustrate the possibility to retrospectively select optimal sub-phases. Due to diaphragm motion, the liver position changed noticeably during the scan (arrows indicated).

3.10.3 Quantitative analysis

To assess the quality of the optimal arterial phase, hepatic artery to portal vein CNR

was compared between TRACER images and multi-phase sliding window images. To get accurate signal measurement within a larger ROI, the aorta was used as a substitute of the hepatic artery. One slice containing the main portal vein was selected for measurement. The CNR was derived as mean signal intensity difference between aorta and portal vein divided by the standard deviation of an ROI containing homogeneous liver tissue near both the aorta and the portal vein, which was done to approximate the local noise characteristics in this parallel imaging study. The Student's t-test was used to compare peak CNR obtained with TRACER and with the multi-phase sliding window method.

TRACER reconstructions had significantly higher aorta to portal vein CNR compared to multi-phase sliding window images ($P < 0.001$). Peak aorta to portal vein CNR was $31 \pm 27\%$ higher for the TRACER reconstruction compared to that of the sliding window reconstruction, corresponding to a range between 9% and 133%. In 14 cases, the CNR increase was over 20%.

The peak aorta to portal vein CNR occurred during the arterial phase before the portal vein enhanced. It could be missed in multi-phases sliding window images when the hepatic artery is not fully enhanced or the portal vein has already enhanced as shown in Figure 3.14. Instead, the TRACER technique gives higher aorta to portal vein CNR and a better visual differentiation between hepatic artery and portal vein.

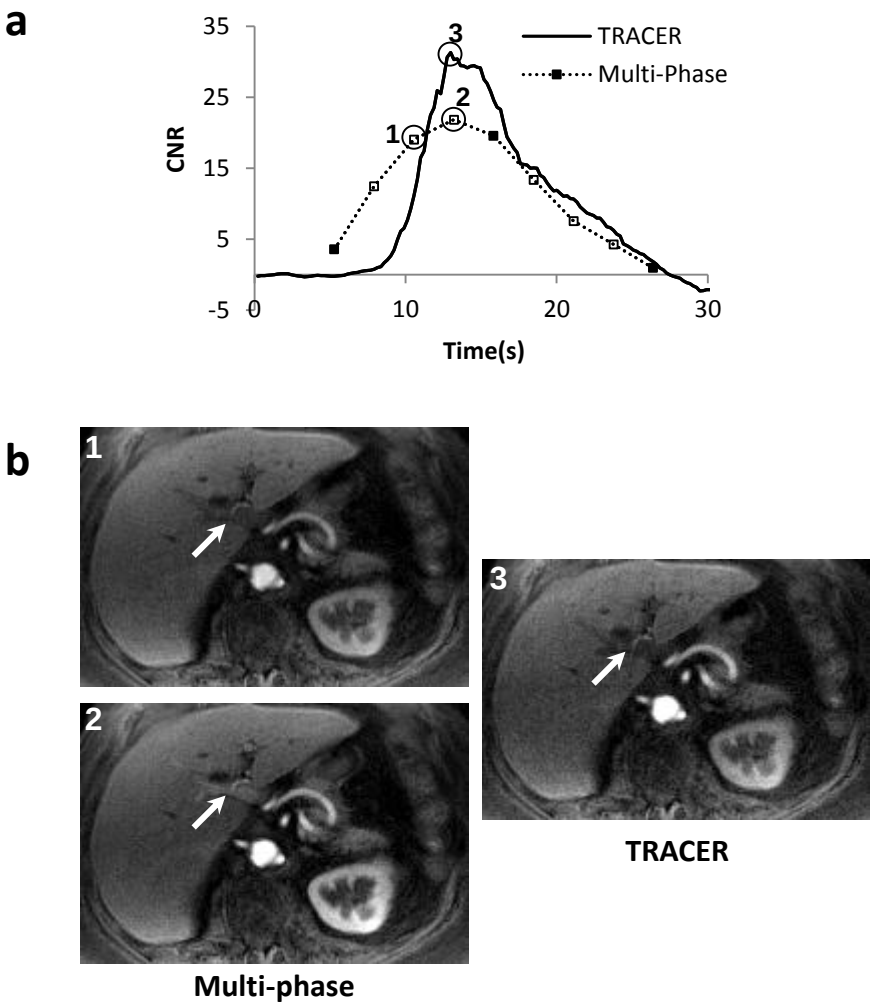

Figure 3.14 TRACER shows improved aorta-to portal vein CNR
(a) CNR of TRACER and multi-phase sliding window images. (Solid markers represent multi-phase and hollow markers represent additional phases by sliding window reconstruction). The TRACER image set has a 44% aorta to portal vein peak CNR increase compared to the multi-phase images. **(b)** Arrows indicate a region where both hepatic artery and portal vein could be seen. The peak aorta to portal vein CNR was at a time (labeled as 3) when aorta was around its highest signal and portal vein has not enhanced. In multi-phase images, the two arterial phases had lower aorta to portal vein CNR. In one phase (labeled as 1), the hepatic artery was not fully enhanced and appears dim. In the other phase (labeled as 2), the portal vein has enhanced thus contaminating the arterial phase.

In one study, the scan initiation was delayed by around 5 seconds due to an unexpectedly long breath hold instruction. The pure arterial phase was missed using the multi-phase sliding window reconstruction but TRACER reconstruction still provided a high quality arterial phase as shown in Figure 3.15.

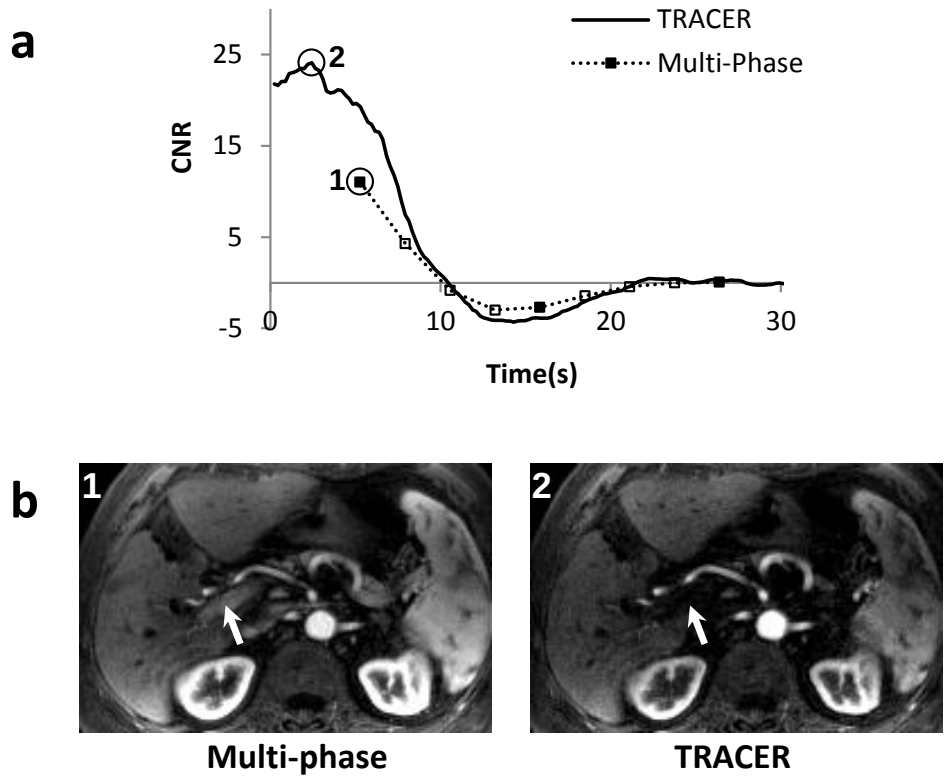

Figure 3.15 Recovering missing arterial phase from TRACER
Missing arterial phase in multi-phase images could be retrospectively selected in TRACER images for a delayed scan initiation study. **(a)** Maximum aorta to portal vein CNR of multi-phase images is only half of the CNR in TRACER images. **(b)** Due to signal average effect, portal vein enhancement is seen in all multi-phase images. Even the phase with maximum aorta to portal vein CNR was contaminated by portal vein enhancement (arrow), whereas TRACER was still able to give a high quality arterial phase, with the portal vein (arrow) not yet enhanced.

3.11 Discussion

Our preliminary data tends to confirm that the nonlinear Temporal Resolution Acceleration with Constrained Evolution Reconstruction (TRACER) can shorten the

temporal footprint of time resolved imaging. Our study specifically demonstrates the feasibility of using a 3D golden ratio spiral acquisition with TRACER reconstruction to achieve high temporal frame rates for whole liver imaging at a spatial resolution normally requiring around 11 seconds of data sampling. This ensures that optimal arterial sub-phases can be selected retrospectively, thereby eliminating bolus timing errors and may ultimately allow studying contrast enhancement kinetics at a new level of temporal-spatial details. The temporal fidelity and dynamic tracking capability were validated by numerical, flow and motion phantom experiments. Increased peak aorta to portal vein CNR compared to a sliding window reconstruction was demonstrated in vivo.

Hepatic arterial and portal venous sources of blood to the liver are briefly separated in time which allows distinguishing arterial enhancing tumors from normal liver which is primarily supplied by portal vein. Detection and diagnosis of malignant liver lesions require obtaining both arterial and portal phase images. In clinical practice, there is a sizable chance that the arterial phase is missed due to imperfect bolus timing. Additionally, each phase spans a long acquisition window, potentially resulting in a corrupted arterial phase with some portal venous enhancement. With high temporal frame rate, TRACER can provide the optimal arterial phases. Retrospectively selecting the optimal phases relieves the need for accurate bolus timing. An average 30% peak aorta to portal vein CNR increase indicates a better differentiation between arterial and portal enhancement. In addition, the high temporal frame rate allows interrogating sub-arterial phases and characterization of enhancement kinetics. Multiple breath holds are still needed with this technique to

acquire the later venous and delayed phases.

In TRACER, each frame is reconstructed using a single spiral leaf for each slice encoding, resulting in a high 3D temporal update. This can intrinsically capture small motions as was demonstrated in moving object and flow phantom experiments. When breathing is shallow, TRACER can, to a certain extent, still produce diagnostic images as shown in Figure 3.13c. Also detailed gastric and intestinal peristalsis was observed in many cases. This dynamic organ movement and deformation information has not been shown previously with 3D acquisitions.

Numerous methods have been proposed to accelerate DCE-MRI. Among recent approaches, k-t PCA (31,32) and partially separable function (PSF) (33) utilize the spatial-temporal correlation by incorporating basis functions from calibration data. PICCS (34), sparse-CAPR (35), HYPRIT(36,37), and RICS (38) are techniques based on compressed sensing (CS), where the temporal update compared to a reference or composite image is constrained (sparse) in an appropriately chosen domain. Other methods include the GraDes (39) method, which iteratively updates a sparse solution to achieve a high acceleration factor, and Nonlocal Means reconstruction (40), which constrains the spatial and temporal neighborhood similarities based on signal similarities.

Similar to these approaches, TRACER utilizes the temporal redundancy in DCE-MRI as a temporal constraint. The constraint between the solutions at consecutive time frames is implicit. This is due to the stopping criterion used, which stops the iterative solver when the norm of the update no longer decreases. In practice, for the heavily under-sampled spiral data used here, this criterion leads to very small number of

iterations, typically between 1 and 3. In our experience, this limits the amount of noise amplification and under-sampling artifact present in the final solution. Additionally, it leads to an implicit constraint on the amount of change permitted between successive time frames, and not just between intermediate solutions of the iterative LM solver. Adding an additional spatial or temporal constraint (such as an L1 norm in a certain transformed domain) in Eq [3.4] may be useful and could further improve the reconstruction accuracy at the potential expense of increased computation time. Compared to other approaches utilizing a reference or composite image, TRACER inherently updates this reference image together with the reconstruction. Additionally, and in contrast to some of the other methods, a given frame will only contain information from data sampled on or before that time point. This introduces a certain lag when the contrast change is very fast, as was shown in the contrast enhancement and impulse response simulations.

Dynamic imaging methods with view sharing commonly have a temporal footprint as long as the duration of a fully sampled data set like in sliding window. This footprint is reduced by the acceleration factor when parallel imaging is used. Here the impulse response function is used to calculate the temporal footprint. Although an impulse response analysis is only valid for a linear reconstruction, its results were found to be in good agreement with the numerical liver contrast enhancement phantom. It is speculated that the slowly changing coil sensitivities observed in both the phantom and in vivo reconstructions may make the input response analysis still a useful tool. Our results demonstrate TRACER has a variable temporal footprint depending on the k-space frequency. This temporal footprint is about 5 frames or

~1.1s (1/10 duration of the fully sampled dataset) or fewer for low spatial frequencies. For high spatial frequencies, the temporal footprint is around 12 frames or 2.7s. In comparison, multi-phase imaging has a constant temporal footprint of 48 frames or ~11s in a typical patient scan. As the k-space energy is mostly concentrated in low frequencies, it is expected that TRACER results are minimally affected by temporal blurring, as shown in the moving phantom position curve and flow phantom enhancement curve. This may also explain the enhancement delay seen in the numerical dynamic liver phantom experiment. Organs like aorta and portal vein have broader spatial frequency support. The corresponding increased temporal footprint combined with the fast temporal changes in these vessels, can therefore be expected to induce a delay between the reconstructed signal curve and the true signal curve that is larger than that of the liver. Indeed, the maximum aorta delay in the numerical liver phantom was two seconds corresponding to a duration of nine frames which is in the range of temporal footprints found using the impulse response analysis.

The reduced temporal footprint may also explain why the TRACER reconstruction produced higher aorta to portal vein CNR when compared to multi-phase technique and sliding window reconstruction which incorporate certain k-space information across a long acquisition window and are affected by temporal blurring due to the repeated sampling of the center of k-space in spiral sampling. The latter remained true to a lesser extent when a tornado like filter was used in the sliding window reconstruction. Accurate enhancement evolution would provide a way to differentiate benign and malignant tumors as well as new insights into contrast uptake pharmacokinetics in lesions. The patient case with arterially enhancing hepatocellular

carcinoma provides a vivid illustration of using high temporal frame rate images to probe arterial enhancement kinetics.

Spiral sampling has the advantage of sampling more k-space locations in one TR, making it well-suited for the TRACER method. On the other hand, it suffers from off-resonance and eddy current artifacts. However, for the typical axial orientation used in liver imaging combined with effective fat suppression and careful shimming, it was found that TRACER is only mildly affected by these artifacts. The highly under-sampled spiral trajectory caused inhomogeneous intensity changes from frame to frame. A temporal median filter greatly reduces this artifact while other filters like the mean filter or the more elaborate Kalman filter (41) are also possible. Additionally, information from a single spiral leaf may not be adequate when the dynamic change between two frames is large. This may result in inaccurate reconstruction and spiral under-sampling (ringing) artifacts. In the moving phantom experiments, when the temporal frame rate is high and the moving velocity is low, the shape and edge of the object can be well preserved. This observation in the phantom is consistent with the observation of adequate image quality in the TRACER reconstruction in the presence of shallow breathing. However, TRACER is currently not able to handle arbitrary respiratory motion, leading to blurring and ghosting artifacts.

A drawback of the proposed reconstruction method is the computational cost. This is in part due to the high number of reconstructed frames and the iterative nature of the solver. An oversampling factor of 3 was chosen to reduce errors when using in a convolution to approximate the gridding and regridding operations needed by the iterative solver (42). Compared to a more conventional oversampling factor of 2, this

increased computation time by ~8% while decreasing the peak RMSE by ~0.4% in the numerical simulation. The computation times for the whole 3D volume were ~2 hours using MATLAB (2009a, The MathWorks, Natick, MA) for a matrix of $256 \times 256 \times 40$ and 192 frames on a Dell PowerEdge R910 server (32 cores, 64GB memory). For a single slice, peak memory usage during initialization was 15MB and increased to 240MB during the subsequent nonlinear solver. Since the slice direction is fully encoded, an FFT can be performed at the beginning, such that each slice can be reconstructed independently. This means that the time-resolved reconstruction of several slices can be performed simultaneously on a modern multi-core desktop computer. The computation time could be potentially reduced with optimized C/C++ code and/or by using a GPU implementation (43). Furthermore, a linearized formulation of the encoding function with periodically updated coil sensitivities may help further decrease overall computation time, but its effect on reconstruction accuracy remains to be investigated.

3.12 Conclusion

By enforcing image fidelity to the sampled data of a time frame and imposing consistency with the previous image frame, Temporal Resolution Acceleration with Constrained Evolution Reconstruction (TRACER) reduces the temporal footprint of dynamic 3D contrast enhanced MRI of the liver while maintaining image quality. TRACER eliminates the need for bolus timing and allows the retrospective selection of optimal arterial phases. High temporal frame rate data sets allow the visualization of the continuous enhancement process.

CHAPTER 4

CEREBRAL PERFUSION MAPPING

Quantitative susceptibility mapping (QSM) has the potential to quantify contrast agent bio-distribution. The purpose of this study is to develop a QSM technique with sufficient temporal resolution for mapping first pass contrast agent concentration in brain perfusion quantification. Four-echo T_2* weighed 3D spoiled gradient echo phase images were acquired with a golden angle ordered spiral sequence during bolus injection of 0.1mmol/kg gadobutrol at 2ml/s. Time resolved field inhomogeneity maps were reconstructed using constrained reconstruction, TRACER. Contrast agent induced field map for each time point was deconvolved with a dipole inversion solver, MEDI, for concentration mapping. Cerebral blood volume and cerebral blood flow was computed from the arterial and tissue concentration curves. Initial in-vivo brain imaging data demonstrated the feasibility of mapping time resolved contrast agent quantification using the proposed method. Cerebral blood flow agrees with that obtained from arterial spin labeling technique. Dynamic quantitative susceptibility maps allowed brain perfusion mapping with cerebral blood flow value in good agreement with arterial spin labeling.

4.1 Introduction

Dynamic Susceptibility Contrast (DSC) MRI employs the magnetic field inhomogeneity change caused by paramagnetic contrast agent to assess cerebral perfusion (44-47). Time resolved contrast agent susceptibility effects during the first

passage are used to quantify arterial input function (AIF) and tissue contrast curves, which are then used to compute cerebral blood flow (CBF) and cerebral blood volume (CBV) according to indicator dilution theory.

Commonly the contrast concentration time curves are obtained by measuring ΔR_2^* of artery and tissue using a fast sequence like single shot EPI and then converting to contrast agent concentration according to the T_2 relaxivity of the contrast agent. Conversion from ΔR_2^* to concentration assumes a linear relationship and that the contrast agent T_1 effects are negligible. However, ΔR_2^* and contrast concentration actually have a quadratic relationship and the AIF obtained assuming a linear relationship may suffer substantial error (48-50). The coefficients of the quadratic function need to be calibrated for a specific contrast agent (like Gd-DTPA) and are hematocrit dependent (48). The tissue concentration is affected by the estimate of tissue relaxivity, which may also influence the perfusion map accuracy (50-52). For the unchanged T_1 assumption, usually a large TR is used, but it could still be a source of error (49). In tumor patients with leaky capillaries, the tumor will have substantial signal enhancement, which needs a sophisticated correction scheme for accurate perfusion quantification (53,54).

On the other hand, MRI phase data also provides important information regarding cerebral hemodynamics, especially when contrast agent produces a big local susceptibility change. The early work in cerebral perfusion (55) has attempted to use phase change to assess the relative contrast concentration and CBV. Recent studies investigated measuring AIF (56) with MR phase data as well. In certain vessel geometry condition, phase shifts is linear with contrast concentration and the derived

AIF from phase shows a substantial SNR improvement over that from ΔR_2^* method (57). Measuring Gd concentration from MRI phase data may be a simpler and more accurate approach to quantifying tissue perfusion. De Rochefort et al. (58) quantitated first pass aorta Gd concentration under piecewise constant assumption. Recently developed quantitative susceptibility mapping (QSM) (59) enables susceptibility measurement of more complicated anatomic structures and Gd contrast bio-distribution. Voxel wise susceptibility mapping with sufficient temporal resolution is potentially useful for cerebral perfusion mapping. Bonekamp et. al showed perfusion mapping results from susceptibility obtained from 2D EPI phase data (60). In this work, we proposed to use 3D multi-echo spiral sequence and constrained reconstruction to achieve sufficient spatial and temporal resolution needed for susceptibility mapping. Dynamic Gd concentration maps were reconstructed from the multi-echo phase images. CBF and CBV maps are obtained thereafter. In vivo study demonstrates the feasibility of the proposed method.

4.2 Data Acquisition

A spoiled 3D 4-echo stack-of-spiral sequence was developed for data acquisition (Figure 4.1). The spiral trajectory in k_x-k_y plane has a variable density such that the k-space center is three-fold oversampled whereas the edge is under-sampled by a factor of 0.8. Consecutive spirals are interleaved by the golden ratio angle of 220˚. For each angle, a full set of slice encodings is acquired (partially encoded) before moving to the next angle.

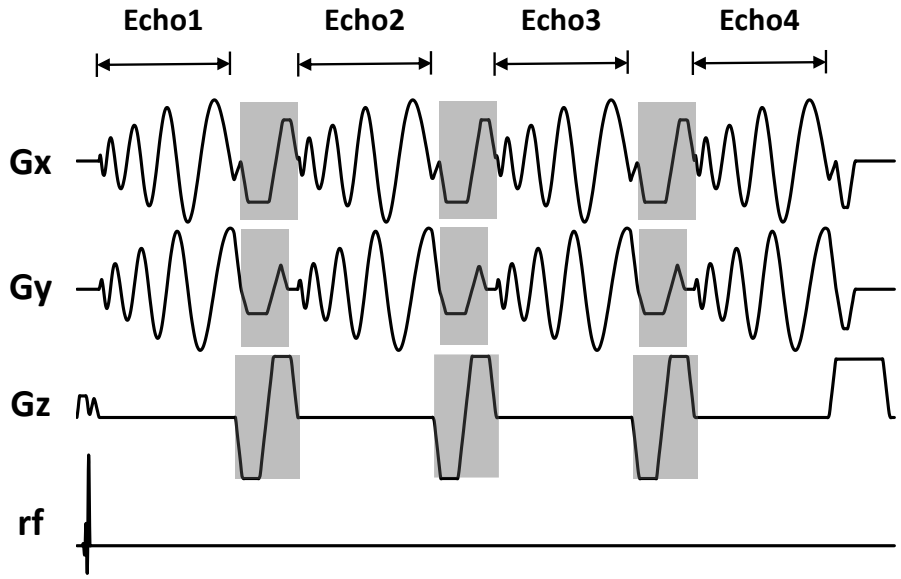

Figure 4.1 Multi-echo spiral pulse sequence
3D multi-echo stack of spirals gradient echo sequence. Bipolar flow compensation gradient (shaded in gray) is added in all directions to null the first order gradient moment.

After each spiral readout, the spiral is refocused to the k-space center and flow compensated before next echo. Flow compensation utilizes bipolar first moment nulling gradient added before each echo except for the first one. The width and amplitude of the flow compensation gradients are computed using the following constraints:

$$\int_{nTE}^{(n+1)TE} G_x(t)\,dt = 0, \int_{nTE}^{(n+1)TE} G_x(t)(\,t - nTE)dt = 0,$$
$$\int_{nTE}^{(n+1)TE} G_y(t)\,dt = 0, \int_{nTE}^{(n+1)TE} G_y(t)(\,t - nTE)dt = 0,$$
$$\int_{0}^{TE} G_z(t)\,dt = \frac{k_z}{\gamma}, \int_{0}^{nTE} G_z(t)\,(t - nTE)dt = 0 (n > 1).$$

The gradient moment nulling markedly reduces spiral ringing displacement artifacts of arteries and veins as shown in Figure 4.2.

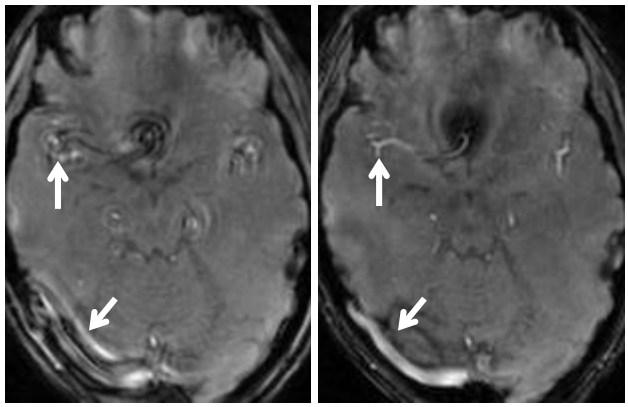

Figure 4.2 Effect of flow compensation gradient
Images reconstructed with and without flow compensation. Flow compensation markedly reduced the spiral artifact from artery and veins.

4.3 Dynamic Field Map Reconstruction

The golden angle view ordered spiral acquisition was reconstructed using Temporal Resolution Acceleration with Constrained Reconstruction (TRACER) (61). A 3D image of the first echo is reconstructed with a set of fully sampled spirals acquired at the beginning of the scan. Coil sensitivity maps were computed from the first echo and were used to compute the initial reference images of later echoes using conjugate gradient SENSE reconstruction. For TRACER reconstruction of dynamic image frames, instead of jointly solving both image content and coil sensitivity map, only image content was solved using the fixed coil sensitivity maps. In the previous study, each frame was updated by one spiral and was constrained by taking the previous frame as the initial guess for the solver. Here we improved TRACER by taking m consecutive spirals, from index N-m+1 to index N, when computing frame N. As more k-space is covered when solving one frame, the under-sampling artifacts are greatly

reduced compared with a single spiral update while the update information from acquired data is still from spiral N. On the other hand, m should be small to eliminate temporal blurring. As consecutively acquired spirals were interleaved with golden angle view order, m = 3, 5, 8, 13, 21 will give a uniform coverage of the k-space while minimizing under-sampling artifacts.

After reconstruction of multi-echo complex 4D images, the phase images of the first frame (pre Gd administration) was subtracted from all later frames. Then for each frame, this difference phase data was linearly fitted through all echoes to produce the magnetic field map corresponding to the evolving Gd contrast agent biodistribution.

4.4 Perfusion Mapping

The susceptibility map of contrast agent for each frame was computed from the field map using morphology enabled dipole inversion (MEDI) solver. The contrast concentration maps were then computed from the susceptibility map, using the molar susceptibility of Gd^{3+} (326ppm L/mol) (62) . A susceptibility offset was applied to each frame by setting susceptibility in ventricles to zero. An arterial input function chosen from the middle cerebral artery was used for voxel-by-voxel de-convolution of the tissue contrast curve. The tissue concentration curve C(t) is the convolution of AIF and residual function R(t) scaled by the CBF:

$$C_t(t) = \frac{\rho}{k_H} CBF \int_0^t AIF(\tau) R(t-\tau)\, d\tau = CBF \cdot R(t) \otimes AIF(t) \qquad [4.1]$$

The correction factor $k_H = (1 - H_{artery})/(1 - H_{capillary})$, where $H_{artery} = 0.45$

and $H_{capillary} = 0.25$ accounts for the hematocrit difference between large vessels and capillaries. The density of brain tissue is set to 1.04 g/mL (46). The residual function R(t) is computed using truncated SVD de-convolution (63) where the truncation threshold is taken to be 0.2 and CBF is taken to be the maximum value of R(*t*). Cerebral blood volume was determined by integrating the area under the concentration time curve and normalized to the area of arterial input function:

$$CBV = \frac{k_H}{\rho} \frac{\int_0^{T_{max}} C_t(\tau)\, d\tau}{\int_0^{T_{max}} AIF(\tau)\, d\tau} \quad [4.2]$$

In the implementation, we choose the time range from the start of the enhancement to when the signal drops to noise level.

4.5 Flow Phantom Study

4.5.1 Experiment setup

A flow phantom experiment was carried out to validate the measured contrast concentration using dynamic susceptibility mapping. A U-shaped vinyl tube was connected to a pump and fixed inside a plastic box filled with water. A three-way valve on the inlet was connected to the power injector to allow contrast injection. The pump circulates water from a reservoir with contrast concentration of 0.5 mM through the tube at a flow rate of 5.5 ml/s. The plastic box in the imaging FOV contains water with 1mM contrast agent to enhance background signal. Gadovist diluted to 100mM was filled in the power injector. For the dynamic scan described below, 3mL of the

solution followed by 10mL saline flush was injected at 1mL/s. The phantom in the FOV is shown in Figure 4.3

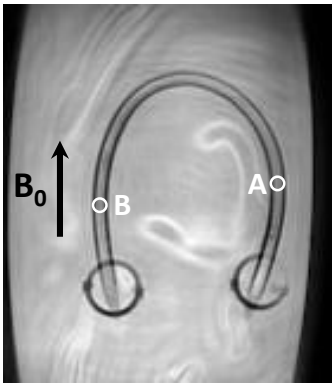

Figure 4.3 Flow phantom setup
A magnitude image showing the flow phantom setup. ROI A on the inlet and B on the outlet were used to plot concentration time curves.

4.5.2 Scan protocol

The proposed multi-echo spiral sequence was used to imaging the contrast dynamics. A coronal slab was prescribed to cover the whole tube. Scan parameters for the scan were: dual-echo TE1/TE2/TR = 1.0/7.75/15.6 ms, FA=30 ˚, FOV=24cm, slice thickness = 3mm, matrix size = 160×160×14, BW = ±125kHz. The contrast injection started 5 seconds after the scan initiation. Total scan time was 48 seconds. In addition, a 2D spiral sequence was used as a reference scan of the contrast dynamics. One coronal slice was prescribed to covers the whole tube in the imaging FOV. Scan parameters were: TE/TR = 1.7/10 ms, FA = 40˚, FOV = 24cm, slice thickness = 12mm, matrix size = 160×160, BW = ±125kHz. Scan time for one slice took 242ms.

4.5.3 Concentration time curve

Two ROIs were drawn from the straight part of the tube that was parallel to B_0 field.

The reference contrast concentration within the ROI was obtained from the phase data of 2D scan according to equation:

$$\theta(t) = \theta(0) + \frac{1}{3}\omega_0 \chi_m TE[Gd]_t \quad [4.3]$$

Dynamic susceptibility maps were computed from the data acquired using multi-echo spiral sequence and reconstructed with TRACER. Then the concentration time curves were compared with that from 2D reference scan.

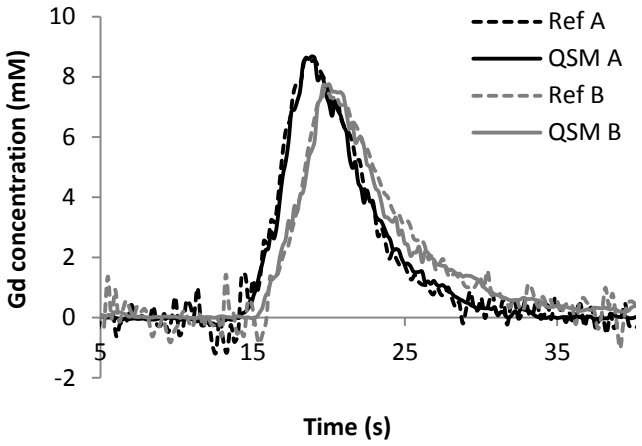

Figure 4.4 Concentration time curves
Contrast concentration time curves computed from dynamic susceptibility mapping agree well with that obtained from phase of the referencd 2D scan.

Figure 4.4 shows the corresponding time curves starting from contrast injection. The concentration measured from dynamic susceptibility mapping agrees well with that obtained from the 2D reference scan at both ROIs. A dispersion and reduced amplitude of the enhancement curves was found on the outlet (B) compared with inlet (A). The integral of the concentration time curves from dynamic susceptibility mapping is 57.8 $\text{mM} \cdot s$ and 53.9 $\text{mM} \cdot s$ in ROI A and B, which corresponds to

total injection amount 318 mmol and 296mmol (flow rate 5.5 ml/s). This is in accordance with the 300mM total injection amount with the discrepancy due to injection variance and reconstruction noise.

4.6 In Vivo Study

4.6.1 Scan protocol

This study was institutional review board approved and HIPPA-compliant. Three healthy volunteers (2 male, 1 female), brain imaging was performed using an 8-channel head coil on a 3T scanner (Signal HDxt; GE Medical Systems) after obtaining informed consent. For spiral axial DSC scan, typical scan parameters were: 4 echoes, $TR/TE_{first}/TE_{last}$ = 34.3/0.7/25.3 ms, bandwidth = ± 125 kHz, flip angle = 15˚, FOV = 22cm, matrix size = 200×200×22, voxel size = 1.1×1.1×3 mm^3. The scan slab was prescribed to cover most of the cerebrum including the middle cerebral artery for AIF measurement. Total scan time was about two and a half minutes. Twenty seconds after scan initiation, 0.1mmol/kg gadobutrol (Gd-BT-DO3A, Gadovist) was injected at 3ml/s followed by 30ml saline flush at 3ml/s. The injection delay is necessary for reconstructing a pre-contrast reference image.

4.6.2 Perfusion imaging

Dynamic contrast concentration maps were reconstructed at a temporal frame rate of 0.7 seconds. A Gaussian smoothing with kernel width of three pixels is applied on the perfusion maps. Figure 4.5 shows the time resolved phase curves of one voxel in gray matter. The phase change follows the contrast agent arrival and is proportional to the

echo time. With linearly spaced echo time, the phase different between each echo is also linearly spaced. At peak enhancement, substantial phase change in the gray matter could be observed.

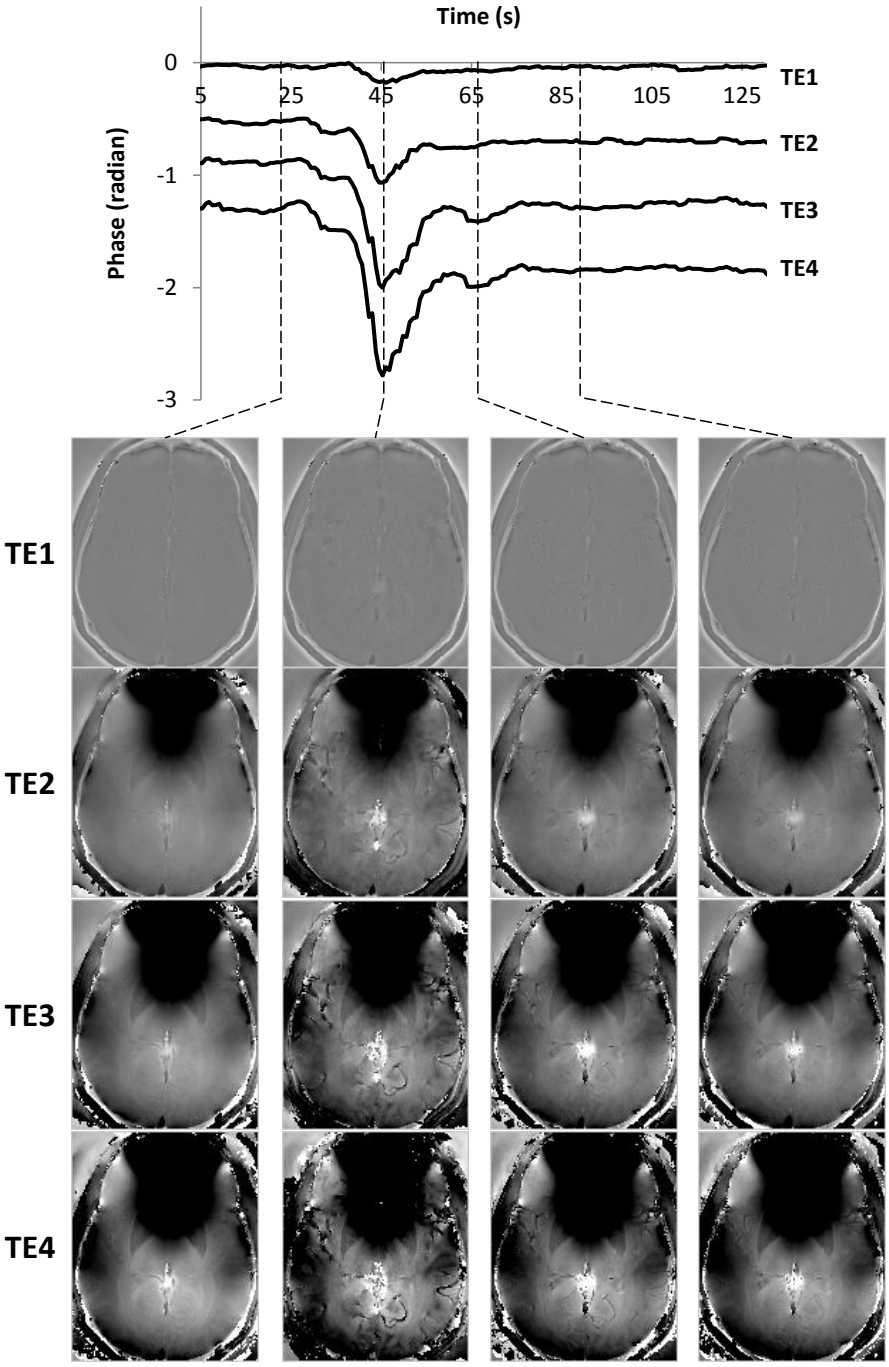

Figure 4.5 Time resolved phase curves

Figure 4.6a shows the measured AIF in middle cerebral artery. The peak bolus concentration reaches to 6mM. Shown in Figure 4.6b are the contrast concentration maps at five time points that are marked on the AIF curve. They correspond to pre-contrast, early arterial phase, peak arterial phase, late arterial phase, and equilibrium phase. The contrast arrival and wash out stages in brain vessels and tissues could be observed.

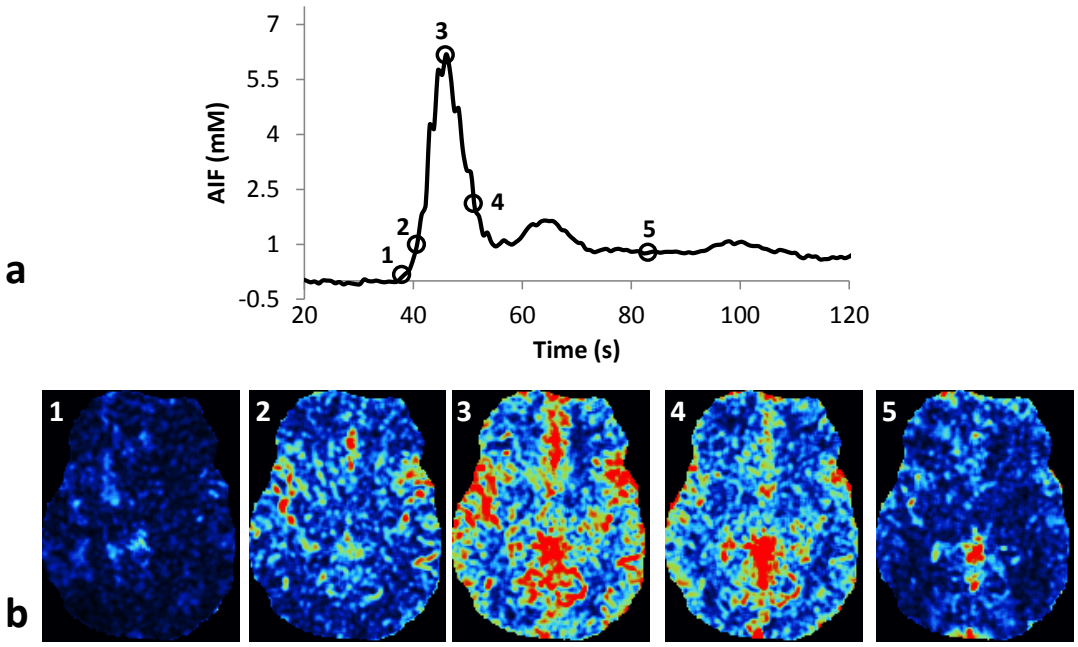

Figure 4.6 Contrast concentration time curves
(a) AIF measured from middle cerebral artery that used for perfusion map quantification. **(b)** Measured contrast agent concentration (log plot) at five time points during the contrast passage. Then enhancement pattern in different regions could be observed.

Figure 4.7 shows the measured CBF and CBV maps in five slices that are in the center of the brain. Grey white matter contrast could be observed. The mean CBF value is around 65ml/100g/min for gray matter and 25ml/100g/min for white matter. The mean CBV value is around 5.6mL/100g for gray matter and 2.3 mL/100g for

white matter. These values are within the physiological ranges from previous studies (46). Some under-estimation of the perfusion value is found in the boundary of frontal lobe. This is due to the spiral artifact from high inhomogeneity field in the frontal lobe and error from susceptibility mapping.

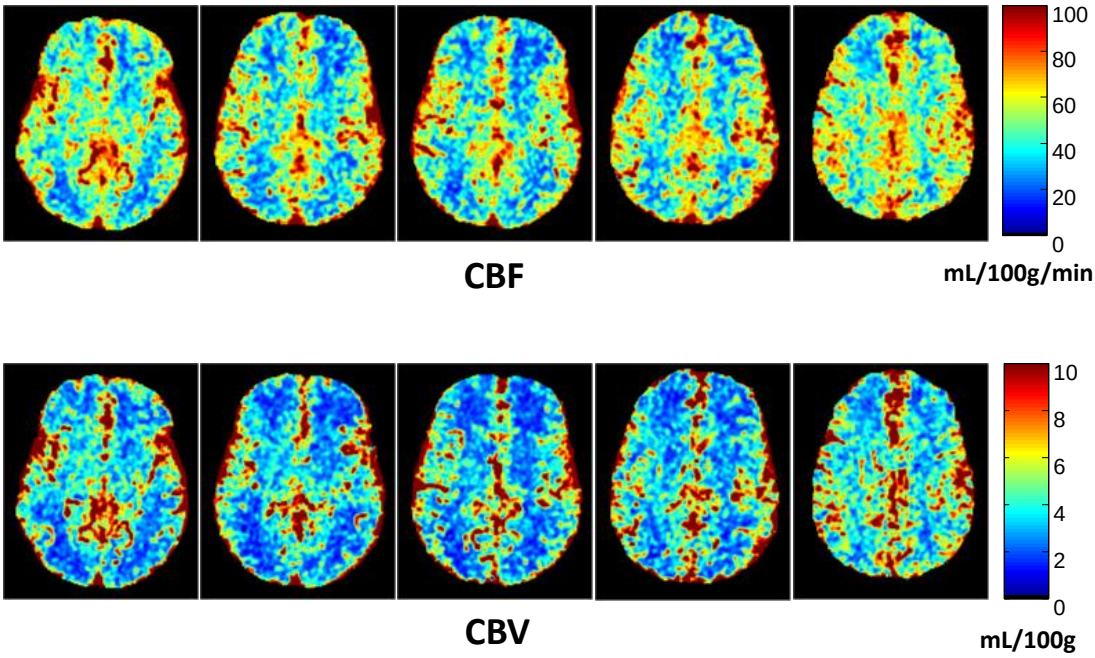

Figure 4.7 CBF and CBV maps
CBF and CBV maps of five slices in the middle of the brain.

4.6.3 Comparison with ASL

An ASL scan was performed before contrast injection followed by a dynamic DSC scan. A commercial pulsed continuous axial ASL was performed. The sequence employs multi-arm spiral imaging with eight arms, each with 512 readout points (bandwidth = ± 62.5 kHz), giving an in plane resolution of 3.2mm. Other scan parameters were: TR/TE = 4.9s/11ms, FOV = 22cm, slice thickness = 2mm, number of slices = 60. Total scan time was 5 minutes. Post processing was performed on the

scanner console to obtain the CBF map.

The magnitude image from the first echo of DSC scan was co-registered with the proton density images acquired in ASL with FSL toolbox (64). The transformation matrix is used to register ASL CBF map. ROIs in gray and white matter were identified in the ASL CBF maps. Within each ROI, mean and standard deviation of CBF value from both ASL and dynamic QSM were measured and compared.

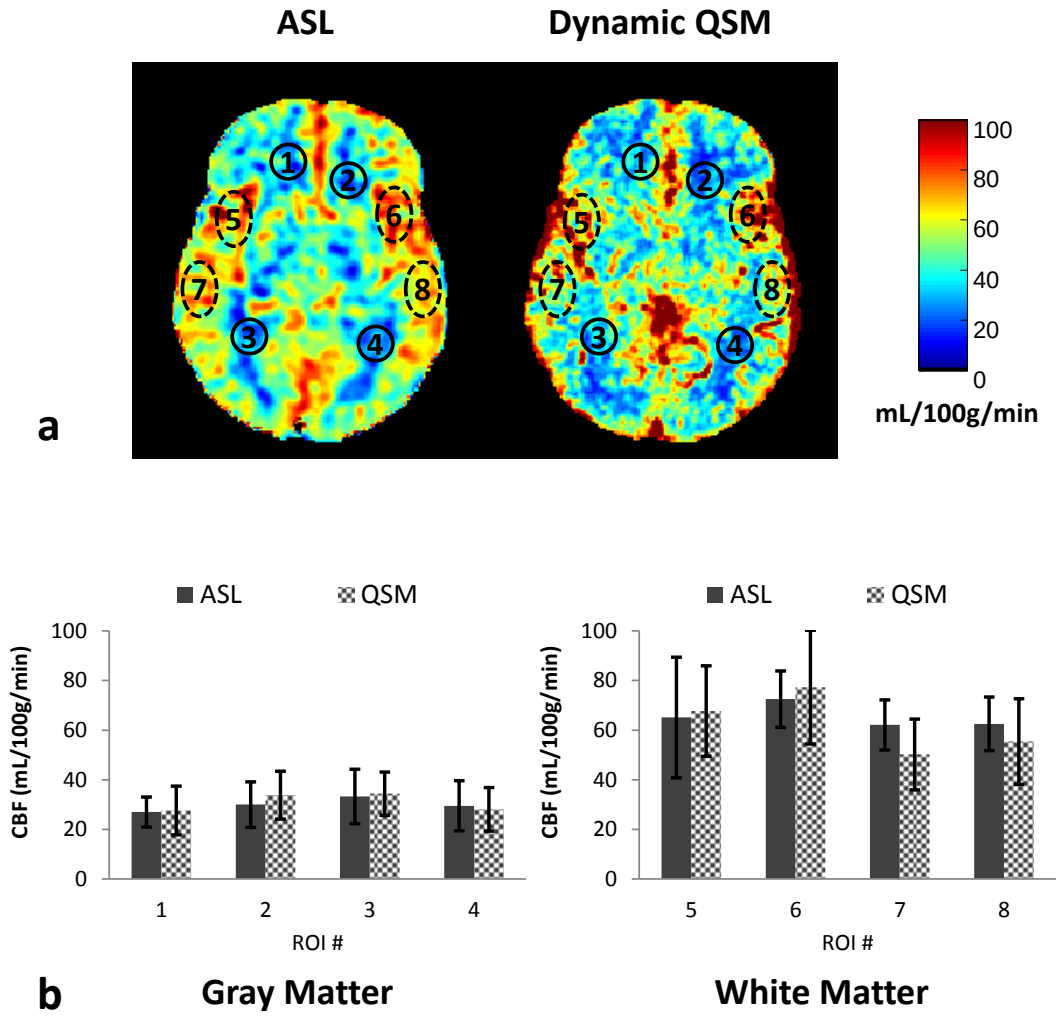

Figure 4.8 Comparison of CBF from ASL and dynamic QSM
The value from dynamic QSM is close to that from ASL. The CBF obtained from QSM in general has larger standard deviation. The QSM derived CBF value has large error in the boundary due to background removal procedures in QSM.

Figure 4.8 shows the comparison of CBF maps obtained from ASL and dynamic QSM. Eight ROIs, 4 in gray matter and 4 in white matter are labeled. Mean and standard deviation of CBF in gray and white matter are plotted in Figure 4.8b. In general, the mean CBF values from dynamic QSM agree with CBF from ASL in each ROI, while the standard deviation in QSM CBF is higher.

4.7 Discussion

Quantitative susceptibility mapping (QSM) is an emerging technique that provides pathophysiology information complementary to traditional T_1, T_2 and T_2* weighed imaging (65-70). QSM has been successful in static tissue imaging (59,71), with a scan time usually in minutes. In this study, for the first time, we demonstrate dynamic quantitative susceptibility mapping by using spiral acquisition and constrained reconstruction. The reconstructed dynamic susceptibility maps, with sub-second temporal frame rate and relative high spatial resolution, is used for quantitative cerebral perfusion imaging.

Imaging first pass contrast agent administration requires high temporal resolution. Different acquisition and reconstruction techniques have been proposed for first pass perfusion MRI and DSC MRI (31,61,72-74). In DSC MRI, ΔR_2* from magnitude image is used for contrast agent quantification. Directly quantifying susceptibility would open a new path for DSC MRI. However, this is hampered by the lengthy scan time of susceptibility mapping. Non-Cartesian sampling has been proposed to accelerate QSM (75). To achieve the desired temporal resolution for capturing contrast dynamics, we extended the TRACER technique to multi-echo acquisition in

susceptibility mapping. As Figure 4.2 demonstrates, flow compensation is necessary to eliminate flow induced displacement artifact. This is especially important for DSC MRI, where the arteries are used to obtain AIF. In order to mitigate decreased temporal resolution in multi-echo scan, a sliding-window TRACER is employed here. This scheme can greatly reduce the spiral under-sampling artifacts when there is substantial temporal change between adjacent spirals. With a small sliding window, the temporal tracking ability of TRACER is only slightly affected. The reduced noise in the enhancement curve is crucial for AIF de-convolution and improves the SNR of final perfusion maps.

The dipole inversion solver for susceptibility mapping is also adapted to dynamic imaging. For gadolinium quantification, only contrast agent induced magnetic field is of the interest. Subtraction of baseline field map can eliminate most of the unwanted field contribution from background susceptibility sources. This subtraction also alleviates the phase unwrapping problem when high susceptibility source like gadolinium contrast agent is present. Background field removal is performed on this difference field to get rid of any residual field from susceptibility sources outside the imaging FOV or from B_0 field variation.

The major advantage of the proposed method is its direct measurement of contrast agent concentration from susceptibility. R_2* based contrast quantification is subject to error induced from the nonlinear relationship between ΔR_2* and AIF. Linear model can either overestimate or underestimate the CBF value. Nonlinear is more preferable but subject to choice of the parameters (50). Tissue relaxivity is also known to vary according to the contrast agent bio-distribution (76) and the value measured from

different method has a big discrepancy. Furthermore, T_1 effect is not negligible when the blood brain barrier is intact. These conditions all contribute to the uncertainty of the estimated concentration.

Susceptibility is proportional to contrast concentration with a scaling factor of Gd^{3+} molar susceptibility. The computed concentration does not rely on assumptions of vessel geometry or physiological parameter (like Hematocrit). The ideal of AIF measurement from phase in a straight artery is extended to all tissue with the help of magnetic dipole inversion. In the flow phantom experiment, the concentration obtained from susceptibility agrees well with that from phase as shown in Figure 4.4. This experiment also demonstrates the temporal tracking ability of TRACER reconstruction. The concentration curves closely follow the concentration curves from 2D scan that has a temporal resolution of 242ms.

Our initial in vivo results demonstrate the feasibility of using susceptibility for Gd quantification in perfusion mapping. The CBF and CBF maps show good gray and white matter contrast. The perfusion values fall in the physiological range. The CBF measurement generally agrees with the ASL measurement. Some discrepancy is seen too. In dynamic QSM method, the straight sinus and superior sagittal sinus shows large CBF value. In comparison, ASL does not capture the vein CBF due to its tagging mechanism. Another discrepancy is primarily in the frontal lobe and the posterior gray matter region. Dynamic QSM method underestimates CBF values in these regions. This is primarily due to imperfect background removal in QSM, which tends to result in errors in the boundaries of the image. This needs further investigation to improve.

A few areas could be further explored to improve the technique. Multi-slice 2D

acquisition with large TR is promised to provide improved SNR compared to the current 3D acquisition. How 2D acquisition could be integrated with TRACER reconstruction and affect dipole inversion needs to be evaluated. Currently, data processing takes tens of minutes on a multi-core server. To make the technique clinic applicable, magnitude of acceleration is possible by optimizing and paralleling the solver.

4.8 Conclusion

Contrast agent concentration time curves are quantitated using multi-echo spiral acquisition, constrained image reconstruction, and quantitative susceptibility mapping. The concentration maps are used to extract arterial input function and tissue concentration curves for quantitative cerebral perfusion. Phantom validation and in vivo comparison demonstrate the feasibility of perfusion mapping using dynamic QSM.

CHAPTER 5

VENOUS OXYGENATION QUANTIFICATION

Venous blood oxygen saturation is an indicator of brain oxygen consumption and can be measured directly from quantitative susceptibility mapping (QSM) by deconvolving the MR phase signal. However, accurate estimation of the susceptibility of blood may be affected by flow induced phase in the presence of imaging gradient and the inhomogeneous susceptibility field gradient. Flow compensation is proposed for QSM by using a fully flow compensated multi-echo GRE sequence for data acquisition and a quadratic fit for the flow phase associated with inhomogeneity field gradient. This flow compensated QSM is validated in phantom experiments. Preliminary results from in vivo human imaging demonstrate improvements in the quantitative susceptibility map and in the estimated venous oxygen saturation values.

5.1 Introduction

Magnetic susceptibility is a physical tissue property that varies in healthy tissue and may also change with pathologic conditions. Susceptibility provides information complementary to traditional T1, T2 and $T2^*$ weighted images. Quantitative Susceptibility Mapping (QSM) computes the magnetic susceptibility distribution based on the magnetic field inhomogeneity generated by magnetic sources (68,77-83). QSM has been shown to provide useful anatomical and clinical information for brain iron quantification (66,84), subthalamic nucleus visualization (85) , and cerebral microbleeds characterization (67). Since magnetic susceptibility is linear in the

deoxyhemoglobin concentration, it also allows venous oxygen saturation quantification (65,86-88). However, blood flow induced artifacts hamper accurate measurement of blood susceptibility. QSM employs a dipole deconvolution of the magnetic field measured by MRI to obtain the susceptibility distribution. Typically, to compute the field map, multi-echo gradient echo phase images are acquired and the field map is estimated by performing a linear fit of the phase to the echo time (TE). However, in the presence of flow, usually between 10~20 cm/s in the veins (89,90) and local spatial field inhomogeneity, this linear assumption does not hold. Travelling spins accumulate additional phase that may cause vessel misalignment and erroneous magnetic field estimation. Without correction, the computed field map in vessels may not be accurate and may lead to unreliable blood susceptibility and oxygen saturation values.

In this chapter, the theoretic relationship between the phase, both in image space and k-space, of flowing spins and TE is derived. A data acquisition and a reconstruction approach is proposed to improve the vessel susceptibility quantification. In the data acquisition, gradient moment nulling is added to the readout, phase and slice encoding directions for all echoes. In the data reconstruction, a quadratic fit is used for regions exhibiting flow while a linear fit is used for regions with static spins. Phantom experiments are performed to validate the theory and demonstrate the improved field map estimation. Improved image quality is demonstrated in human brain images. More consistent venous oxygen saturation measurement is achieved with the improved susceptibility value.

5.2 Theory

5.2.1 Signal modeling

The k-space MRI signal s at time t acquired for a static spin isochromat could be written as:

$$s(t) = \int \rho(\mathbf{r}) e^{-i(\psi+\gamma\delta B(\mathbf{r})t+\gamma\int_0^t \mathbf{G}(\tau)\,d\tau\cdot\mathbf{r})}\,d\mathbf{r} \qquad [5.1]$$

where $\rho(\mathbf{r})$ is the density of the spin isochromats at position $\mathbf{r}$, ψ is an initial phase after the radio frequency (RF) pulse; γ is the gyromagnetic ratio; $\delta B(\mathbf{r})$ is the field inhomogeneity; $\mathbf{G}(\tau)$ is the imaging field gradient at time $0 < \tau < t$. When flow exists, the position vector $\mathbf{r}$ of the excited spins depends on t and should be noted as $\mathbf{r}(t)$. The signal equation becomes:

$$\begin{aligned} s(t) &= \int \rho(\mathbf{r}(0)) e^{-i(\psi+\gamma\int_0^t \delta B(\mathbf{r}(\tau))d\tau)}\, e^{-i\gamma\int_0^t \mathbf{G}(\tau)\cdot\mathbf{r}(\tau)d\tau} d\mathbf{r} \\ &= \int \rho(\mathbf{r}(0)) e^{-i\phi_1} e^{-i\phi_2}\,d\mathbf{r} \end{aligned} \qquad [5.2]$$

The first phase term $\phi_1 = \psi + \gamma\int_0^t \delta B(\mathbf{r}(\tau))d\tau$ represents the phase that a spin isochromat accumulates along the traveling path in image space. The second phase term $\phi_2 = \gamma\int_0^t \mathbf{G}(\tau)\cdot\mathbf{r}(\tau)d\tau$ contains the usual k-space encoding. Let us assume that for a given spatial location $\mathbf{r}$, the velocity $\mathbf{v}(\mathbf{r}(\tau))$ is constant in a local region around $\mathbf{r}$ and is constant in time, up to at least the largest TE. Then $\mathbf{r}(\tau) = \mathbf{r}_0 + \mathbf{v}(\mathbf{r}_0)\tau = \mathbf{r}_{TE} + \mathbf{v}(\mathbf{r}_0)(\tau - TE)$, where $\mathbf{r}_0 = \mathbf{r}(0)$ and $\mathbf{r}_{TE} = \mathbf{r}(TE)$. Let us further

assume $\delta B(\mathbf{r})$ is linearly varying in a small local region around the path of the moving spin, i.e., $\delta B(\mathbf{r} + d\mathbf{r}) = \delta B(\mathbf{r}) + \nabla \delta B(\mathbf{r}) \cdot d\mathbf{r}$. After substituting $\mathbf{r}(\tau)$ into Eq [5.2], ϕ_1 and ϕ_2 becomes:

$$\begin{aligned} \Phi_1 &= \psi + \gamma \int_0^{TE} \delta B\big(\mathbf{r}_{TE} + \mathbf{v}(\mathbf{r}_0)(\tau - TE)\big) d\tau \\ &= \psi + \gamma \int_0^{TE} \big(\delta B(\mathbf{r}_{TE}) + (\tau - TE)\mathbf{v}(\mathbf{r}_0) \cdot \nabla \delta B(\mathbf{r}_{TE})\big) d\tau \\ &= \psi + \gamma \delta B(\mathbf{r}_{TE}) TE - \frac{1}{2}\gamma \mathbf{v}(\mathbf{r}_0) \cdot \nabla \delta B(\mathbf{r}_{TE}) TE^2 \end{aligned} \quad [5.3]$$

$$\begin{aligned} \Phi_2 &= \gamma \int_0^{TE} \mathbf{G}(\tau) \cdot \big(\mathbf{r}_{TE} + \mathbf{v}(\mathbf{r}_0)(\tau - TE)\big) d\tau \\ &= \gamma \mathbf{r}_{TE} \cdot \int_0^{TE} \mathbf{G}(\tau) d\tau + \gamma \mathbf{v}(\mathbf{r}_0) \cdot \int_0^{TE} \mathbf{G}(\tau)(\tau - TE) d\tau \\ &= 2\pi \mathbf{r}_{TE} \cdot \mathbf{k}(TE) + \gamma \mathbf{v}(\mathbf{r}_0) \cdot \mathbf{M}(TE) \end{aligned} \quad [5.4]$$

where $\mathbf{k}(TE)$ is the k-space position and $\mathbf{M}(TE)$ is the first moment of $\mathbf{G}(\tau)$ at time TE. In Eq [5.3], the phase Φ_1 is a quadratic function of TE. The linear coefficient reflects the local field inhomogeneity, causing shift along the readout direction; The quadratic coefficient is proportional to the flow velocity and the gradient of the field inhomogeneity, referred to here as the inhomogeneity field gradient. This quadratic phase term is independent of phase encoding and its TE squared dependence may cause blurring along the readout direction. In Eq [5.4], the second term can be compensated using gradient moment nulling for a given imaging gradient as in standard MRA (62,91-96).

5.2.2 Gradient moment nulling

A diagram of the 3D multi-echo GRE sequence with first moment nulling gradient is illustrated in Figure 5.1.

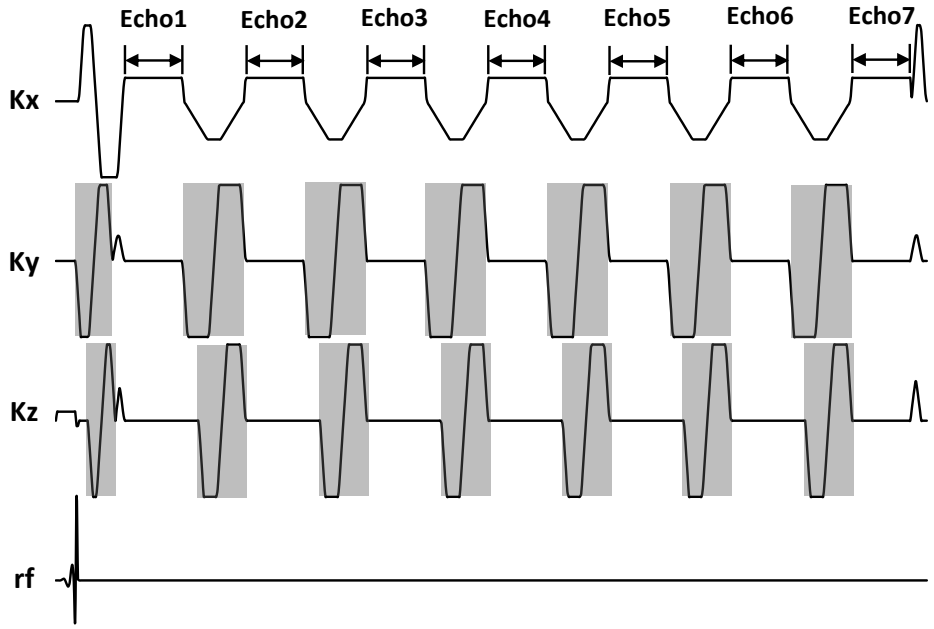

Figure 5.1 Flow compensated multi-echo GRE sequence
Bipolar flow compensation gradients (shaded in gray) are added before each echo in the phase and slice encoding directions to null the first order gradient moment.

The fully flow compensation can be realized using the following gradient constraints ($t = 0$ at the peak of the RF, $t = nTE$ at the nth echo center):

$$\int_0^{TE} G_x(t)\,dt = 0, \int_0^{TE} G_x(t)\,tdt = 0, \int_{nTE}^{(n+1)TE} G_x(t)\,dt = 0, \int_{nTE}^{(n+1)TE} G_x(t)\,tdt = 0,$$

$$\int_0^{TE} G_y(t)\,dt = \frac{k_y}{\gamma}, \int_{(n-1)TE}^{nTE} G_y(t)\,dt = 0(n > 1), \int_0^{nTE} G_y(t)(t - nTE)dt = 0,$$

$$\int_0^{TE} G_z(t)dt = \frac{k_z}{\gamma}, \int_{(n-1)TE}^{nTE} G_z(t)dt = 0(n > 1), \int_0^{nTE} G_z(t)(t - nTE)dt = 0.$$

In the readout direction, each echo is refocused, and flow compensation is naturally

achieved at the center of each echo after inserting an appropriate moment nulling gradient before the first echo. In the phase encoding directions (k_y and k_z), the first moment of phase encoding gradient increases from one echo to the next by the amount of the phase encoding gradient area (k_y or k_z) times the echo spacing, so the same gradient moment nulling can be used for all later echoes except the first one.

Gradient moment nulling removes the extra phase $\gamma \mathbf{v}(\mathbf{r}_0) \cdot \mathbf{M}(\mathrm{TE})$ for each TE in a multi-echo sequence. Note that gradient moment nulling only corrects for the ghosting artifacts in the magnitude images. The reconstructed image still has an extra phase component $\frac{1}{2}\gamma \mathbf{v}(\mathbf{r}_0) \cdot \boldsymbol{\nabla}\delta\mathrm{B}(\mathbf{r}_{\mathrm{TE}})\mathrm{TE}^2$ due to the varying local field in which the moving spins travel.

5.2.3 High order fit of the multi-echo phase

In image space, and under the assumptions stated above, phase is a linear or quadratic function of TE depending on whether or not the spin is traveling. A linear fit is applicable in static regions but a quadratic fit may be necessary in voxels experiencing flow. In this study, both a linear fit $\phi_1 = \psi + L\ \mathrm{TE}$ and a quadratic fit $\phi_1 = \psi^* + L^*\ \mathrm{TE} + Q^*\ \mathrm{TE}^2$ were performed for each voxel. However, there is much greater noise amplification in the quadratic fit than the linear fit due to the increased unknowns. In order to improve the SNR, a mixing of linear and quadratic fits, referred to as adaptive-quadratic fit, was developed to ensure that the quadratic fit was only used in regions with flow. As indicated in Eq [5.3], the field inhomogeneity $\gamma\delta\mathrm{B}$ is the coefficient of the linear term L or L^*. In flow regions, L and L^* are distinctly different and Q^* is nonzero. Based on this, the field inhomogeneity was computed as

the combination of the two fit results: $\gamma\delta\mathrm{B} = (1-\mathrm{w})L + wL^*$, using the weighting $\mathrm{w} = 1 - \mathrm{e}^{-\alpha|(L-L^*)Q^*|\mathrm{dTE}^3}$, with empirical $\alpha = 10^{-4}$. The resulting field inhomogeneity map served as the input for nonlinear morphology enabled dipole inversion (83), a dipole deconvolution solver, to compute the susceptibility map.

5.3 Flow Phantom Experiment

5.3.1 Phantom setup

A U-shaped vinyl tube connected to a pump was fixed inside a plastic box, which was filled with tap water and put inside the scanner. The pump generated a constant flow with known velocity. Both experiments were performed on a 3T scanner (GE Signa HDxt).

5.3.2 Flow displacement

In the first experiment, two scans were performed: the first scan with an unmodified product sequence where flow compensation was only applied to the readout direction (10 echoes, TR/TE_{first}/TE_{last} =36.0/3.1/32.2ms, FA=20˚, coronal FOV=25cm, voxel size = 1×1×1 mm^3, BW=±62.5kHz) and the second scan with the proposed sequence with flow compensation applied in all three directions for all echoes (6 echoes, TR/TE_{first}/TE_{last} =35.0/3.1/30.3ms, FA=20˚, coronal FOV= 25cm, voxel size = 1×1×1 mm^3). The flow velocity was set to 60cm/s to match the magnitude of quadratic term component $\mathbf{v}\cdot\boldsymbol{\nabla}\delta\mathrm{B}$ to that observed in preliminary in vivo studies.

Figure 5.2 shows the magnitude images acquired without (Figure 5.2a) and with (Figure 5.2b) phase encoding flow compensation (i.e. k_y and k_z). In Figure 5.2a,

without flow compensation, displacement artifacts appear in the phase encoding direction, which increase with TE. In Figure 5.2b, it can be seen that flow compensation markedly reduces these artifacts.

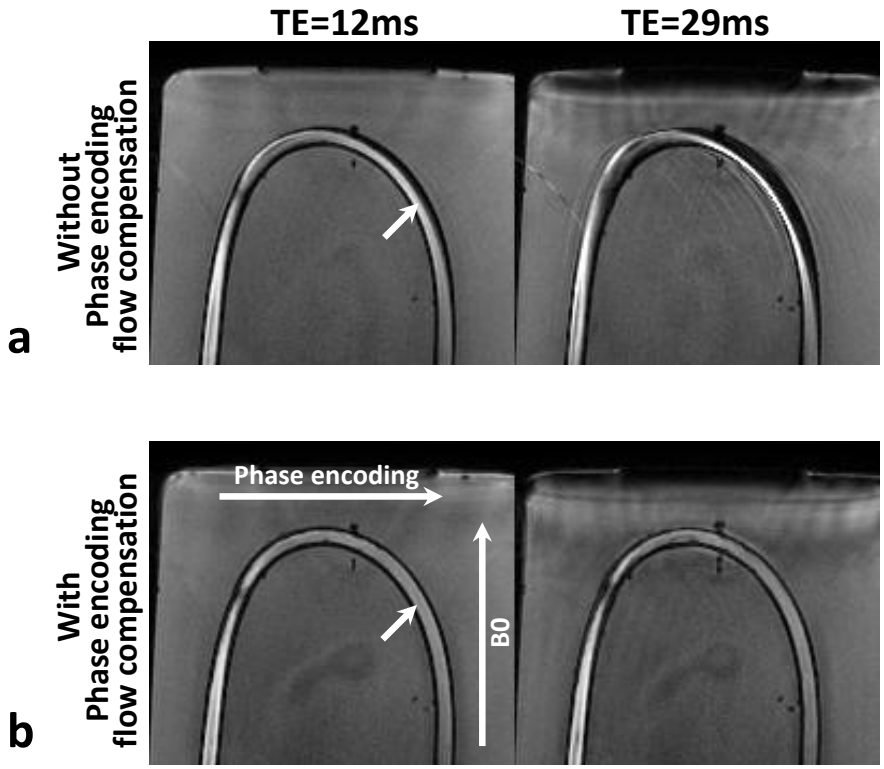

Figure 5.2 Magnitude from scans with/without flow compensation
Shown are images at TE=12ms and 29ms. Without flow compensation, water flow displacement artifacts appear in the phase encoding direction, which increase with TE. With flow compensation, the artifacts are substantially reduced.

Figure 5.3 shows the phase plot of one voxel indicated by the arrow in Figure 5.2. In Figure 5.3a, due to displacement of the flow, the phase from non-compensated scan exhibits a nonlinear relationship with TE. In Figure 5.3b, although with flow compensation, the phase exhibits an approximately quadratic, instead of linear, relationship as a function of TE. The absolute value of the linear coefficient –

presumed to be proportional to the field inhomogeneity – is 12 times larger for the linear fit (-0.0695) as compared to the quadratic fit (-0.0057).

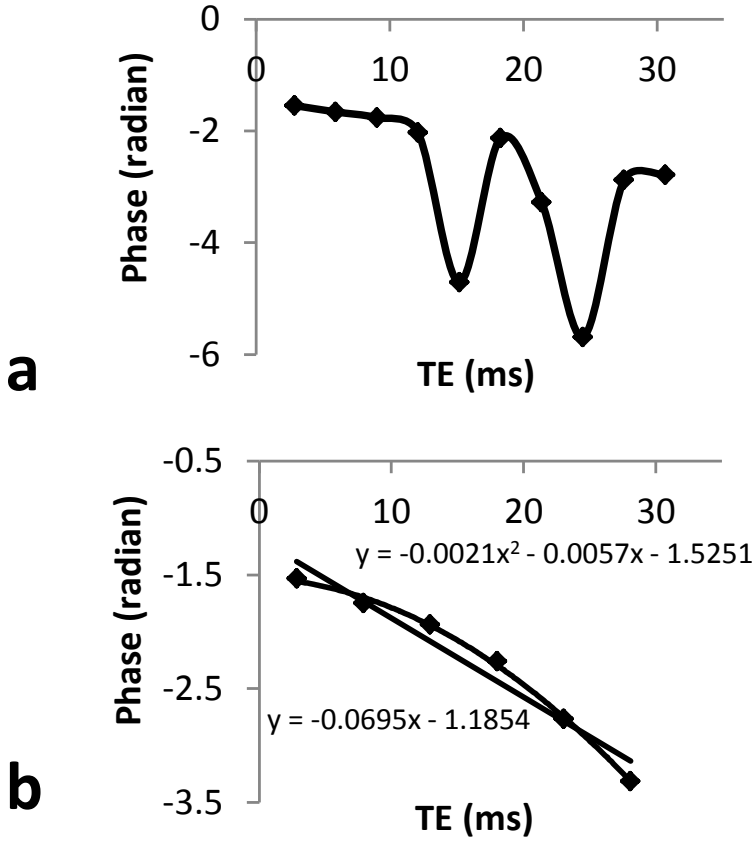

Figure 5.3 Phase plot from scans with/without flow compensation
The phase measured in the later echoes no longer reflects the phase of the original voxel due to its flow-induced displacement. The phase of the same voxel exhibits an approximately quadratic relationship because of the susceptibility induced field gradient. The absolute value of the linear coefficient of the linear fit (-0.0695) is 12 times larger than that of the quadratic fit (-0.0057),

5.3.3 QSM of flow with contrast agent

The above flow scan with flow compensation was repeated a number of times. Each time, the tap water inside the tube was replaced with a gadopentetate dimeglumine (Gd-DTPA, Magnevist, Bayer HealthCare) solution with different concentrations.

Two QSM images were reconstructed, one with a linear and one with an adaptive-quadratic fitted field map. The measured susceptibility was compared with that from the reference QSM images reconstructed from a scan without flow.

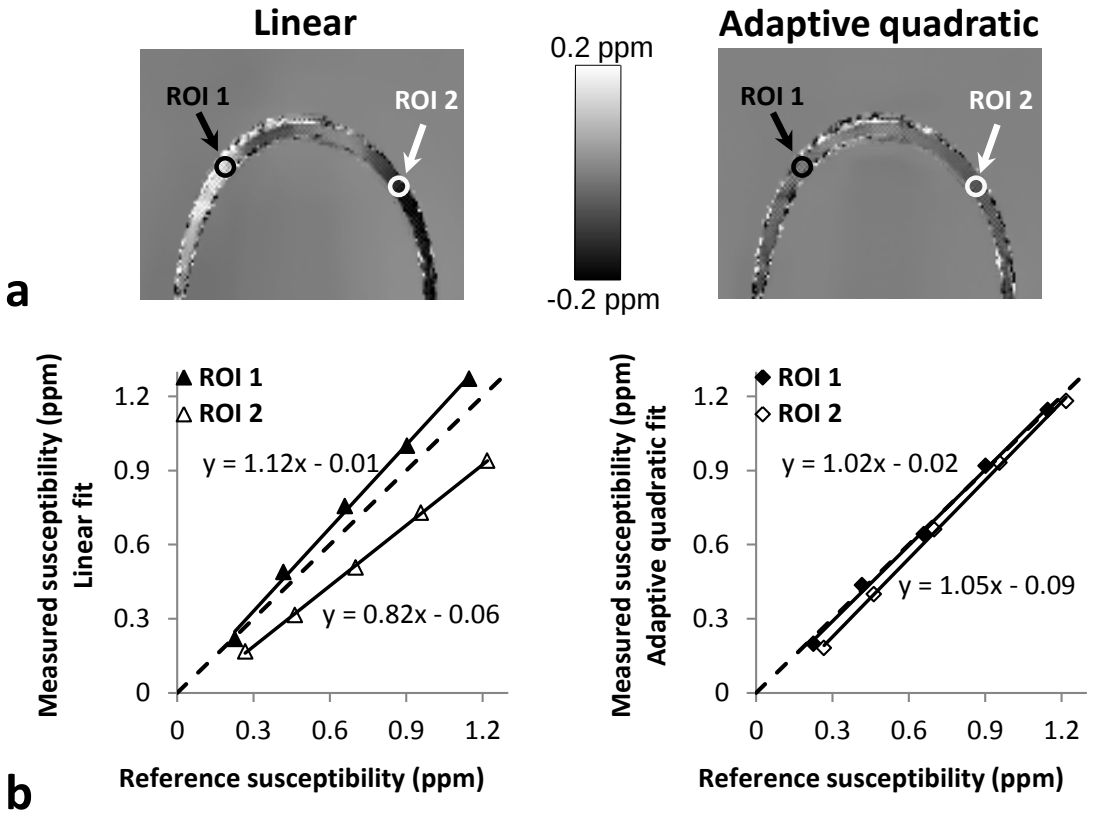

Figure 5.4 QSM of flow with contrast agent
(a) Error map of reconstructed susceptibility of flowing contrast agent solution at a velocity of 60 cm/s. Data was acquired with the fully flow compensated sequence. The reconstruction error using the adaptive-quadratic fit was markedly reduced compared to that using the linear fit, especially in regions pointed to by ROI1 and ROI2. **(b)** Linear regression of the measured susceptibility versus the reference susceptibility. Five experiments with different concentration of contrast agent solutions were performed. The reference susceptibility was obtained in the zero-flow state. The measured susceptibility was obtained using both the linear and the adaptive-quadratic fit at a flow rate of 60 cm/s. Compared with the linear fit, the adaptive-quadratic fit exhibits more accurate measurement over all concentrations with a regression slope close to 1.

Figure 5.4a shows the QSM error image of the flowing contrast agent solution.

The error image was obtained by subtracting the reference QSM acquired during zero flow from the QSM acquired during non-zero flow. Inside the tube, the error of the adaptive-quadratic fit was markedly reduced compared with that from the linear fit, especially in the two ROI regions. Figure 5.4b shows the linear regression of the measured susceptibility versus the reference susceptibility for five distinct contrast agent solutions. In both ROIs, adaptive-quadratic fit exhibits more accurate measurement compared with linear fit over all the concentrations.

5.3.4 Flow velocity measurement

A second flow experiment was performed to validate the polynomial phase expansion in Eq [5.3]. For a given flow velocity, two data sets were acquired for two different Z shimming gradient to create a magnetic field that varies linearly along the B0 direction. The Z direction was chosen because it coincides with the principal direction of the flow in the straight parts of the U shaped tube. A quadratic fit was performed for each of the two acquisitions obtaining $\phi_{\mathrm{shim1}}(\mathbf{r}) = \psi_1(\mathbf{r}) + L_1(\mathbf{r})TE + Q_1(\mathbf{r})TE^2$ and $\phi_{\mathrm{shim2}}(\mathbf{r}) = \psi_2(\mathbf{r}) + L_2(\mathbf{r})TE + Q_2(\mathbf{r})TE^2$. Then, the following holds:

$$\begin{aligned} Q_2(\mathbf{r}) - Q_1(\mathbf{r}) &= -\frac{1}{2}\gamma \mathbf{v}(\mathbf{r}) \cdot \boldsymbol{\nabla}\big(\delta \mathrm{B}_2(\mathbf{r}) - \delta \mathrm{B}_1(\mathbf{r})\big) \\ &= -\frac{1}{2}\mathbf{v_z}(\mathbf{r})\, \partial\big(L_2(\mathbf{r}) - L_1(\mathbf{r})\big)/\, \partial \mathrm{z} \end{aligned} \qquad [5.5]$$

where B_1 and B_2 are the total magnetic field of the two scans. In this equation, we have used the fact that the difference between B_1 and B_2 is induced by the difference in the Z shim, such that the assumption of a spatially linearly varying field

in Eq [5.3] is satisfied. Then, the flow velocity along Z can then be obtained as follows:

$$\mathbf{v_z}(\mathbf{r}) = -2\big(Q_2(\mathbf{r}) - Q_1(\mathbf{r})\big)/\big(\partial\big(L_2(\mathbf{r}) - L_1(\mathbf{r})\big)/\,\partial \mathrm{z}\big) \qquad [5.6]$$

The acquisition of the two data sets with differing Z shimming was repeated for a range of flow velocities between 28cm/s to 62cm/s. For each of the velocities, these two acquisitions were performed (Z shim difference 1400Hz/m) as well as a 2D phase contrast scan (TR/TE = 15/6ms, FA=10˚, FOV=25cm, matrix size = 256×128, slice thickness = 5mm, BW= ±15.63kHz, VENC=100cm/s, using an acquisition plane orthogonal to the straight parts of the U shaped vinyl tube).

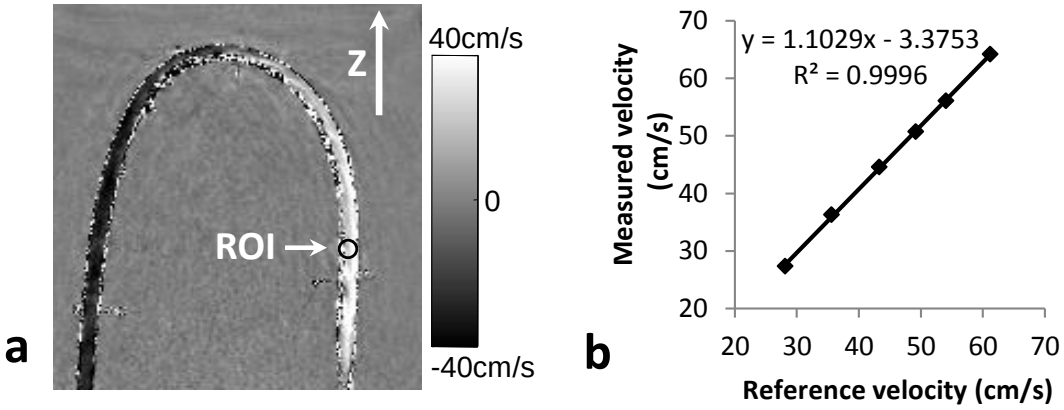

Figure 5.5 Quantification of flow velocity
(a) A representative Z direction flow velocity map computed based on the theory. Two data sets are acquired, which are identical except for a different Z shim gradient. The coefficients of the quadratic fit are used to obtain this velocity map. The estimated flow has opposite signs on the two straight sections, as expected. **(b)** Linear regression of the measured flow velocity versus the reference flow velocity at six velocity settings. The obtained regression slope is 1.1 and R^2 is 0.99, indicating a good agreement of the measured velocity. The reference flow velocity was obtained using a separate phase contrast acquisition for each flow setting.

Figure 5.5a is the Z direction velocity map derived from the second order fit

coefficient of the two scans with varying Z shim gradients. Opposite signs of velocity were observed on the two sides of the U shaped tube as the flow changes signs in the Z direction. The velocity in the selected ROI (see Figure 5.5a) was measured in six experiments with varying flow, which was then compared with the reference velocity measured with a phase contrast scan as shown in Figure 5.5b. Good agreement was found between the two measurements, with a linear regression slope of 1.1 and R^2 of 0.99.

5.4 In Vivo Study

5.4.1 Scan protocol

This study was institutional review board approved and HIPPA-compliant. In N = 8 healthy volunteers (7 male, 1 female), the brain was imaged using an 8-channel head coil on a 3T scanner (GE Healthcare) after obtaining informed consent. Typical scan parameters were: axial scan, 7 echoes, $TR/TE_{first}/TE_{last}$ =48.2/3.7/43.8ms, FA=20˚, FOV =24cm, voxel size = $0.7\times0.7\times0.7mm^3$, BW=±62.5kHz. All volunteers were scanned using the proposed fully flow compensated sequence.

5.4.2 Vein visualization

Both a linear fit and the proposed adaptive-quadratic fit were used to obtain a field map. Two QSM images were reconstructed using the respective field maps. Major veins were identified by an experienced reader in a Maximal Intensity Projections (MIPs) of a 15mm thick volume centered at the location of the boundary between the two hemispheres. The number of visualized cortical veins longer than 1cm was

compared between the two reconstructions.

Figure 5.6 shows QSM MIPs of a 15 mm-thick sagittal slab centered at the location of the boundary between the two hemispheres. Both linear fit and adaptive-quadratic fit results are shown here. The adaptive-quadratic fit reconstruction greatly improves vessel appearance, especially in cortical veins. A number of small veins missing in the linear fit QSM were recovered by the adaptive-quadratic fit method. Some veins that appeared disjointed in the linear fit QSM were better visualized using the adaptive-quadratic fit. The conspicuity and the sharpness of a number of dim veins were improved.

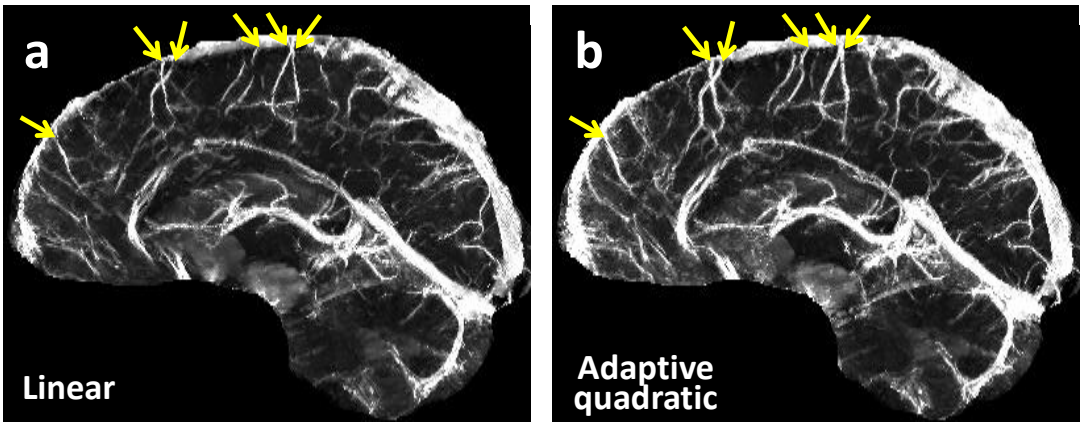

Figure 5.6 MIP of brain susceptibility map
MIPs from linear **(a)** and adaptive-quadratic **(b)** fit QSM shows the improvement of the vessel depiction using the adaptive-quadratic fit. Dim and apparently disconnected veins from the linear fit result are better visualized using the adaptive-quadratic fit.

In all 8 volunteers, more cortical veins were visualized in the adaptive-quadratic fit QSM. Figure 5c shows the number of cortical veins visualized within the 15 mm sagittal MIP in each volunteer. For all cases, more cortical veins were observed and the percentage increase from adaptive-quadratic fit QSM is 37.3%±14.9% ($p<0.001$).

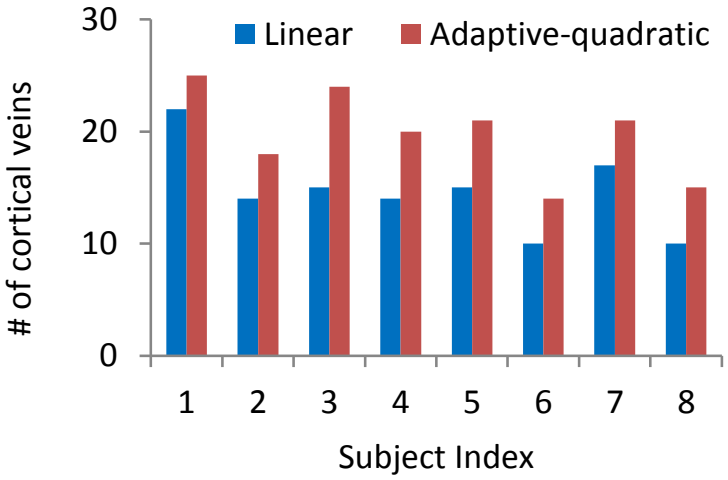

Figure 5.7 Count of cortical veins
Quantitative comparison of visualized cortical veins. In all subject, 37.3%±14.9% more cortical veins are visualized using the adaptive-quadratic fit.

5.4.3 Oxygenation quantification

Venous oxygen saturation SvO_2 was computed using $\chi_{blood} = Hct(1 - SvO_2)\Delta\chi_{do}$ (88). Hematocrit (Hct) was assumed to be 0.4 and the susceptibility difference between fully deoxygenated blood and oxygenated blood $\Delta\chi_{do}$ was assumed to be 3.43ppm (62,86,97). Here χ_{blood} was the measured susceptibility value on the QSM images. In each volunteer, a number of estimates of SvO_2 were obtained by taking the mean over an ROI in each of the six largest cortical veins identified above using both the linear and adaptive-quadratic fit. Next, for each volunteer, the average and standard deviation of these six SvO_2 estimates were computed and compared between the two fitting models. The mean SvO_2 across all selected cortical veins and all volunteers was also computed and compared. All comparisons were analyzed statistically using pair-wise two-tailed t-tests with a p-value of 0.05 indicating statistical significance.

The average venous oxygen saturation of six cortical veins based on the susceptibility map is shown in Figure 5.8. The mean measured SvO_2 value across all volunteers is 72.2%±4.1% for the adaptive-quadratic fit method and 93.1%±5.3% for the linear fit ($p<0.001$). Previous studies measured the SvO_2 in a range of 50% to 75% (98-100). Thus, the mean SvO_2 value from the adaptive-quadratic fit QSM falls within this range while that of the linear fit QSM would appear to lead to overestimation. For each volunteer, the error bar indicated the standard deviation of SvO_2 value over the 6 cortical veins used for measuring. The standard deviations for the linear fit method ranged from 5% to 17%, compared to those of the adaptive-quadratic fit, which ranged from 3% to 6%.

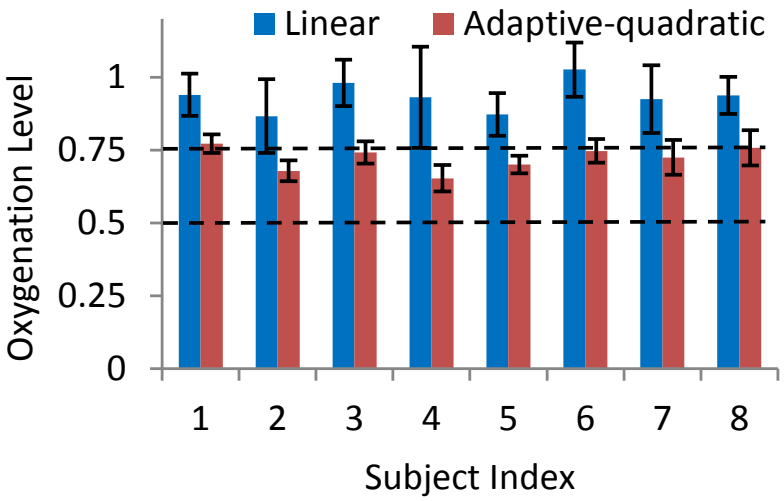

Figure 5.8 Oxygenation level comparison
The measured venous oxygen saturation (SvO_2) from both the linear and adaptive-quadratic fit QSM in all volunteers. Arrows indicate the veins on which the measurements were performed. The value is 72.2%±4.1% for the adaptive-quadratic fit method and 93.1%±5.4% for the linear fit method. The SvO_2 variance over the six cortical veins for ROI analysis for each subject is also smaller for the adaptive-quadratic fit QSM (3%-6%) compared with the linear fit QSM (5%-17%).

5.5 Discussion

The preliminary results in this study suggest that flow compensation by nulling the gradient moment and modeling the flow phase under the gradient of the inhomogeneity field can reduce flow artifacts in image and improve the accuracy of mapping of in-vivo venous blood susceptibility. The flow artifacts in both image magnitude and phase from multi-echo GRE acquisition are markedly reduced by flow compensation. This flow compensated quantitative susceptibility mapping (QSM) method may provide a robust measurement of venous oxygen saturation in the brain, as the blood susceptibility is deoxyhemoglobin concentration times the molar susceptibility of deoxyhemoglobin. Previous approaches to MRI measurements of venous oxygen saturation rely on various assumptions on susceptibility distributions including distribution geometries (65,87,98-105). QSM has the potential to overcome these limitations and errors associated with these assumptions. Flow compensation using imaging gradient moment nulling and inhomogeneity field gradient phase modeling was shown to increase consistency in the estimation of paramagnetic deoxyhemoglobin concentration.

The accumulated phase of proton spin isochromats is determined by the magnetic field they experience. This field may include a spatial gradient term consisting of imaging gradient used for spatial encoding or inhomogeneity field gradient induced by susceptibility sources. The imaging gradient is spatially uniform with magnitude as high as tens of mT/m. The inhomogeneity field gradient may be small and spatially varying, depending on the susceptibility strength and distribution. In the presence of a field gradient, the phase of moving spins is a polynomial function of time, quadratic

for constant flow, as well-known in phase contrast MRA. The nonlinear phase–time relationship can cause erroneous k-space encoding and may lead to vessel displacement in the phase encoding direction and blurring in the readout direction. In a multi-echo acquisition, this flow-induced displacement increases with TE and needs to be compensated for consistent voxel fitting across echoes. Flow compensation can be achieved using gradient moment nulling. In this study, we added bipolar flow compensation gradients in both phase encoding directions before each echo. The maximum TE was kept approximately unchanged. Since the addition of the compensation gradients increased the minimal echo spacing, this meant that the total number of echoes was reduced. To see the effect of the lower number of echoes on the resulting field map, the variance of the fitted field frequency ω can be computed according to (106):

$$\sigma^2(\omega) = \sigma^2 \frac{\sum \rho_i{}^2}{(\sum \rho_i{}^2)(\sum \rho_i{}^2 t_i^2) - (\sum \rho_i{}^2 t_i)^2} \qquad [5.7]$$

where σ is the noise level of the complex echo images and $\rho_i = \rho e^{-\frac{t_i}{T_2^*}}$ is the magnitude for the *i*-th echo. Assuming a constant noise level σ, TE_{min}=4ms, TE_{max}=44ms and T2*=50ms (107) , reducing the number of echoes from 11 to 7 (as used in this study), $\sigma(\omega)$ increases by 20%, leading to a decreased signal to noise for the estimated field frequency ω.

The gradient of the tissue induced inhomogeneity field, although typically much smaller than the imaging gradient, also needs to be considered in multiple echo sequences that include long TEs. This inhomogeneity field gradient may vary in space

with unknown magnitude, making it difficult to be compensated. Consequently, it may cause not only image blurring along the readout direction (dephasing effects on high k_x components) but also quantitative error in phase measurement (phase shift at k_x=0), the quadratic phase–time relationship in Eq [5.3].

The quadratic relationship induced by flow and the inhomogeneity field gradient was demonstrated in the phantom experiment. From Eq [5.3], a linear fit of the phase $\Phi_1$will lead to an underestimation of the field when $\mathbf{v} \cdot \boldsymbol{\nabla}\delta B > 0$ or to an overestimation of the field when $\mathbf{v} \cdot \boldsymbol{\nabla}\delta B < 0$. For the phantom study, the field in ROI 1 decreases along the flow direction, leading to $\mathbf{v} \cdot \boldsymbol{\nabla}\delta B < 0$ consistent with the overestimation of the field and susceptibility in Figure 5.4b (solid triangles). However, in ROI 2, the field increases along the flow direction, leading to $\mathbf{v} \cdot \boldsymbol{\nabla}\delta B > 0$, consistent with the underestimation of the field and susceptibility in Figure 5.4 (hollow triangles). The difference in field estimates between the linear and the adaptive fit can be quite substantial as shown in Figure 5.3b. By fitting the phase data with inclusion of the flow-induced quadratic term, the susceptibility map (Figure 5.4a) was improved. In the in vivo brain study, the condition $\mathbf{v} \cdot \boldsymbol{\nabla}\delta B > 0$ was also observed for the cortical veins where SvO2 was measured, leading to an underestimation of the field and the venous susceptibility. This resulted in oxygen saturation values higher than the range of values reported in the literature (Figure 5.8). The susceptibility map quality improves using the quadratic fit (Figure 5.6), and correspondingly the mean estimated oxygen saturation falls within that range (Figure 5.8). The mean SvO_2 value of 72.2% is consistent with a previous study (105) conducted by Fan et al., using a linear fit of the phase data, provided a value for $\Delta\chi_{do}$

of 0.27 ppm (cgs units, or 3.43 ppm in SI units) is used, as discussed by the authors of that study. This value for $\Delta\chi_{do}$ is consistent with experimentally obtained estimates. Performing QSM with the adaptive-quadratic fit can also eliminate the need to restrict the measurement of SvO2 to those vessels whose phase evolution is sufficiently linear in TE, as done in (105).

In this work, we derived and applied a quadratic fit in the vessel voxels assuming a locally constant flow and a linearly varying field inhomogeneity in one TR interval. A non-constant (pulsatile) flow may exist in the vessels and higher order spatial variations may exist in the inhomogeneity field, resulting in higher order terms to the phase–time relationship. When these terms become substantial, a higher order polynomial fit is needed and can be easily incorporated into the approach outlined here. As the number of fit parameter increases, the noise of the fitted parameter also increases. To maintain a high SNR in the estimated parameters, we may desire the linear fit for voxels known of having no flow. Automated image segmentation of regions of no flow is a difficult mathematical problem. Instead, we adopted an empirical weighted average of both linear and quadratic fits using a weighting determined by the magnitude of the second order coefficient for the quadratic fit (an indication of the flow magnitude) and the difference between the linear coefficients of the two fits (another indication for flow existence). Preliminary results here demonstrated the feasibility of this weighting scheme but it may be further improved.

5.6 Conclusion

By using a fully flow compensated multi-echo GRE sequence and an adaptive-

quadratic fit of the phase images at all echoes, vessel visibility and susceptibility measurements are improved. This method significantly reduces the flow induced displacement artifacts and improves the field inhomogeneity estimation to ensure a more accurate dipole deconvolution for obtaining the susceptibility map. Improved vein susceptibility enables in-vivo measurement of venous oxygen saturation in the brain.

CHAPTER 6

FUTURE DIRECTIONS AND CONCLUSION

6.1 Future Directions

MRI always quest for fast and quantitative imaging technique. Spiral sampling and constrained reconstruction allows dynamic imaging but also brings artifacts. For dynamic MRI, it is desirable to have larger spatial coverage, higher spatial and temporal resolution or to increase temporal resolution. Future research continuing this dissertation involves reducing artifacts, improving motion robustness, and further increasing spatial-temporal resolution. The dynamic imaging technique can also be adjusted to fit in other clinical applications.

6.1.1 Artifacts reduction

Spiral sampling and constrained reconstruction poses artifacts that need further investigation. Specifically the following areas should be looked into.

First is to reduce spiral under-sampling artifacts. TRACER reconstruction employs highly under-sampled spiral to update the temporal information. The under-sampling artifacts are not apparent in a single frame but appear as temporal signal fluctuation across image time series, when imposing strong prior information constraints. One way to eliminate this artifact is to smooth the signal time curves in post-processing. Another way is to impose temporal constraints, such as the second order derivative of time curves in the solving process. In either case, both the temporal changes and the spatial correlation should be taken into account.

Second is to reduce spiral off-resonance artifacts, appearing as blurred image edges. Off-resonance correction requires a field map, which is readily available in a multi-echo acquisition. There are time-segmented and frequency-segmented off-resonance correction scheme in fully sampled dataset. Integrating them with dynamic imaging especially high under-sampled spiral imaging needs further development.

Correction of the spiral sampling trajectory is another area worth looking into. Imperfect gradient field results in k-space sampling trajectory away from prescription, showing as intensity variation across the image. This imperfection is manifested in multi-echo scans when the TR is long. Incorporating trajectory mapping can potentially improve the image quality and quantitation accuracy for dynamic QSM study.

6.1.2 Spatial-temporal resolution improvement

A major improvement would be to further increase the spatial-temporal resolution of TRACER. In the developed cerebral perfusion MRI, the spatial coverage is limited by the temporal resolution of multi-echo acquisition. Further acceleration could be achieved through parallel imaging in slice encoding direction. This could be readily done with segmented slice encoding view order. Each under-sampled slice segment is used to reconstruct a time frame and served as the initial guess for the next segment. The acceleration rate would be the same as the number of segments. Another area worth looking into is true 3D spiral or radial sampling trajectory. These sampling strategies incorporate true 3D k-space coverage in one TR. Consecutive TRs will contain k-space information that is much more incoherent than a stack-of-spiral scan. This allows further temporal resolution improvement as the temporal resolution is not

restricted by a fully sampled slice encoding in stack-of-spiral scan. More uniform k-space coverage may reduce the under-sampling artifacts in TRACER.

Another way to improve the temporal resolution is to incorporate global information in the minimization solver. The TRACER algorithm relies on prior information from previous frames. The acquired data in later frames could also serve as prior information. They can be all combined as one 4D data set for global minimization. This may need initial guess from a sliding window reconstruction and the initial guess could be modified locally to predict the temporal behavior for improved temporal tracking.

6.1.3 Motion correction

Respiratory motion induces liver position changes. In liver perfusion imaging, the motion needs to be corrected for reliable contrast enhancement curve measurement. Due to respiratory motion, a lesion can move out of an ROI, resulting in meaningless measurement. Correction of motion can be integrated into the reconstruction process. A displacement field can be computed along with TRACER by registering consecutive frames. This displacement is formed as an additional term in the minimization problem, forcing the liver to stay still. The structures of an artifact free liver image at the beginning of the scan can also be used to constrain motion corrupted data. The other direction of motion correction is to post-process enhancement curves from motion corrupted TRACER reconstruction. The selected ROI is allowed to move in a 3D neighborhood to track the tissue. Then the temporal curves is also constrained to be smooth and with limited amount temporal basis functions to reduce the search space.

6.1.4 Exploration of application

Multi-echo spiral acquisitions can be used in liver QSM. Liver imaging with breath hold requires acquisition time less than 30 seconds in clinical studies. Spiral sampling provides the opportunity to complete a QSM scan in one breath hold. This enables absolute quantification of iron deposition in liver which is a biomarker in liver examination. The oxygenation in portal vein, hepatic artery and hepatic veins can also be quantified to study liver function. Due to the existence of lungs, stomach and fat, good segmentation of liver and field estimation without fat effect would be desired in liver QSM.

Another application is to use dual-echo spiral acquisition with TRACER reconstruction dynamic for liver MRA. The current DCE liver perfusion requires fat suppression. Fat suppression is often affected due to deviation of fat off-resonance frequency from programed value, imperfect rf pulse or field inhomogeneity. Dual-echo acquisition with a TE different close to 2ms can produce two datasets with a π phase different for water-fat separation using two-point Dixon method. The water image from this reconstruction will have an improved CNR of vessels compared with traditional fat-suppression method.

6.2 Conclusion

In this dissertation, three imaging techniques were developed to quantify tissue perfusion and oxygenation. The liver perfusion technique achieves sub-second temporal resolution with high spatial resolution and coverage. It has been routinely used in our hospital as a clinical protocol. The dynamic QSM method allows direction

contrast agent quantification. It avoids assumptions in R_2* based method, promises to produce improved contrast agent quantification. The proposed flow compensation and quadratic fitting resolves flow issues in QSM and provides a method for in vivo blood oxygenation quantification.

BIBLIOGRAPHY

1. Prince MR, Yucel EK, Kaufman JA, Harrison DC, Geller SC. Dynamic gadolinium-enhanced three-dimensional abdominal MR arteriography. J Magn Reson Imaging 1993;3(6):877-881.

2. Rofsky NM, Lee VS, Laub G, Pollack MA, Krinsky GA, Thomasson D, Ambrosino MM, Weinreb JC. Abdominal MR imaging with a volumetric interpolated breath-hold examination. Radiology 1999;212(3):876-884.

3. Lee VS, Lavelle MT, Rofsky NM, Laub G, Thomasson DM, Krinsky GA, Weinreb JC. Hepatic MR imaging with a dynamic contrast-enhanced isotropic volumetric interpolated breath-hold examination: feasibility, reproducibility, and technical quality. Radiology 2000;215(2):365-372.

4. Hagiwara M, Rusinek H, Lee VS, Losada M, Bannan MA, Krinsky GA, Taouli B. Advanced liver fibrosis: diagnosis with 3D whole-liver perfusion MR imaging--initial experience. Radiology 2008;246(3):926-934.

5. Baxter S, Wang ZJ, Joe BN, Qayyum A, Taouli B, Yeh BM. Timing bolus dynamic contrast-enhanced (DCE) MRI assessment of hepatic perfusion: Initial experience. J Magn Reson Imaging 2009;29(6):1317-1322.

6. Wang J, Chen LT, Tsang YM, Liu TW, Shih TT. Dynamic contrast-enhanced MRI analysis of perfusion changes in advanced hepatocellular carcinoma treated with an antiangiogenic agent: a preliminary study. AJR Am J Roentgenol 2004;183(3):713-719.

7. Materne R, Smith AM, Peeters F, Dehoux JP, Keyeux A, Horsmans Y, Van Beers BE. Assessment of hepatic perfusion parameters with dynamic MRI. Magn Reson Med 2002;47(1):135-142.

8. Wilman AH, Riederer SJ, King BF, Debbins JP, Rossman PJ, Ehman RL. Fluoroscopically triggered contrast-enhanced three-dimensional MR angiography with elliptical centric view order: application to the renal arteries. Radiology 1997;205(1):137-146.

9. Goncalves Neto JA, Altun E, Vaidean G, Elazzazi M, Troy J, Ramachandran S, Semelka RC. Early contrast enhancement of the liver: exact description of subphases using MRI. Magn Reson Imaging 2009;27(6):792-800.

10. Uecker M, Zhang S, Voit D, Karaus A, Merboldt KD, Frahm J. Real-time MRI at a resolution of 20 ms. NMR Biomed 2010;23(8):986-994.

11. Uecker M, Hohage T, Block KT, Frahm J. Image reconstruction by regularized nonlinear inversion--joint estimation of coil sensitivities and image content.

Magn Reson Med 2008;60(3):674-682.

12. Uecker M, Zhang S, Frahm J. Nonlinear inverse reconstruction for real-time MRI of the human heart using undersampled radial FLASH. Magn Reson Med 2010;63(6):1456-1462.

13. Kaltenbacher B, Neubauer A, Scherzer O. Iterative Regularization Methods for Nonlinear Ill-Posed Problems: Walter de Gruyter; 2008.

14. Scherzer O. Iterative Solution Methods. Handbook of Mathematical Methods in Imaging. 1st ed: Springer; 2011.

15. Marquardt DW. An Algorithm for Least-Squares Estimation of Nonlinear Parameters. J Soc Ind Appl Math 1963;11(2):431-441.

16. Kressler B, Spincemaille P, Nguyen TD, Cheng L, Xi Hai Z, Prince MR, Wang Y. Three-dimensional cine imaging using variable-density spiral trajectories and SSFP with application to coronary artery angiography. Magn Reson Med 2007;58(3):535-543.

17. Semelka RC, Shoenut JP, Kroeker MA, Greenberg HM, Simm FC, Minuk GY, Kroeker RM, Micflikier AB. Focal liver disease: comparison of dynamic contrast-enhanced CT and T2-weighted fat-suppressed, FLASH, and dynamic gadolinium-enhanced MR imaging at 1.5 T. Radiology 1992;184(3):687-694.

18. Meyer CH, Hu BS, Nishimura DG, Macovski A. Fast spiral coronary artery imaging. Magn Reson Med 1992;28(2):202-213.

19. Spielman DM, Pauly JM, Meyer CH. Magnetic resonance fluoroscopy using spirals with variable sampling densities. Magn Reson Med 1995;34(3):388-394.

20. Kim YC, Narayanan SS, Nayak KS. Flexible retrospective selection of temporal resolution in real-time speech MRI using a golden-ratio spiral view order. Magn Reson Med 2011;65(5):1365-1371.

21. Winkelmann S, Schaeffter T, Koehler T, Eggers H, Doessel O. An optimal radial profile order based on the Golden Ratio for time-resolved MRI. IEEE Trans Med Imaging 2007;26(1):68-76.

22. Wajer F, Pruessmann K. Major speedup of reconstruction for sensitivity encoding with arbitrary trajectories. Proceedings of the ISMRM 9th Annual Meeting. Glasgow, Scotland; 2001. p 767.

23. Beatty PJ, Nishimura DG, Pauly JM. Rapid gridding reconstruction with a minimal oversampling ratio. IEEE Trans Med Imaging 2005;24(6):799-808.

24. Haider CR, Hu HH, Campeau NG, Huston J, 3rd, Riederer SJ. 3D high temporal

and spatial resolution contrast-enhanced MR angiography of the whole brain. Magn Reson Med 2008;60(3):749-760.

25. Bae KT, Heiken JP, Brink JA. Aortic and hepatic contrast medium enhancement at CT. Part I. Prediction with a computer model. Radiology 1998;207(3):647-655.

26. Riederer SJ, Tasciyan T, Farzaneh F, Lee JN, Wright RC, Herfkens RJ. MR fluoroscopy: technical feasibility. Magn Reson Med 1988;8(1):1-15.

27. Barger AV, Block WF, Toropov Y, Grist TM, Mistretta CA. Time-resolved contrast-enhanced imaging with isotropic resolution and broad coverage using an undersampled 3D projection trajectory. Magn Reson Med 2002;48(2):297-305.

28. Song HK, Dougherty L. Dynamic MRI with projection reconstruction and KWIC processing for simultaneous high spatial and temporal resolution. Magn Reson Med 2004;52(4):815-824.

29. Fienup JR, Kowalczyk AM. Phase Retrieval for a Complex-Valued Object by Using a Low-Resolution Image. J Opt Soc Am A 1990;7(3):450-458.

30. Applegate GR, Thaete FL, Meyers SP, Davis PL, Talagala SL, Recht M, Wozney P, Kanal E. Blood-Flow in the Portal-Vein - Velocity Quantitation with Phase-Contrast Mr Angiography. Radiology 1993;187(1):253-256.

31. Pedersen H, Kozerke S, Ringgaard S, Nehrke K, Kim WY. k-t PCA: temporally constrained k-t BLAST reconstruction using principal component analysis. Magn Reson Med 2009;62(3):706-716.

32. Vitanis V, Manka R, Giese D, Pedersen H, Plein S, Boesiger P, Kozerke S. High resolution three-dimensional cardiac perfusion imaging using compartment-based k-t principal component analysis. Magn Reson Med 2011;65(2):575-587.

33. Brinegar C, Schmitter SS, Mistry NN, Johnson GA, Liang ZP. Improving Temporal Resolution of Pulmonary Perfusion Imaging in Rats Using the Partially Separable Functions Model. Magnet Reson Med 2010;64(4):1162-1170.

34. Chen GH, Tang J, Leng S. Prior image constrained compressed sensing (PICCS): a method to accurately reconstruct dynamic CT images from highly undersampled projection data sets. Med Phys 2008;35(2):660-663.

35. Trzasko JD, Haider CR, Borisch EA, Campeau NG, Glockner JF, Riederer SJ, Manduca A. Sparse-CAPR: highly accelerated 4D CE-MRA with parallel imaging and nonconvex compressive sensing. Magn Reson Med 2011;66(4):1019-1032.

36. Samsonov A, Jung Y, Alexander A, Block W, Field A. MRI Compressed Sensing via Sparsifying Images. Proceedings of the ISMRM 16th Annual Meeting. Toronto; 2008. p 342.

37. Velikina J, Johnson K, Block KT, Samsonov A. Design of Temporally Constrained Compressed Sensing Methods for Accelerated Dynamic MRI. Proceedings of the ISMRM 18th Annual Meeting. Stockholm; 2010.

38. Wang H, Miao Y, Zhou K, Yu Y, Bao S, He Q, Dai Y, Xuan SY, Tarabishy B, Ye Y, Hu J. Feasibility of high temporal resolution breast DCE-MRI using compressed sensing theory. Med Phys 2010;37(9):4971-4981.

39. Seiberlich N, Jeong HJ, Carroll TJ, Griswold M. Parameter-Free Reconstruction of Highly Undersampled MR Angiography Images using Gradient Descent with Sparsification. Proceedings of the ISMRM 18th Annual Meeting. Stockholm; 2010. p 4873.

40. Adluru G, Tasdizen T, Schabel MC, DiBella EV. Reconstruction of 3D dynamic contrast-enhanced magnetic resonance imaging using nonlocal means. J Magn Reson Imaging 2010;32(5):1217-1227.

41. Sumbul U, Santos JM, Pauly JM. Improved time series reconstruction for dynamic magnetic resonance imaging. IEEE Trans Med Imaging 2009;28(7):1093-1104.

42. Eggers H, Boernert P, Boesiger P. Comparison of gridding- and convolution-based iterative reconstruction algorithms for sensitivity-encoded non-Cartesian acquisitions. 2002; Honolulu. p 130.

43. Stone SS, Haldar JP, Tsao SC, Hwu WM, Sutton BP, Liang ZP. Accelerating Advanced MRI Reconstructions on GPUs. J Parallel Distrib Comput 2008;68(10):1307-1318.

44. Edelman RR, Mattle HP, Atkinson DJ, Hill T, Finn JP, Mayman C, Ronthal M, Hoogewoud HM, Kleefield J. Cerebral blood flow: assessment with dynamic contrast-enhanced T2*-weighted MR imaging at 1.5 T. Radiology 1990;176(1):211-220.

45. Rosen BR, Belliveau JW, Vevea JM, Brady TJ. Perfusion imaging with NMR contrast agents. Magn Reson Med 1990;14(2):249-265.

46. Rempp KA, Brix G, Wenz F, Becker CR, Guckel F, Lorenz WJ. Quantification of regional cerebral blood flow and volume with dynamic susceptibility contrast-enhanced MR imaging. Radiology 1994;193(3):637-641.

47. Willats L, Calamante F. The 39 steps: evading error and deciphering the secrets for accurate dynamic susceptibility contrast MRI. NMR Biomed

2013;26(8):913-931.

48. van Osch MJ, Vonken EJ, Viergever MA, van der Grond J, Bakker CJ. Measuring the arterial input function with gradient echo sequences. Magn Reson Med 2003;49(6):1067-1076.

49. Calamante F, Vonken EJPA, van Osch MJP. Contrast agent concentration measurements affecting quantification of bolus-tracking perfusion MRI. Magnet Reson Med 2007;58(3):544-553.

50. Calamante F, Connelly A, van Osch MJ. Nonlinear DeltaR*2 effects in perfusion quantification using bolus-tracking MRI. Magn Reson Med 2009;61(2):486-492.

51. Pedersen M, Klarhofer M, Christensen S, Ouallet JC, Ostergaard L, Dousset V, Moonen C. Quantitative cerebral perfusion using the PRESTO acquisition scheme. J Magn Reson Imaging 2004;20(6):930-940.

52. Kjolby BF, Ostergaard L, Kiselev VG. Theoretical model of intravascular paramagnetic tracers effect on tissue relaxation. Magn Reson Med 2006;56(1):187-197.

53. Quarles CC, Ward BD, Schmainda KM. Improving the reliability of obtaining tumor hemodynamic parameters in the presence of contrast agent extravasation. Magn Reson Med 2005;53(6):1307-1316.

54. Boxerman JL, Schmainda KM, Weisskoff RM. Relative cerebral blood volume maps corrected for contrast agent extravasation significantly correlate with glioma tumor grade, whereas uncorrected maps do not. AJNR Am J Neuroradiol 2006;27(4):859-867.

55. Conturo TE, Barker PB, Mathews VP, Monsein LH, Bryan RN. Mr Imaging of Cerebral Perfusion by Phase-Angle Reconstruction of Bolus Paramagnetic-Induced Frequency-Shifts. Magnet Reson Med 1992;27(2):375-390.

56. Akbudak E, Conturo TE. Arterial input functions from MR phase imaging. Magnet Reson Med 1996;36(6):809-815.

57. Kotys MS, Akbudak E, Markham J, Conturo TE. Precision, signal-to-noise ratio, and dose optimization of magnitude and phase arterial input functions in dynamic susceptibility contrast MRI. J Magn Reson Imaging 2007;25(3):598-611.

58. de Rochefort L, Nguyen T, Brown R, Spincemaille P, Choi G, Weinsaft J, Prince MR, Wang Y. In vivo quantification of contrast agent concentration using the induced magnetic field for time-resolved arterial input function measurement with MRI. Med Phys 2008;35(12):5328-5339.

59. Liu T, Wisnieff C, Lou M, Chen W, Spincemaille P, Wang Y. Nonlinear formulation of the magnetic field to source relationship for robust quantitative susceptibility mapping. Magn Reson Med 2012.

60. Bonekamp D, Li X, Leigh R, Van Zijl PC, Barker PB. Optimized Processing of Quantitative Susceptibility Mapping-Based Gadolinium Perfusion MRI: Correction of Bulk Susceptibility Effects and Comparison of Arterial Input Function Selection from DeltaR2* and QSM Data. Proceedings of the ISMRM 21st Annual Meeting. Salt Lake City; 2013.

61. Xu B, Spincemaille P, Chen G, Agrawal M, Nguyen TD, Prince MR, Wang Y. Fast 3D contrast enhanced MRI of the liver using temporal resolution acceleration with constrained evolution reconstruction. Magn Reson Med 2012.

62. Wang Y. Principles of Magnetic Resonance Imaging: Physics Concepts, Pulse Sequences, & Biomedical Applications: CreateSpace Independent Publishing Platform; 2012. 276 p.

63. Ostergaard L, Weisskoff RM, Chesler DA, Gyldensted C, Rosen BR. High resolution measurement of cerebral blood flow using intravascular tracer bolus passages. Part I: Mathematical approach and statistical analysis. Magn Reson Med 1996;36(5):715-725.

64. Jenkinson M, Beckmann CF, Behrens TE, Woolrich MW, Smith SM. Fsl. Neuroimage 2012;62(2):782-790.

65. Haacke EM, Tang J, Neelavalli J, Cheng YC. Susceptibility mapping as a means to visualize veins and quantify oxygen saturation. J Magn Reson Imaging 2010;32(3):663-676.

66. Schweser F, Deistung A, Lehr BW, Reichenbach JR. Quantitative imaging of intrinsic magnetic tissue properties using MRI signal phase: an approach to in vivo brain iron metabolism? Neuroimage 2011;54(4):2789-2807.

67. Liu T, Surapaneni K, Lou M, Cheng L, Spincemaille P, Wang Y. Cerebral microbleeds: burden assessment by using quantitative susceptibility mapping. Radiology 2012;262(1):269-278.

68. Schweser F, Sommer K, Deistung A, Reichenbach JR. Quantitative susceptibility mapping for investigating subtle susceptibility variations in the human brain. Neuroimage 2012;62(3):2083-2100.

69. Xu B, Liu T, Spincemaille P, Prince M, Wang Y. Flow compensated quantitative susceptibility mapping for venous oxygenation imaging. Magn Reson Med 2013.

70. Liu T, Eskreis-Winkler S, Schweitzer AD, Chen W, Kaplitt MG, Tsiouris AJ,

Wang Y. Improved Subthalamic Nucleus Depiction with Quantitative Susceptibility Mapping. Radiology 2013.

71. Schweser F, Deistung A, Sommer K, Reichenbach JR. Toward online reconstruction of quantitative susceptibility maps: Superfast dipole inversion. Magn Reson Med 2012.

72. Plein S, Ryf S, Schwitter J, Radjenovic A, Boesiger P, Kozerke S. Dynamic contrast-enhanced myocardial perfusion MRI accelerated with k-t sense. Magn Reson Med 2007;58(4):777-785.

73. Otazo R, Kim D, Axel L, Sodickson DK. Combination of compressed sensing and parallel imaging for highly accelerated first-pass cardiac perfusion MRI. Magn Reson Med 2010;64(3):767-776.

74. Velikina JV, Jung Y, Field A, Samsonov A. High Resolution Dynamic Susceptibility Contrast Perfusion Imaging Using Multi-Echo Spirals and Temporal Compressed Sensing-Based Reconstruction. Proceedings of the ISMRM 21st Annual Meeting. Salt Lake City; 2013.

75. Wu B, Li W, Avram AV, Gho SM, Liu C. Fast and tissue-optimized mapping of magnetic susceptibility and T2* with multi-echo and multi-shot spirals. Neuroimage 2012;59(1):297-305.

76. Weisskoff RM, Zuo CS, Boxerman JL, Rosen BR. Microscopic Susceptibility Variation and Transverse Relaxation - Theory and Experiment. Magnet Reson Med 1994;31(6):601-610.

77. Liu J, Liu T, de Rochefort L, Ledoux J, Khalidov I, Chen W, Tsiouris AJ, Wisnieff C, Spincemaille P, Prince MR, Wang Y. Morphology enabled dipole inversion for quantitative susceptibility mapping using structural consistency between the magnitude image and the susceptibility map. Neuroimage 2012;59(3):2560-2568.

78. de Rochefort L, Liu T, Kressler B, Liu J, Spincemaille P, Lebon V, Wu J, Wang Y. Quantitative susceptibility map reconstruction from MR phase data using bayesian regularization: validation and application to brain imaging. Magn Reson Med 2010;63(1):194-206.

79. Liu T, Spincemaille P, de Rochefort L, Kressler B, Wang Y. Calculation of susceptibility through multiple orientation sampling (COSMOS): a method for conditioning the inverse problem from measured magnetic field map to susceptibility source image in MRI. Magn Reson Med 2009;61(1):196-204.

80. Shmueli K, de Zwart JA, van Gelderen P, Li TQ, Dodd SJ, Duyn JH. Magnetic susceptibility mapping of brain tissue in vivo using MRI phase data. Magn Reson Med 2009;62(6):1510-1522.

81. Li W, Wu B, Liu C. Quantitative susceptibility mapping of human brain reflects spatial variation in tissue composition. Neuroimage 2011;55(4):1645-1656.

82. Wharton S, Bowtell R. Whole-brain susceptibility mapping at high field: a comparison of multiple- and single-orientation methods. Neuroimage 2010;53(2):515-525.

83. Liu T, Wisnieff C, Lou M, Chen W, Spincemaille P, Wang Y. Nonlinear formulation of the magnetic field to source relationship for robust quantitative susceptibility mapping. Magn Reson Med 2013;69(2):467-476.

84. Langkammer C, Schweser F, Krebs N, Deistung A, Goessler W, Scheurer E, Sommer K, Reishofer G, Yen K, Fazekas F, Ropele S, Reichenbach JR. Quantitative susceptibility mapping (QSM) as a means to measure brain iron? A post mortem validation study. Neuroimage 2012;62(3):1593-1599.

85. Schafer A, Forstmann BU, Neumann J, Wharton S, Mietke A, Bowtell R, Turner R. Direct visualization of the subthalamic nucleus and its iron distribution using high-resolution susceptibility mapping. Hum Brain Mapp 2012;33(12):2831-2842.

86. Jain V, Abdulmalik O, Propert KJ, Wehrli FW. Investigating the magnetic susceptibility properties of fresh human blood for noninvasive oxygen saturation quantification. Magn Reson Med 2012;68(3):863-867.

87. Fernandez-Seara MA, Techawiboonwong A, Detre JA, Wehrli FW. MR susceptometry for measuring global brain oxygen extraction. Magnet Reson Med 2006;55(5):967-973.

88. Weisskoff RM, Kiihne S. Mri Susceptometry - Image-Based Measurement of Absolute Susceptibility of Mr Contrast Agents and Human Blood. Magnet Reson Med 1992;24(2):375-383.

89. Yamada K, Naruse S, Nakajima K, Furuya S, Morishita H, Kizu O, Maeda T, Takeo K, Shimizu K. Flow velocity of the cortical vein and its effect on functional brain MRI at 1.5T: preliminary results by cine-MR venography. J Magn Reson Imaging 1997;7(2):347-352.

90. Becker G, Perez J, Krone A, Demuth K, Lindner A, Hofmann E, Winkler J, Bogdahn U. Transcranial color-coded real-time sonography in the evaluation of intracranial neoplasms and arteriovenous malformations. Neurosurgery 1992;31(3):420-428.

91. Bernstein MA, King KF, Zhou ZJ. Handbook of MRI pulse sequences. Amsterdam ; Boston: Academic Press; 2004. xxii,1017 p. p.

92. Bernstein MA, Shimakawa A, Pelc NJ. Minimizing TE in moment-nulled or

flow-encoded two- and three-dimensional gradient-echo imaging. J Magn Reson Imaging 1992;2(5):583-588.

93. Slavin GS, Riederer SJ. Gradient moment smoothing: a new flow compensation technique for multi-shot echo-planar imaging. Magn Reson Med 1997;38(3):368-377.

94. Nishimura DG, Jackson JI, Pauly JM. On the nature and reduction of the displacement artifact in flow images. Magn Reson Med 1991;22(2):481-492.

95. Haacke EM, Lenz GW. Improving MR image quality in the presence of motion by using rephasing gradients. AJR Am J Roentgenol 1987;148(6):1251-1258.

96. Butts K, Riederer SJ. Analysis of flow effects in echo-planar imaging. J Magn Reson Imaging 1992;2(3):285-293.

97. Spees WM, Yablonskiy DA, Oswood MC, Ackerman JJH. Water proton MR properties of human blood at 1.5 Tesla: Magnetic susceptibility, T-1, T-2, T-2* and non-Lorentzian signal behavior. Magnet Reson Med 2001;45(4):533-542.

98. Wright GA, Hu BS, Macovski A. 1991 I.I. Rabi Award. Estimating oxygen saturation of blood in vivo with MR imaging at 1.5 T. J Magn Reson Imaging 1991;1(3):275-283.

99. Haacke EM, Lai S, Reichenbach JR, Kuppusamy K, Hoogenraad FGC, Takeichi H, Lin WL. In vivo measurement of blood oxygen saturation using magnetic resonance imaging: A direct validation of the blood oxygen level-dependent concept in functional brain imaging. Human Brain Mapping 1997;5(5):341-346.

100. Lu H, Ge Y. Quantitative evaluation of oxygenation in venous vessels using T2-Relaxation-Under-Spin-Tagging MRI. Magn Reson Med 2008;60(2):357-363.

101. Golay X, Silvennoinen MJ, Zhou JY, Clingman CS, Kauppinen RA, Pekar JJ, van Zijl PCM. Measurement of tissue oxygen extraction ratios from venous blood T-2: Increased precision and validation of principle. Magnet Reson Med 2001;46(2):282-291.

102. Oja JM, Gillen JS, Kauppinen RA, Kraut M, van Zijl PC. Determination of oxygen extraction ratios by magnetic resonance imaging. J Cereb Blood Flow Metab 1999;19(12):1289-1295.

103. Bolar DS, Rosen BR, Sorensen AG, Adalsteinsson E. QUantitative Imaging of eXtraction of oxygen and TIssue consumption (QUIXOTIC) using venular-targeted velocity-selective spin labeling. Magn Reson Med 2011;66(6):1550-1562.

104. Jain V, Langham MC, Wehrli FW. MRI estimation of global brain oxygen

consumption rate. J Cereb Blood Flow Metab 2010;30(9):1598-1607.

105. Fan AP, Benner T, Bolar DS, Rosen BR, Adalsteinsson E. Phase-based regional oxygen metabolism (PROM) using MRI. Magn Reson Med 2012;67(3):669-678.

106. Kressler B, de Rochefort L, Liu T, Spincemaille P, Jiang Q, Wang Y. Nonlinear regularization for per voxel estimation of magnetic susceptibility distributions from MRI field maps. IEEE Trans Med Imaging 2010;29(2):273-281.

107. Siemonsen S, Finsterbusch J, Matschke J, Lorenzen A, Ding XQ, Fiehler J. Age-dependent normal values of T2* and T2' in brain parenchyma. AJNR Am J Neuroradiol 2008;29(5):950-955.